IEKP-KA/2013-01

Physikalische Analyse des Ansprechverhaltens des CMS Siliziumdetektors beim Betrieb am LHC

Zur Erlangungung des akademischen Grades eines
DOKTORS DER NATURWISSENSCHAFTEN
von der Fakulät für Physik des
Karlsruher Instituts für Technologie (KIT) genehmigte

DISSERTATION

von

Dipl. Phys. Christian Barth
aus Saarbrücken

Tag der mündlichen Prüfung: 11.01.2013
Referent: Prof. Dr. Thomas Müller, Institut für Experimentelle Kernphysik
Korreferent: Prof. Dr. Wim de Boer, Institut für Experimentelle Kernphysik

Deutsche Zusammenfassung

Die Frage nach dem Aufbau der Materie und den fundamentalen Wechselwirkungen fasziniert und inspiriert die Menschheit bereits seit Urzeiten. Jedoch waren es die technischen Fortschritte des letzten Jahrhunderts die eine völlig neue Ära auf diesem Gebiet eingeläutet haben. Mit der Entwicklung der Teilchenbeschleuniger konnten erstmals Kollisionen von hochenergetischen Elementarteilchen gezielt herbeigeführt werden. Die ersten Apparaturen, wie der Cockcroft-Walton Generator, konnten Ionen bis in den MeV Bereich beschleunigen. Dank des technischen Fortschritts kann der größte Beschleuniger-Komplex, der LHC am CERN, heute Protonen mit einer Schwerpunktenergie von 8 TeV kollidieren lassen. Nach Wartungsarbeiten in 2013 und 2014 ist sogar 14 TeV vorgesehen. Mit Hilfe steigender Energien ist es möglich bisher unerreichbare Bereiche der Physik zu erforschen.

Doch eine hohe Kollisions-Energie ist nur eine wichtige Vorraussetzung um neuartige Physik zu entdecken. Von besonderer Bedeutung ist zudem die Erzeugung von hohen Ereignisraten. Auf diese Weise können mit Hilfe ausgefeilter statistischer Methoden selbst extrem seltene Prozesse untersucht werden die bisher unentdeckt blieben.

Das prominenteste Beispiel ist das Higgs-Boson. Dieses Elementarteilchen wurde in den 1960er Jahren vorhergesagt, als eine Konsequenz auf den theoretischen Mechanismus der für die Masse der Elementarteilchen verantwortlich ist. Lange wurde vergeblich nach diesem Baustein der Theorie gesucht, bis im diesjährigen 2012 die beiden großen Experimente CMS und ATLAS am LHC ein neues Boson entdeckt haben, dass mit sehr großer Wahrscheinlichkeit das Higgs-Boson ist. Der technische Aufwand der LHC Experimente ist kaum in Worte zu fassen. Abertausende Physiker, Ingenieure, Informatiker und andere Wissenschaftler arbeiten am geligen des größten jemals von Menschen erbauten physikalischen Versuches.

Neben dem Teilchenbeschleuniger-Komplex sind die Detektoren der wichtigste Bestandteil der Experimente. Für CMS ist es der namensgebende *Compact Muon Solenoid*. Er ist der schwerste von Menschen gebaute Detektor und gehört zusammen mit ATLAS zu den beiden großen Universaldetektoren am LHC, die aus einer Vielzahl von verschiedenen aufeinander abgestimmten Systemen bestehen. Das Kernstück von CMS ist der Silizium-Tracker. Er bildet mit über 200 m^2 den größten Halbleiterdetektor der Welt. Mit seiner Hilfe können die Trajektorien der Kollisions-Produkte die im inneren des starken Magnetfeldes sich auf gebogenen Bahnen bewegen vermessen werden.

Zentrales Thema dieser Arbeit ist die Untersuchung der Veränderung der Eigenschaften des Silizium-Streifen-Detektors am CMS in Hinblick auf die Schädigung durch die extreme Strahlungsbelastung. Die Dissertation beginnt mit einem Überblick über das Standardmodell der Elementarteilchenphysik, dass eine schlüssige Theorie der Teilchen und fundementalen Wechselwirkungen bildet. Die Fermionen und Eichbosonen sind in Tabelle 1 und 2 aufgelistet. In diesem Zusammenhang wird auch der Higgs-Mechanismus diskutiert, und die experimentelle Suche nach dem Higgs-Boson angesprochen.

	I Generation	II Generation	III Generation
Quarks	Up (u) Down (d)	Charm (c) Strange (s)	Top (t) Bottom (b)
Leptonen	Elektron (e^-) Elektron-Neutrino (ν_e)	Myon (μ^-) Myon-Neutrino (ν_μ)	Tauon (τ^-) Tauon-Neutrino (ν_τ)

Table 1: Fermionen im Standardmodel.

Wechselwirkung:	Starke W.	Schwache W.	Elektromagnetische W.
Boson:	g	Z^0, W^{+-}	γ

Table 2: Eichbosonen im Standardmodel.

Dem folgt ein Kapitel über die Wirkungsweise von Silizium-Sensoren, wobei ein besonderes Augenmerk auf die strahlungsbedingte Veränderung des Leckstroms und der Verarmungsspannung gelegt wird. Die Erhöhung des Leckstroms hängt linear von dem bestrahlten Volumen und der Fluenz ab, wobei durch die Zeit- und Temperaturabhängigkeit des Faktors $\alpha(t, T)$ das Ausheilen der Strahlenschädigung beschrieben wird.

$$\Delta I = \alpha(t, T)\Phi_{eq}V \tag{1}$$

Die Veränderung der Verarmungsspannung ist mit einer Zu- beziehungsweise Abnahme der effektiven freien Ladungsträgerkonzentration identisch. Die Abhängigkeiten von Strahlung, Ausheilungsdauer und Temperatur werden durch das Hamburg Modell beschrieben. Es teilt die Veränderung in drei Terme auf: der erste beschreibt die Schädigung die zeitlich unverändert bleibt. Ein weiterer Term beschreibt das positive temperaturabhängige Ausheilen, dass sich auf kleinen Zeitskalen abspielt. Der dritte Term trägt der Tatsache Rechnung, dass auf langen Zeitskalen auch ein negatives, inverses Ausheilen erfolgt.

$$\Delta N_{eff}(\Phi_{eq}, t, T) = N_{C,0}(\Phi_{eq}) + N_A(\Phi_{eq}, t, T) + N_Y(\Phi_{eq}, t, T). \tag{2}$$

Nach einer Einführung in den Beschleuniger-Komplex LHC und das CMS Experiment, wird die strahlenbedingte Veränderung des CMS Silizium-Streifendetektors behandelt. In diesem Zusammenhang werden sogenannte Fluka-Simulationen vorgestellt. Diese MonteCarlo-Simulationen liefern, zusammen mit einem Modell des in CMS verwendeten Materials, zu einer Abschätzung der Fluenz an einem beliebigen Punkt im inneren des Trackers. Daraufhin werden die etablierten Messmethoden zur Bestimmung des Leckstrom behandelt. Dabei werden auch die thermischen Bedingungen der Sensoren, und das temperaturabhängige Skalieren des Leckstroms diskutiert. Mit Hilfe von Leckstrom-Messungen - auf Temperatur und Volumen normiert - wurde die Fluenz-Simulationen bestätigt.

Desweiteren werden zwei Messverfahren beschrieben, die für eine Bestimmung der Verarmungsspannung im laufenden Betrieb entwickelt wurden: Die erste Methode nutzt die Abhängigkeit des Sensor-Rauschens von der angelegten Betriebsspannung. Basierend auf diesem Prinzip kann - in dem man Rausch-Messungen für verschiedene angelegte Spannungen durchführt - die Verarmungsspannung bestimmt werden. Bei der zweiten Methode wird die ausgelesene Ladungsmenge von Treffern rekonstruierter Teilchenspuren in Abhängigkeit der angelegten Betriebsspannung analysiert. Hierbei wird eine zuvor generierte Kurvenschaar den Signal-über-Spannungs-Kurven angepasst. Auf diese Weise wird die Verarmungsspannung bestimmt. Die Kurvenschaar wurde dabei basieren auf den geometrischen Gegebenheiten, sowie einem physikalischen Modell berechnet. Beide Messverfahren wurden getestet und mit Referenzwerten - die im Labor während der Produktion des Trackers gemessen wurden - verglichen. Auf Grund ihrer Eignung zur Bestimmung der Depletionsspannung, wurden beide Methoden als Messverfahren für den Detektor akzeptiert, und werden regelmäßig durchgeführt.

Basierend auf dem heutigen Verständnis der Strahlenschädigung wurde zudem ein Programm entwickelt, das die Veränderung der Sensoreigenschaften unter Bestrahlung für alle Module im Tracker simuliert, wobei simultan zur Bestrahlung die verschiedenen Ausheilprozesse berücksichtigt werden. Als Eingabge dafür wird lediglich das Strahlungsprofil sowie die Temperaturen - mit der Genauigkeit von Tagen - benötigt. Die Simulationen wurde mit den gemessenen Leckstrom-Veränderungen verglichen, wobei die relative Abweichung im Durchschnitt unter 7% ist, und keine Diskrepanz vom bisherigen Strahlenschädigungsmodells beobachtet werden kann.

Zusätzlich wurde das Programm genutzt um Prognosen für die Entwicklung der Sensoreigenschaften zu berechnen. Dabei wurde ein besonderes Augenmerk auf den Einfluss von Veränderungen in der Kühlung des Detektors auf die zukünftigen Eigenschaften gesetzt. Es wurde herausgestellt, dass eine Verbesserung der Kühlung nach der Wartungsperiode in 2013 und 2014 unumgänglich ist. Insgesamt muss bis zum Ende der Laufzeit der Phase 1, die Ende des Jahres 2021 geplant ist, die Kühlung bis auf -20° C verbessert werden. Dies kann jedoch schrittweise Erfolgen und sich dem jeweiligen Strahlungsausmaß anpassen.

In einem weiteren Kapitel wird der Einfluss der Strahlenschädigung auf die Datenqualität abgeschätzt, die basierend auf unseren Annahmen bis über die geplanten 10 Jahre Laufzeit hinaus exzellent sein wird. Unter Berücksichtigung einer vorgesehenen

vierten Lage im Pixel-Detektor kann die Spurrekonstruktion - trotz eines potentiellen Ausfalls von 674 Modulen deren thermischer Kontakt beeinträchtigt ist - im Vergleich zu heute sogar noch verbessert werden.

In einem letzten Kapitel wird ein Resümee über die Arbeit gezogen. Dabei wird aufgezeigt, dass mit den in dieser Arbeit vorgestellten Werkzeugen die Grundlagen zur Vertiefung unseres Verständnisses von Strahlenschädigungsphänomenen geschaffen wurden.

Performance of the CMS Tracker under Irradiation

Contents

Introduction

For millennia, it has been a driving force for mankind to improve the understanding of the structure of matter and the natural laws governing its interactions. However, it was only during the last decades that particle physics has experienced a great leap forward. With the development of particle accelerators we entered a new era of high-energy physics and paved the way for a comprehensive understanding of elementary particles and the fundamental interactions forming the Standard Model of particle physics [GaGrSc]. Many new insights in this field have been found within the last century, not least due to the huge progress in the development of sophisticated measurement equipment. While early accelerators like the Cockcroft-Walton generator are only capable of creating energies up to 1 MeV, a state of the art accelerator like the *Large Hadron Collider* (LHC) at CERN is able to reach energies of up to 8 TeV and is expected to increase this center of mass energy within the coming years up to 14 TeV. Furthermore, the recent luminosity $\mathcal{L}$ of the LHC, directly connected to the event rate $R = \sigma\mathcal{L}$, is higher than the luminosity achieved by any hadron collider so far. High energies and event rates are essential to investigate rare processes in high mass regimes. However, these conditions make great demands on the detecting devices. The *Compact Muon Solenoid* (CMS), one of the two big experiments at the LHC, is a huge instrument of more than 14000 tons of weight. Densely packed with sensors, electronics and support structures, it is certainly one of the most complex devices ever built by mankind.

With more than 200 m^2 active area, the innermost sub detectors of CMS form the world's largest silicon detector. Its task is to track the particle trajectories within the strong magnetic field of a solenoid. The advantages of silicon-based detecting devices are manifold: they are accurate in the spatial resolution (resolutions in the order of μm), fast in reading out the signal, resistant to radiative environments and last but not least affordable. Despite the radiation tolerance of silicon, there are many ways how traversing particles can damage the sensors and influence the macroscopic sensor properties. The main effects are an increase in the leakage current and a change of the full depletion voltage. The leakage current has an impact on the sensor's noise level and can thus influence a central quantity: the hit efficiency. The leakage current values are also limited by the finite capabilities of the power supply and the cooling system. The full depletion voltage defines the minimal bias voltage that needs to be applied to a sensor, in order to allow for the read-out of the full signal. The limitations are again the power supply and the cooling system. The CMS strip tracker was designed to withstand the amount of irradiation expected during more than 10 years of operation.

It is the central research topic of this thesis to estimate how the alteration of the sensor properties under irradiation and aging match the model expectations. One important aspect is how the thermal conditions, which deviate essentially from the design values, affect the evolution of the leakage current and full depletion voltage in the long run. Based on this study, projections for the macroscopic detector properties are presented for different cooling scenarios.

The first chapter of this work is dedicated to our current understanding of particle physics, the so-called Standard Model. The Standard Model has been thoroughly tested during many years and is in good agreement with all measurements. Based on this theory one particle has been postulated in the 1960s [PHiggs, EngBro, GuHaKi] For this Higgs boson a conclusive evidence has been found for the first time this year. The Higgs mechanism explains how elementary particles acquire mass. The search for this particle and its study is one of the central tasks among the LHC experiments. In addition, physics beyond the Standard Model is a mayor effort of CMS. One prominent example for a current field of research is the *supersymmetry*. In the second chapter, the basic principles of silicon detectors are introduced. A special focus is put on the radiation damage and aging of the silicon bulk and their impact on macroscopic properties namely the full depletion voltage and the leakage current. The third chapter gives a survey of the LHC experiments with a particular attention payed to the CMS strip tracker.

The second main part of this thesis details the study of radiation damage phenomena at the CMS strip tracker during the first years of operation. In chapter four the simulated fluence exposure of the tracker is discussed. Chapter five and chapter six are dedicated to the sensors' leakage current and full depletion voltage respectively. This covers a presentation of the developed in-situ measurement techniques as well as an extensive analysis of the evolution of the sensor's properties during the first years of data taking. In chapter seven, a software tool for the computation of sensor properties' evolution under irradiation is introduced. In chapter eight, a variety of projections of the sensor properties for future conditions is presented - evaluated with respect to the impact of modifications of the cooling conditions. In chapter nine, considerations about the influence of changing sensor properties on the physics performance of the tracker are made. In a final chapter, a conclusion about the status of this research at the CMS tracker is drawn. In addition, an outlook of the ongoing and planned activities is given.

Chapter 1

Particle Physics Quests of the LHC Experiments

1.1 The Standard Model

1.1.1 Brief Summary of the Standard Model

Our current understanding of the elementary particles and the fundamental interactions is forming the Standard Model of particle physics. It gives an elegant structure to the elementary particles by introducing the concepts of quarks and leptons which may be further divided into fermions (listed in 1.1) and force carriers the so-called *gauge bosons* (listed in 1.2). This quantum field theory also describes the electro-weak and strong force.

Predictions of various phenomena, like the existence of the charm quark, were based on principles of the standard model, even before their experimental discovery. So far, all high precision measurements and higher order theoretical calculations are in very good agreement with each other.

	I Generation	II Generation	III Generation
Quarks	Up (u) Down (d)	Charm (c) Strange (s)	Top (t) Bottom (b)
Leptons	Electron (e^-) Electron neutrino (ν_e)	Muon (μ^-) Muon neutrino (ν_μ)	Tauon (τ^-) Tauon neutrino (ν_τ)

Table 1.1: List of fundamental fermions.

Force	Strong Force	Weak Force	Electromagnetic Force
Boson	g	Z^0, W^{+-}	γ

Table 1.2: List of gauge bosons.

The underlying symmetry of these forces can be written as

$$S = SU(3)_C \otimes SU(2)_L \otimes U(1)_Y, \tag{1.1}$$

with $SU(3)_C$ being the symmerty underlying the Quantum Chromodynamics (QCD) theory of the strong interaction and $SU(2)_L \otimes U(1)_Y$ describing the symmetry of the electroweak interaction. A detailed description of the standard model would be beyond the scope of this thesis; the interested reader may consult [PesSch] for further reading.

The total number of free parameters of the standard model is 19: the masses of the three leptons and the six quarks, the three gauge couplings of equation 1.1, three CKM mixing angles between the weak eigenstates and the mass eigenstates of the quarks, one CP violating phase for the electroweak interaction, one parameter defining the strength of the CP violation for the QCD and two parameters related to the Higgs mechanism (see subsection 1.1.2).

Despite the predictibility of the standard model, the theory is not complete in the sense that it is missing a comprehensive explanation of many observations like gravitation, dark energy, dark matter and neutrino oscillations. Also, various so-called fine-tuning problems emerged within the model. Fine-tuning problems are characterized by the need to adjust certain parameters very precisely in order to match the experimental results. Prominent examples are the strong CP problem and the hierarchy problem. The first is based on the fact that, in contrast to the weak interactions, all experimental results do not show any CP violation of the strong interaction, even though no known mechanism suppresses the strong CP violation. The latter problem is related to large discrepancies between fundamental standard model parameters and their radiative corrections. One important example is the mass of the Higgs boson.

It is a hope of many physicists that the Standard Model is valid at all scales. However, radiative corrections to the Higgs mass are at the order of Λ^2 so that a Higgs mass in near the cutoff scale $\Lambda \simeq 10^{16}$ GeV is expected. On the other hand, a Higgs mass around of 100 GeV is preferable in order to give the correct masses to the W and Z boson. Thus, precise cancellations need to take place in order to achieve the balance between these two requirements. In general, fine-tuning problems do not falsify the standard model, yet they suggest that some pieces of the puzzle are still missing.

1.1.2 The Higgs Mechanism

Two of the four gauge bosons are known to be heavy ($M_W \simeq 80$ GeV, $M_Z \simeq 91$ GeV). However, mass terms are not allowed in the Standrad Model, since they violate gauge

invariance [PesSch]. The only way to obtain masses for gauge bosons is by interactions, in this case to the so-called Higgs-field.

We consider a complex scalar field coupled to itself and an electromagnetic field:

$$\mathcal{L} = -\frac{1}{4}(F_{\mu\nu})^2 + \mid D_\mu\phi \mid^2 - V(\phi), \tag{1.2}$$

with $D_\mu = \partial_\mu + ieA_\mu$. This Lagrangian is invariant under the local $U(1)$ transformation

$$\phi(x) \to e^{i\alpha(x)}\phi(x),\ A_\mu(x) \to A_\mu(x) - \frac{1}{e}\partial_\mu\alpha(x). \tag{1.3}$$

The potential can be chosen to be:

$$V(\phi) = -\mu^2\phi^*\phi + \frac{\lambda}{2}(\phi^*\phi)^2, \tag{1.4}$$

with a non zero vacuum expectation value of $< \phi >= \phi_0 = \left(\frac{\mu^2}{\lambda}\right)^{1/2}$ for $\mu^2 > 0$. The two parameters related to the Higgs mechanism mentioned in subsection 1.1.1 are μ and λ. If we decompose the complex field around the minimum of the potential as

$$\phi(x) = \phi_0 + \frac{1}{\sqrt{2}}(\phi_1(x) + i\phi_2(x)), \tag{1.5}$$

the global symmetry is no longer apparent and we speak of a spontaneously broken symmetry. Thus the potential (1.4) can be written as

$$V(\phi) = -\frac{1}{2\lambda}\mu^4 + \frac{1}{2}\cdot 2\mu^2\phi_1^2 + \mathcal{O}(\phi_i^3), \tag{1.6}$$

giving the ϕ_1 field the mass $m = \sqrt{2}\mu$. The field ϕ_2 can be identified with the massless Goldstone boson which needs to appear when a continuous symmetry is spontaneously broken according to the Goldstone theorem (see [GoSaWe]).

The Higgs mechanism uses a similar but more generic approach. We investigate the scalar fields ϕ_i that are invariant under a symmetry group G with the transformation

$$\phi_i \to (1 + i\alpha^a t^a)_{ij}\phi_j. \tag{1.7}$$

If we choose ϕ_i as real-valued fields, all matrices t^a must be pure imaginary and thus we can write

$$t^a_{ij} = iT^a_{ij}, \tag{1.8}$$

with T^a being real and antisymmetric. With G being a local gauge symmetry, the covariant derivative on ϕ_i is

$$D_\mu\phi = (\partial_\mu - igA^a_\mu t^a)\phi = (\partial_\mu + gA^a_\mu T^a)\phi. \tag{1.9}$$

The kinetic energy term for ϕ_i is then given by

$$\frac{1}{2}(D_\mu\phi_i)^2 = \frac{1}{2}(\partial_\mu\phi_i)^2 + gA^a_\mu(\partial_\mu\phi_i T^a_{ij}\phi_j) + \frac{1}{2}g^2A^a_\mu A^{b\mu}(T^a\phi)_i(T^b\phi)_i. \tag{1.10}$$

We can identify the last term in 1.10 with a mass term for the gauge bosons, while keeping in mind that ϕ_i acquires the vacuum expectation values

$$< \phi_i >= (\phi_0)_i. \tag{1.11}$$

Using this, we can write

$$\Delta\mathcal{L} = \frac{1}{2} m_{ab}^2 A_\mu^a A^{b\mu}, \tag{1.12}$$

with the mass matrix

$$m_{ab}^2 = g^2 (T^a \phi_0)_i (T^b \phi_0)_i. \tag{1.13}$$

The mass matrix is positive semidefinite and the diagonal elements have the form

$$m_{aa}^2 = g^2 (T^a \phi_0)^2 \geq 0. \tag{1.14}$$

This approach is able to explain the mass terms of the gauge bosons while also keeping the possibility of a massless gauge boson (with $T^a\phi_0 = 0$) physically represented by the photon. The Goldstone bosons manifest themselves in the second term of equation 1.10. Taking the vacuum expectation value into account, this leads to

$$\Delta\mathcal{L} = g A_\mu^a \partial_\mu \phi_i (T^a \phi_0)_i, \tag{1.15}$$

with ϕ_i being the Goldstone bosons.

This mechanism of spontaneous symmetry breaking explains the acquisition of mass for gauge bosons. It was explored by Higgs, Kibble, Guralnik, Hagen, Brout and Englert, and is nowadays known as the *Higgs mechanism* [PHiggs, EngBro, GuHaKi]. The key part is the non zero vacuum expectation of the potential, which allows an explanation of the fermion masses in a gauge-invariant way.

1.1.3 Theoretical Prediction of the Higgs Boson

In this context, the search for a more direct manifestation of the Higgs mechanism in form of a physical particle is the logical next step. One candidate for this would be the Goldstone boson. However, this can be ruled out easily, by transforming the Lagrangian (equation 1.2) into the so-called *unitarity gauge*. Thus, it is possible to eliminate the ϕ_2 terms leading to

$$\mathcal{L} = -\frac{1}{4}(F_{\mu\nu})^2 + (\partial_\mu \phi)^2 + e^2 \phi^2 A_m u A^\mu - V(\phi). \tag{1.16}$$

A different approach parametrizes the scalar field ϕ in the following way

$$\phi(x) = U(x) \frac{1}{\sqrt{2}} \begin{pmatrix} 0 \\ v + h(x) \end{pmatrix}, \tag{1.17}$$

with the real-valued fluctuating field $h(x)$ with $< h(x) >= 0$. Given an explicit renormalizable Lagrangian with a vacuum expectation like

$$\mathcal{L} =\mid D_\mu\phi \mid^2 +\mu^2\phi^\dagger\phi - \lambda(\phi^\dagger\phi)^2. \tag{1.18}$$

In the unitary gauge, we can express the terms of the potential energy with the position of the minimum at $v = \left(\frac{\mu^2}{\lambda}\right)^{1/2}$ in the form

$$\begin{aligned} \mathcal{L} &= -\mu^2h^2 - \lambda v h^3 - \frac{1}{4}\lambda h^4 & (1.19)\\ &= -\frac{1}{2}m_h^2h^2 - \sqrt{\frac{\lambda}{2}}m_h h^3 - \frac{1}{4}\lambda h^4. & (1.20) \end{aligned}$$

The quantum of the $h(x)$ field is a scalar particle with the mass

$$m_h = \sqrt{2}\mu = \sqrt{2\lambda}v. \tag{1.21}$$

This particle is called *Higgs boson* and providing evidence of its existence is one of the central goals of the LHC experiments at CERN.

1.1.4 Experimental Search for the Higgs Boson

In subsection 1.1.3 it was shown that, according to the Standard Model, a Higgs boson needs to exist. In mid 2012, both CMS [Obs125] and ATLAS published a paper reporting the observation of a new boson at around 125 GeV mass, which is compatible with the Higgs boson of the Standard Model. There are several possibilities to create the Higgs boson commonly referred to as channels. The largest channel at the LHC is the gluon-gluon fusion. Other important channel being the vector boson fusion, Higgsstrahlung and $t\bar{t}$ associated production. The tree level Feynman graphs of these production channels are shown in figure 1.1.

Higgs production channels

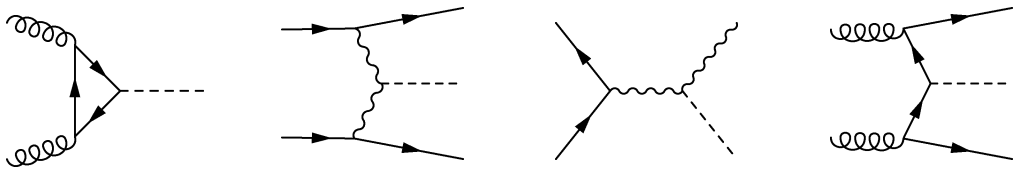

Figure 1.1: Feynman diagrams of Higgs production channels at tree level. From left to right: gluon-gluon fusion, vector boson fusion, Higgsstrahlung and $t\bar{t}$ associated production.

One criterion for the importance of a specific channel is the cross section of the channel and thus the rate with which the Higgs boson is produced. The cross section is strongly

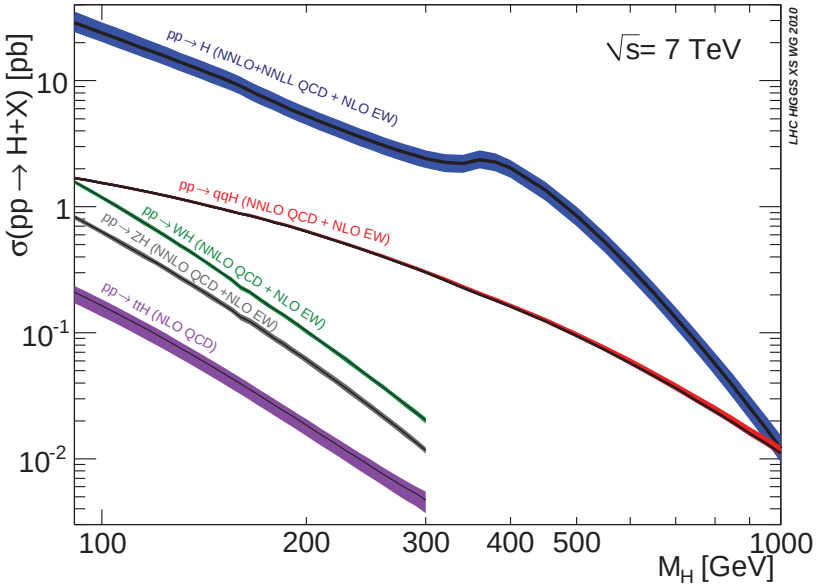

Figure 1.2: Cross sections for different Higgs production channels computed for pp collisions at a center of mass energy of 7 TeV as a function of the Higgs boson mass. Taken from [LHCSWG].

dependent on the actual Higgs boson mass. In figure 1.2 the calculated cross sections for the different Higgs boson production channels of pp collisions at a center of mass energy of 7 TeV is depicted. The cross section also depends crucially on the beam energy $\propto E^2$. Thus an increases in beam energy of about 14% (from 7 to 8 TeV) enhance the cross section already by approximately 30% [Murray]. The ratio of the Higgs boson cross sections at 8 TeV and 9 TeV compared to the 7 TeV value is shown in figure 1.3.

Figure 1.4 shows, that the decay of the Higgs boson is sensitive to the Higgs mass. A summary of the main channels' branching ratios is shown in figure . The plot makes it evident, that different mass regimes demand different decay channels to focus on.

Beyond this, a profound knowledge of the background is important since most decay products are frequently produced in many physical reactions. For instance, in the low mass Higgs regime ($m_H < 140$ GeV), the dominant hadronic decay channel $H \to b\bar{b}$ is covered with a QCD background which is 5 orders of magnitude higher than the signal. Thus, rare channels like $H \to \tau\bar{\tau}$ and particularly $H \to \gamma\gamma$ are more promising to identify a significant Higgs signal. Since it is difficult to discriminate the τ leptons from QCD jets, the $\gamma\gamma$ decay mode is - even though it has a small branching ratio - the best candidate for low mass Higgs search.

In [Obs125], a local significance of 5 standard deviations at a mass of 125.3 $\pm$ 0.4 (stat.) $\pm$ 0.5 (syst.) GeV was found. The most significant channels are $\gamma\gamma$ and ZZ. In figure 1.5 the resonance in the $\gamma\gamma$ mass spectrum at 125 GeV is shown.

Given the high backgrounds of the interesting Higgs channels a precise particle identification is crucial. Additional details on how CMS approaches this challenges can be found in chapter 3.2.5.

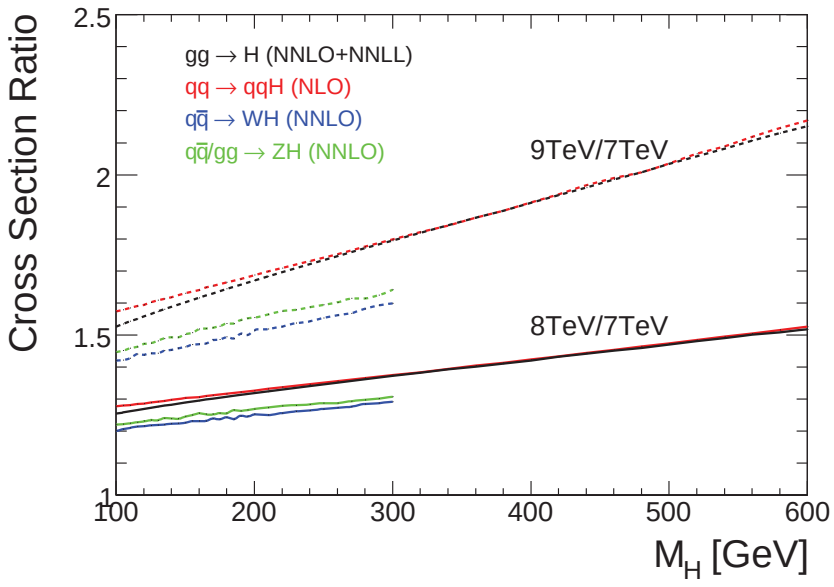

Figure 1.3: Dependence of the Higgs cross section on the beam energy. The ratios between the Higgs cross section at 8 TeV and 9 TeV beam energy to the 7 TeV value is plotted against the Higgs mass taken from [Murray].

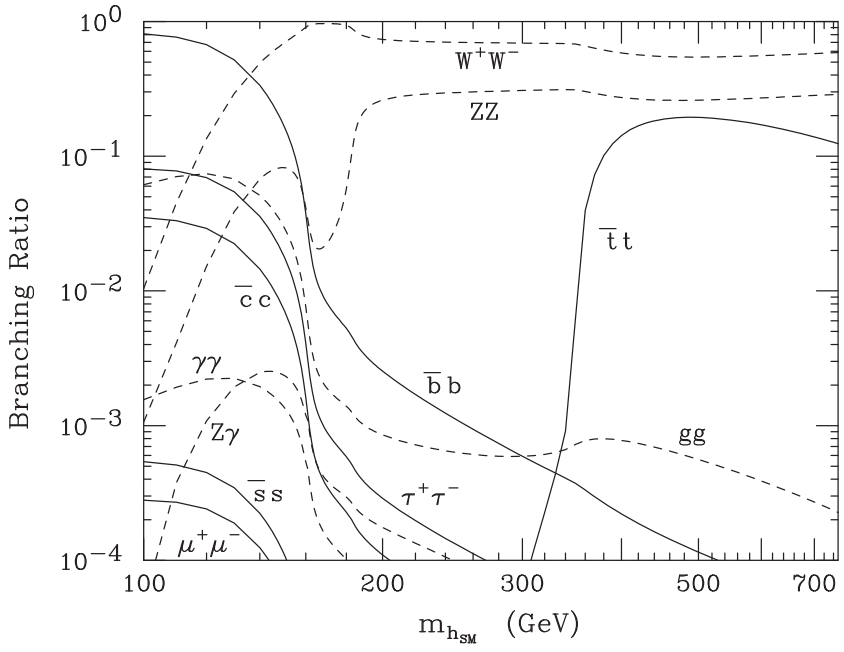

Figure 1.4: Branching ratios of different Higgs decay modes for the standard model Higgs boson as a function of the Higgs mass. Taken from [CarHab].

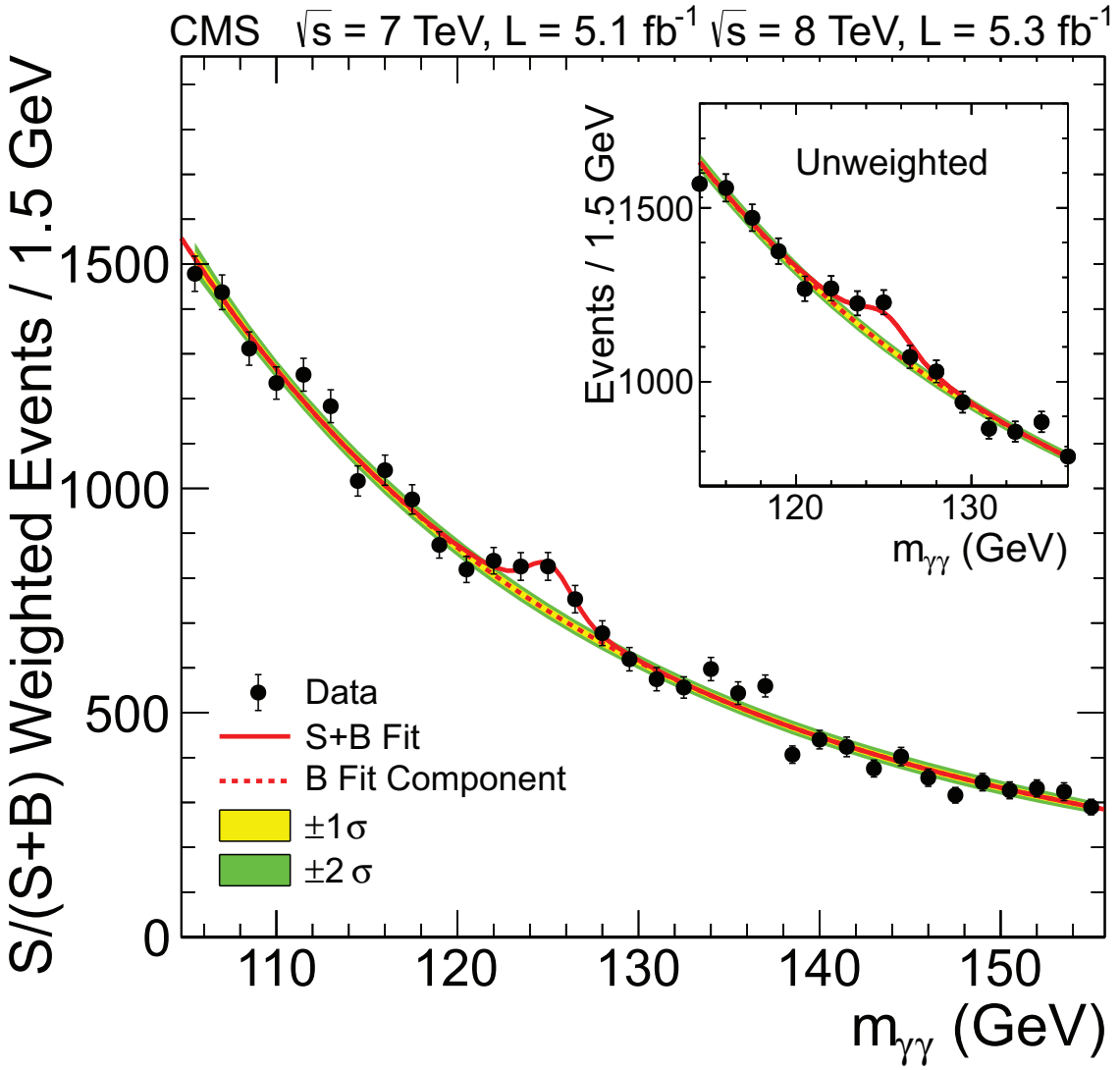

Figure 1.5: The invariant mass distribution of the diphoton spectrum measured by CMS is shown. The dashed line represents the fitted background. The colored bands are the one and two standard deviation uncertainty intervals on the background estimate. The red line is the fit of the background combined with the signal. In the large figure, each event is weighted with $S/(S+B)$ while the inset plot is unweighted. Taken from [CMSHIG].

1.2 Search for New Physics

Apart from proving the existence of the Higgs boson, the search for physics beyond the standard model is the main field of research at the LHC experiments. Since there are numerous theories which undergo extensive testing at the CERN experiments, an exhaustive overview is out of the scope of this work. The most prominent example of physics beyond the standard model is supersymmetry, which will be briefly discussed in the next subsection.

1.2.1 Supersymmetry

In supersymmetric (SUSY) models, each of the known particles have a supersymmetric partner, which has the same internal quantum numbers but the spin differs by one half. The mass region of the supersymmetric partner has to be substantially higher than for standard particles, since no SUSY particle has been found yet. Despite no experimental proof of supersymmetry over the last decades, the theory still has its appeal since it is able to explain several theoretical obstacles in an elegant manner.

A well known example is the *Grand Unification Theory* (GUT), in which the strong and electro-weak interactions are merged into a single interaction at high energy scales, the so-called GUT scale Λ_{GUT} [AmBoFü]. The convergence of the fundamental forces can be explained easily in supersymmetric models. Supersymmetric particles are also candidates for being the origin of dark matter, which still lacks a conclusive explanation. Moreover, the fine tuning problem mentioned in 1.1.1 can be avoided in SUSY models.

The downside of these promising theories is, apart from the still missing experimental proof, a large number of parameters that is needed to describe the model. Of the many different SUSY theories, the *Minimal Supersymmetric Standard Model* (MSSM) is the best studied.

Chapter 2

Silicon Strips Sensors

The development of silicon material for particle sensors started in the 1970's. Since then, enormous efforts have been made by many physicists and engineers around the world to optimize silicon sensor devices. Today, the silicon sensors stand out for their capability to track particles at high event rates with high resolutions while still being radiation tolerant.

Another important factor that contributed to the success of silicon detectors is the reasonable costs at which high quality silicon can be produced.

All these benefits made silicon detectors an essential part of almost all modern particle detectors. In the following passage a brief summary of silicon detecting devices is given.

2.1 Basic Principles of Silicon Particle Detectors

2.1.1 Physical Properties of Silicon

The semiconductor silicon used for building sensors is diamond blend with each atom having four covalently bound neighbors. Accordingly, they are labeled as group IV semiconductors. At first, the focus is put on pure silicon material which forms an intrinsic semiconductor. In order to explain the band structure of silicon, we need to develop the energy-momentum relationship and the concept of effective mass. According to the Bloch theorem, the solution of the Schrödinger equation for an approximate one-electron problem

$$\left[-\frac{\hbar^2}{2m^*}\nabla^2 + V(r)\right]\Psi(\vec{r},\vec{k}) = E(\vec{k})\Psi(\vec{r},\vec{k}) \tag{2.1}$$

is of the form of a Bloch function

$$\Psi(\vec{r},\vec{k}) = exp(i\vec{k}\cdot\vec{r})U_b(\vec{r},\vec{k}) \tag{2.2}$$

with the band index b and $\Psi(\vec{r},\vec{k})$ being periodic in $\vec{R}$ of the direct lattice.

It is a direct consequence of the Bloch theorem that the energy is periodic in the reciprocal lattice, i.e.: $E(\vec{k}) = E(\vec{k}+\vec{G})$. Thus, it is evident that one can reduce the investigated space to the Brillouin zone.

However, in order to study the band structure in detail, a numerical approach is necessary. A draft of the energy-band structure of silicon is shown in figure 2.1. The valence band is fully occupied at zero Kelvin while the conduction band is not, so that electrons being in the conductive band are mobile. Two phenomena contribute to the conductance of the material: firstly, the mobile electrons in the conduction band and secondly, the now-missing electrons in the valence band, resulting in the propagation of so-called holes. Depending on the shape of the energy band structure, one usually distinguishes between direct semiconductor and indirect semiconductor. Within a direct semiconductor the electron transition from the valence band to the conduction band does not require a change in momentum, while for the indirect semiconductor the lower end of the conduction band is shifted with respect to the upper boarder of the valence band in the momentum plane. This makes - in addition to the energy - a simultaneous change of momentum necessary for a transition between the two bands. Thus, an excited electron cannot recombine on its own, but requires an additional phonon providing it with the needed momentum change.

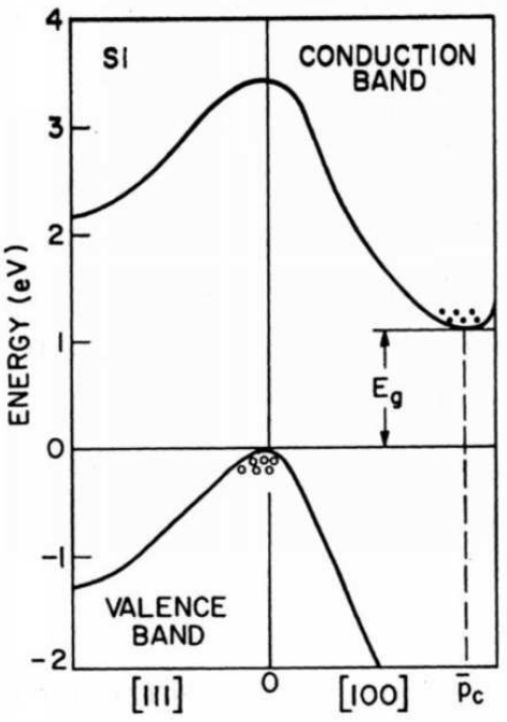

Figure 2.1: The energy-band structure of silicon as an indirect semiconductor, with E_g being the band gap [Lutz].

Near the band edges, the $E-k$ relationship can be approximated by a quadratic expression,

$$E(k) = \frac{\hbar^2 k^2}{2m^*}, \tag{2.3}$$

with m^* being the effective mass. The effective mass corresponds to the hypothetical mass of the particle if it were free. With the help of this concept, electrons and holes can be treated as classical charged particles.

The number of electrons in the conductive band is given by the number of allowed

states multiplied by the occupancy integrated over the whole band,

$$n = \int_{E_C}^{\infty} N(E)\mathcal{F}(E)dE. \tag{2.4}$$

The density near the bottom of the conduction band can be taken as an approximation for low-enough carrier densities and temperatures. According to [Pointo], this approach leads to

$$N(E) = \frac{\sqrt{2}}{\pi^2}\frac{m_n^{3/2}(E - E_C)^{1/2}}{\hbar^3}, \tag{2.5}$$

with m_n being the effective mass of the electrons.

The occupation probability of these electron states is given by the Fermi-Dirac function

$$\mathcal{F}(E) = \frac{1}{1 + \exp(\frac{E-E_F}{k_B T})} \tag{2.6}$$

with the Fermi energy E_F, the Boltzmann constant k_B and the temperature T.

With 2.4, 2.5 and 2.6 the density of free electrons in the conductive band can be written as:

$$n = \frac{2}{h^3}(2\pi m_n k_B T)^{3/2}\exp(-\frac{E_C - E_F}{k_B T}) = N_C \exp(-\frac{E_C - E_F}{k_B T}) \tag{2.7}$$

Similarly, we can obtain the hole density p in the valence band:

$$p = 2\frac{2\pi m_p kT}{h^2}^{3/2}\exp(-\frac{E_F - E_V}{kT}) = N_V \exp(-\frac{E_F - E_V}{kT}) \tag{2.8}$$

with the effective density of states in the valence band N_V. For intrinsic semiconductors the number of electrons and holes per unit volume is equal, leading to:

$$n = p = n_i \tag{2.9}$$

2.1.2 Donors and Acceptors

Impurities within the semiconductor bulk can introduce new energy levels within the band structure: the semiconductor becomes extrinsic. The purposeful introduction of impurities is called doping. If a silicon atom is exchanged with a group V atom like arsenic, the fifth electron has a low binding energy to its host and can become a conduction band electron at moderate temperatures. These types of impurities are called donors. When the donor doping is dominant the silicon is called n-type material. The doping with group III atoms like boron, leads already a low energies to the absorption of a single electron out of the valence band, which is then able to form a fourth covalent bond. In consequence, a positively charged hole is created. A dominant doping of this type leads to a p-type semiconductor and the corresponding impurities are called acceptors.

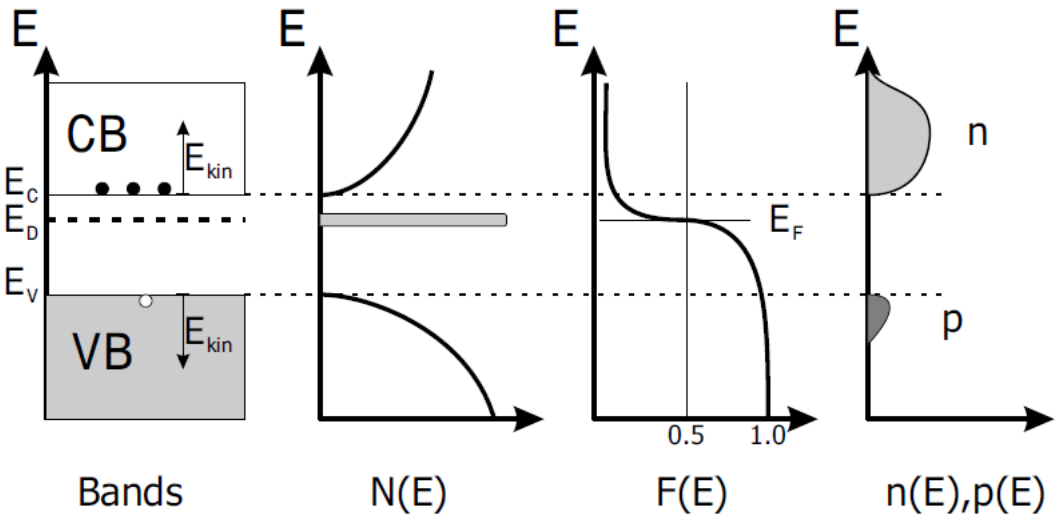

Figure 2.2: Sketch of basic silicon properties. On the left-hand side the band structure is drawn, with the valence band (VB) and the conduction band (CB). The density of states is shown in the second figure. The third figure shows the Fermi-Dirac function for silicon. The plot on the right shows the density of free charge carriers [Lutz]. The defect energy level E_D represents an additional energy level introduced by a donor.

At room temperature, all donors are ionized so that

$$n = N_D. \tag{2.10}$$

By using equation 2.7 we are able to obtain the Fermi level in terms of the effective density of states N_C and the donor concentration N_D:

$$E_C - E_F = kT \ln(N_C/N_D). \tag{2.11}$$

Equation 2.11 shows that, the higher the donor concentration, the closer the Fermi level will move towards the bottom of the conduction band. Similar considerations show that the higher the acceptor concentration, the closer the Fermi level will move towards the top of the valence band.

Following this approach, we can express the electron and hole densities in terms of the intrinsic carrier concentration n_i and the intrinsic Fermi level E_i:

$$n = n_i \exp(\frac{E_F - E_i}{kT}), \tag{2.12}$$

and

$$p = n_i \exp(\frac{E_i - E_F}{kT}). \tag{2.13}$$

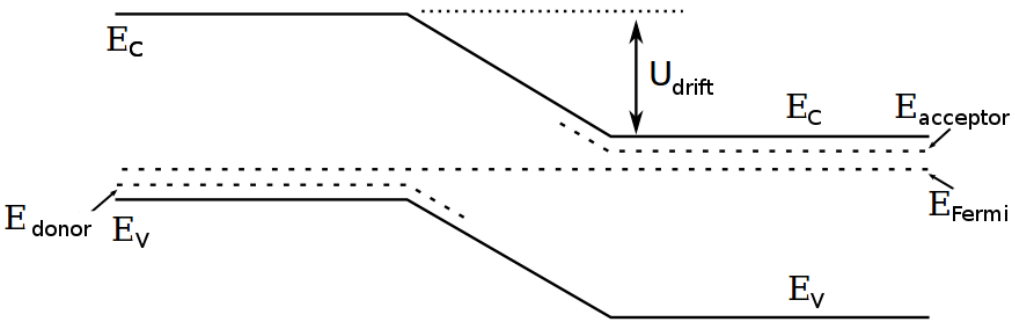

Figure 2.3: Schema of the energy band structure of a p-n-junction. The diffusion current flows from the n-type material (right-hand side) to the p-type material (left-hand side) within the conduction band, while the drift current in the conduction band flows from the p-type material to the n-type material. In the valence band, the directions are the opposite due to the opposite charge of the holes. The figure is taken from [WIKI].

The doping concentration has direct impact on the resistivity of the material. For materials dominated by one impurity type (e.g. N_i) the resistivity is given by:

$$\rho = \frac{1}{e\mu N_i}, \tag{2.14}$$

for the respective mobility μ.

2.1.3 The p-n Junction

In order to use semiconductors for particle tracking one needs to use the properties of the p-n junction. If a p-type and a n-type semiconductor are joined together, holes from the p-side diffuse into the n-side, and electrons from the n-side diffuse into the p-side. This space charge region creates an electric field resulting in a drift voltage U_{drift}. In equilibrium, the drift and diffusion currents are equal.

It is a direct consequence of the equilibrium state that the Fermi level must be constant:

$$\begin{aligned} J_n &= J_n(drift) + J_n(diffusion) \\ &= q\mu_n n\mathcal{E} + qD_n\frac{dn}{dx} \\ &= q\mu_n n\left(1/q\frac{dE_i}{dx}\right) + kT\mu_n\frac{dn}{dx} = 0, \end{aligned} \tag{2.15}$$

using the Einstein relation $D_n = (kT/q)\mu_n$, and the derivative of equation 2.12

$$\frac{dn}{dx} = \frac{n}{kT}\left(\frac{dE_F}{dx} - \frac{dE_i}{dx}\right). \tag{2.16}$$

This yields the net electron current density to

$$J_n = \mu_n n \frac{dE_F}{dx} = 0 \ , or \ \frac{dE_F}{dx} = 0. \tag{2.17}$$

In the transition area between the p-type and the n-type material, the mobile carrier density is zero. This is called the depletion region. The Poisson's equation for this region with $p = n = 0$ becomes:

$$\frac{d^2\psi}{dx^2} = \frac{q}{\epsilon_s}(N_A - N_D). \tag{2.18}$$

One can simplify this expression to:

$$\frac{d^2\psi}{dx^2} = \frac{qN_A}{\epsilon_s}, \ for \quad -x_p \leq x < 0, \tag{2.19}$$

$$\frac{d^2\psi}{dx^2} = -\frac{qN_D}{\epsilon_s}, \ for \ \ 0 < x \leq x_n, \tag{2.20}$$

with x_p and x_n being the borders of the depletion region, and $x = 0$ being the coordinate of the transition. Furthermore, overall space charge neutrality leads to:

$$N_A x_p = N_D x_n. \tag{2.21}$$

The total depletion width W is given by

$$W = x_p + x_n. \tag{2.22}$$

The electric field can be obtained by integrating equation 2.19:

$$\mathcal{E}(x) = -\frac{d\psi}{dx} = -\frac{qN_A(x + x_p)}{\epsilon_s}, \ for \quad -x_p \leq x < 0 \tag{2.23}$$

$$\mathcal{E}(x) = \frac{qN_D}{\epsilon_s}(x - x_n), \ for \ \ 0 < x \leq x_n. \tag{2.24}$$

The maximum of the field is located at $x = 0$ and is given by

$$\mathcal{E}_m = \frac{qN_D x_n}{\epsilon_s} = \frac{qN_A x_p}{\epsilon_s}. \tag{2.25}$$

The built-in potential V_{bi} can be obtained by integrating equation 2.23:

$$\begin{aligned} V_{bi} &= -\int_{-x_p}^{x_n} \mathcal{E}(x)dx = -\int_{-x_p}^{0} \mathcal{E}(x)dx|_{p-side} - \int_{0}^{x_n} \mathcal{E}(x)dx|_{n-side} \\ &= \frac{qN_A x_p^2}{2\epsilon_s} + \frac{qN_D x_n^2}{2\epsilon_s} = \frac{1}{2}\mathcal{E}_m W. \end{aligned} \tag{2.26}$$

With equation 2.26, the total width of the depletion region can be written as:

$$W = \sqrt{\frac{2\epsilon_s}{q}\left(\frac{N_A + N_D}{N_A N_D}\right) V_{bi}}. \tag{2.27}$$

When an external bias voltage is applied, the width of the depletion region can be controlled in the following way:

$$W = \sqrt{\frac{2\epsilon_s}{q}\left(\frac{N_A + N_D}{N_A N_D}\right) (V_{bi} - V_{bias})}. \tag{2.28}$$

A positive V_{bias} can reduce the depletion zone width (forward bias), while a negative bias voltage (reverse bias) enhances the depletion width.

Depletion of the silicon bulk is crucial in the construction of particle detectors, since only electron-hole-pairs only electron-hole-pairs generated by a traversing particle in the depleted region of the sensor can contribute to the read-out current. Therefore, the full depletion voltage - namely the value of the bias voltage from which onwards the complete bulk is depleted - is an important quantity.

For sensors, the built-in potential V_{bi}, which is in the order of Volts, can usually be neglected with respect to the applied bias voltage $V_{bi} \ll V_{bias}$. Generally the width of one side is much smaller than the width of the other side. At the CMS strip tracker the p-strip on n-type bulk technique is used ($N_A \gg N_D$ and thus $x_p \ll x_n$). This junction is called *one-sided abrupt junction*. For N_{eff} being the effective donor or acceptor concentration respectively within the silicon bulk, this leads to the full depletion voltage of a diode,

$$V_{dep} = \frac{qN_{eff}d^2}{2\epsilon}, \tag{2.29}$$

for a given thickness d of the bulk.

For a strip sensor the strip size is smaller than the pitch. According to [BaCaVi], this leads to a correction factor for the full depletion voltage. The semi analytical result yields:

$$V_{dep,sensor} = V_{dep} \cdot 1 + \frac{p}{d} f(\frac{w}{p}), \tag{2.30}$$

for the strip pitch p, the strip width w and the function f with the following form:

$$f(x) = -0.00111x^{-2} + 0.0586x^{-1} + 0.24 - 0.651x + 0.355x^2. \tag{2.31}$$

In order to determine the capacitance of the depletion region, the impact of an incremental charge dQ on the electric field $d\mathcal{E}| = dQ/\epsilon_s$ is derived from the Poisson's

equation. A change in the bias voltage dV can be approximated by $Wd\mathcal{E}$. Using these equations, the capacitance of the depletion region can be written as:

$$C = \frac{dQ}{dV} = \frac{dQ}{W\frac{dQ}{\epsilon_s}} = \frac{\epsilon_s}{W}. \tag{2.32}$$

Finally, one can express the capacitance in terms of the applied bias voltage by inserting equation 2.28 into 2.32:

$$C = \sqrt{\frac{q\epsilon_s N_{eff}}{2(V_{bi} - V_{bias})}} \sim \sqrt{\frac{q\epsilon_s N_{eff}}{2|V_{bias}|}}. \tag{2.33}$$

2.1.4 The Leakage Current

Another important quantity is the reverse current or leakage current of the p-n-junction. As mentioned above in subsection 2.1.1, the recombination of excited electrons is highly suppressed in silicon, since it is an indirect semiconductor. In real devices, the recombination time is dominated by the concentration of the trap level impurities in the material N_t, which are impurities introducing new energy levels E_t into the band structure. According to [Lutz] the so-called *generation lifetime* can be written as

$$\tau_L = \frac{1}{N_t}\left(\frac{\exp(\frac{\Delta_t}{k_B T})}{v_{tp}\sigma_p} + \frac{\exp(\frac{-\Delta_t}{k_B T})}{v_{tn}\sigma_n}\right), \tag{2.34}$$

with $\Delta_t = E_t - E_i$ being the energy difference between the trap level and the intrinsic Fermi level, v_{tp} and v_{tn} being the thermal velocity of electrons or holes respectively, and σ_p, σ_n being the trapping cross sections for electrons or holes.

In 1952, Shockley, Read [ShoRea] and Hall [Hall] were the first to propose the so-called SRH model for carrier recombination and lifetime. However, the very details are out of the scope of this thesis. The minimum of τ_L is reached when the trap levels are near to the intrinsic Fermi level E_i. Thus, the most effective current generation happens for these impurities. For these so-called *deep level impurities* N_{dl}, which introduce energy levels near to the mid of the band gap, the leakage current can be approximated using equation 2.34

$$I_L = \frac{1}{2}e\frac{n_i}{\tau_L}WA \approx \frac{1}{2}en_i\sigma v_{th}N_{dl}WA, \tag{2.35}$$

with A being the surface of the junctions.

In equation 2.7 it was shown, that the temperature dependence of n_i can be written as:

$$n_i(T) \propto T^{3/2}\exp\left(\frac{-E_g}{2k_B T}\right), \tag{2.36}$$

for a given temperature T with the band gap energy E_g and the Boltzmann constant k_B.

If we assume $v_{tp}\sigma_p \simeq v_{tn}\sigma_n$ and limit ourselves to energy levels near the intrinsic Fermi level, the temperature dependence of the recombination lifetime will become dependent on the thermal velocity alone, which is given by:

$$\tau_L \propto T^{-1/2}. \tag{2.37}$$

If we combine equation 2.36 and 2.37 we can parameterize the temperature dependency of the leakage current by:

$$I_L \propto T^2 \exp\left(-\frac{E_g + 2\Delta}{2k_B T}\right), \tag{2.38}$$

for a parameter Δ being approximately the absolute value of Δ_t. A.Chilingarov followed this ansatz using experimental data and found an effective band gap value for silicon of $E_{eff} = 1.21eV$ [Chilin]. With this value the final effective temperature scaling of the leakage current is given by:

$$I(T) \propto T^2 \exp\left(\frac{-1.21eV}{2k_B T}\right). \tag{2.39}$$

2.1.5 Energy Deposition of Charged Particles within the Sensor Bulk

When charged particles traverse the depleted sensor bulk, electron hole pairs are generated along the trajectory. The energy loss of heavy particles by ionization and excitation is given by the Bethe-Bloch formula:

$$-\frac{dE}{dx} = kz^2 \frac{Z}{A}\frac{1}{\beta^2}\left(\frac{1}{2}\ln(\frac{2m_e c^2\gamma^2\beta^2 T_{max}}{I}) - \beta^2 - \frac{\delta}{2} - \frac{C}{Z}\right), \tag{2.40}$$

with $k = 4\pi N_A r_e^2 m_e c^2 = 0.3071 \frac{\text{MeV}}{g/\text{cm}^2}$.

z - charge of the incident particle in units of the elementary charge.

Z, A - atomic number and atomic weight of the absorber.

m_e - electron mass.

r_e - classical electron radius.

N_A - Avogadro number ($6.022 \cdot 10^{23}\text{mol}^{-1}$)

$T_{max} = \frac{2m_e c^2\beta^2\gamma^2}{1=2\gamma m_e/M+(m_e/M)^2}$ - maximum kinetic energy transferred from a particle with mass M onto the electron.

I - mean excitation energy, which is about $(173 \pm 3)eV$ for silicon.

δ - parameter of the density effect, which describes how much the extended transverse electric field of the incident relativistic particle is screened by the charge density of the atomic electrons.

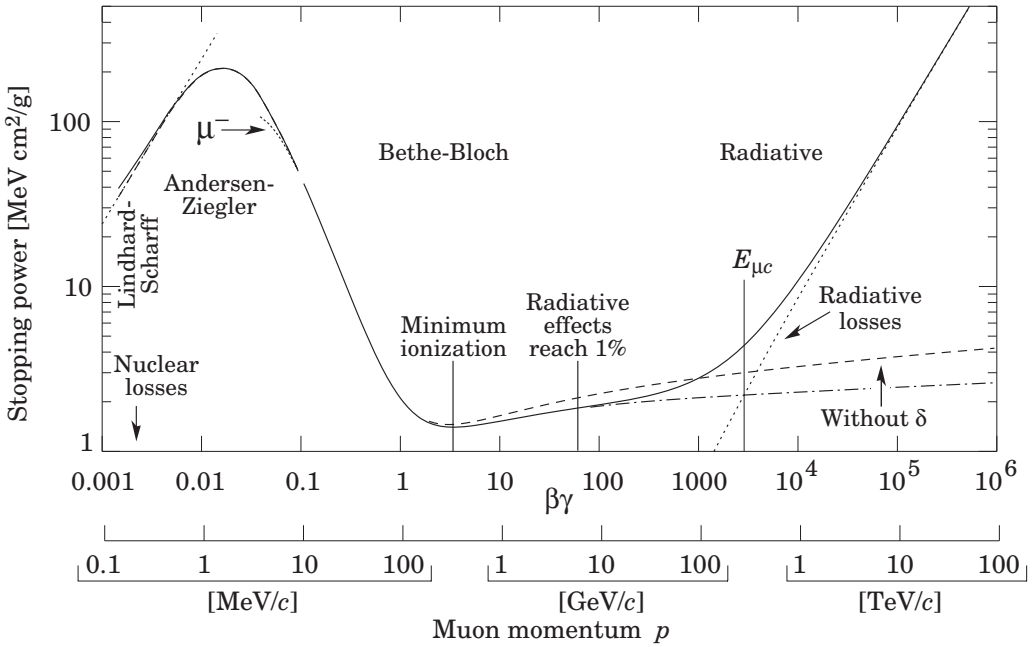

Figure 2.4: The stopping power of copper $\langle \frac{dE}{dx} \rangle$ versus the momentum of a traversing muon. The plot also includes corrections to low and high momentums, the discussion of which would be out of the scope of this overview. The point of minimum ionization is indicated in this plot at around 300 MeV. Image taken from [PDG].

$\frac{C}{Z}$ - Shell corrections for the assumption that the velocity of the bound electron is negligible compared to the velocity of the traversing particle.

The minimum of this curve indicates the momentum of minimal ionization. This is an important point, since detectors aim to achieve a good signal strength (and a high signal over noise value), even for minimum ionizing particles, so-called *MIPs*. One example for the differential energy loss is shown in figure 2.4.

Since the energy loss only depends on the velocity and not on the mass of the traversing particle, the $\frac{dE}{dx}$ versus momentum curves can be used to distinguish between different particles. Figure 2.5 shows an example of particle identification at the CMS strip tracker.

This approach utilizes that the Bethe-Bloch formula (2.40) can be linearized around m^2/p^2 in the restricted region of $\beta\gamma$ where the particle identification is possible

$$\langle \frac{dE}{dx} \rangle = K \frac{m^2}{p^2} + C \tag{2.41}$$

with the two free parameters K and C.

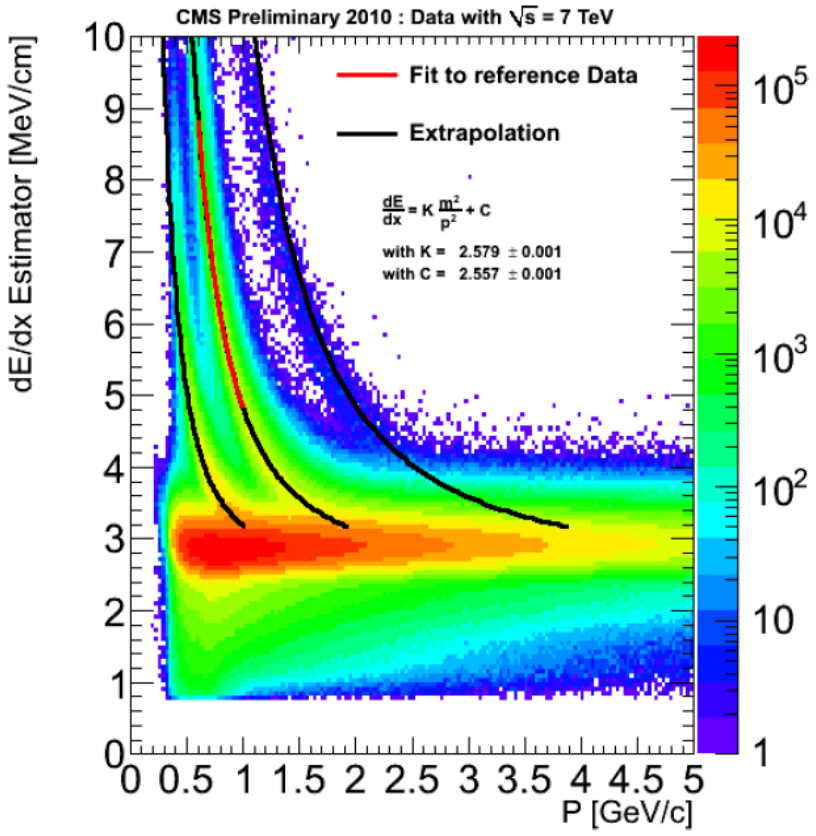

Figure 2.5: Example plot of particle identification by using the specific energy loss in the silicon strip tracker of CMS. The black extrapolated curves correspond to kaons, protons and deuterons. For this plot the most probable value of the energy loss is used since it is more stable than the mean value. The parameters K and C of equation 2.41 are derived from the fit, indicated by the red line. The figure is taken from [Quert].

The $\frac{dE}{dx}$ value in equation 2.40 gives the average energy loss of the charged particle. The energy loss in a real sensor bulk is a statistical process. Since collisions with small dE are more probable, the energy loss distribution in thin layers is highly asymmetric. It can be parametrized by a Landau distribution. Although strictly speaking, the mean of a Landau distribution is undefined, due to the long tail, one can use the concept for finite amount of entries. Note that the most probable value of the Landau distribution is smaller than the mean value of a given distribution. In contrast, the Bethe-Bloch formula (2.40) refers to the mean value.

By increasing the layer thickness or the density of the material, the distribution converges to a Gaussian distribution. According to [GruShw] the Landau parametrization can be written as

$$L(\lambda) = \frac{1}{\sqrt{2\pi}} \cdot \exp\left[-\frac{1}{2}(\lambda + e^{-\lambda})\right], \tag{2.42}$$

where λ characterizes the deviation of the actual energy loss from the most probable energy loss:

$$\lambda = \frac{\Delta E - \Delta E^W}{\xi}, \tag{2.43}$$

with ξ being proportional to the density and the thickness of the material. A characteristic Landau distribution is depicted in figure 2.6.

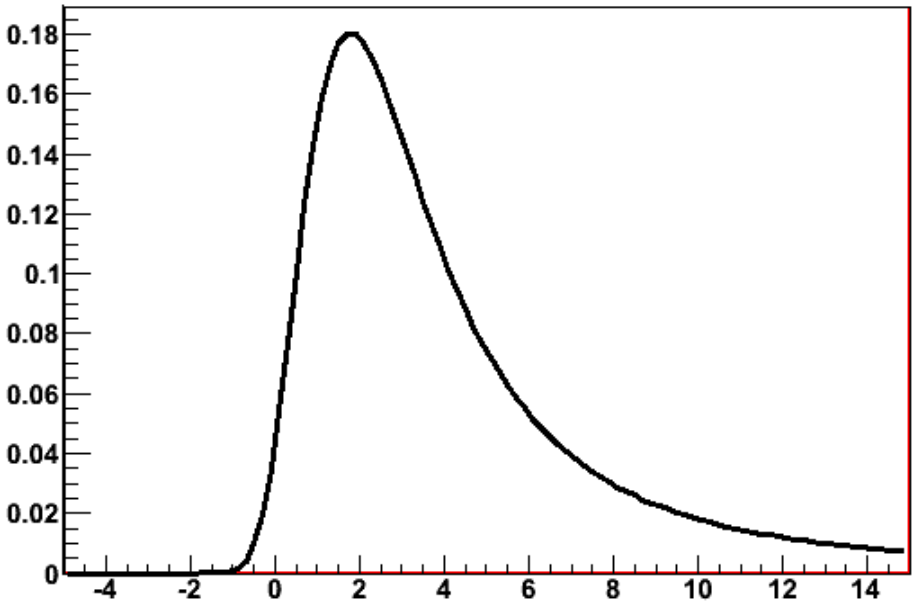

Figure 2.6: Example of a Landau distribution. The figure is taken from [WIKI].

2.1.6 Silicon Sensors Working Principle

Silicon sensors are essentially multiple p-n-junctions connected to an active plane. The main layouts are pixel sensors with a two dimensional resolution and strip sensors with only one dimensional resolution within each sensor. In figure 2.7, a schematic slice plane of a silicon strip sensor is shown to demonstrate the principle of a p-in-n type silicon sensor. The p-type strips are forming the p-n-junction together with the n-type bulk material.

The applied bias voltage in reverse direction is depleting the entire sensor bulk of free charge carriers. An ionizing particle creates electron-hole pairs in the sensor bulk, which are transported by the electric field to the backplane and the strips. The Al read-out strips are coupled capacitively to the sensor using the common AC read-out technique.

The pitch is the distance of two neighboring strips. It is an important quantity defining the resolution of a sensor according to [Zichin],

$$\sigma \propto \frac{\text{pitch} f}{\text{signal/noise}} \tag{2.44}$$

for analogue read-out with the factor f depending on the spread of the signal. In contrast, for the binary read-out the resolution can be written as:

$$\sigma \simeq \frac{\text{pitch}}{\sqrt{12}}, \tag{2.45}$$

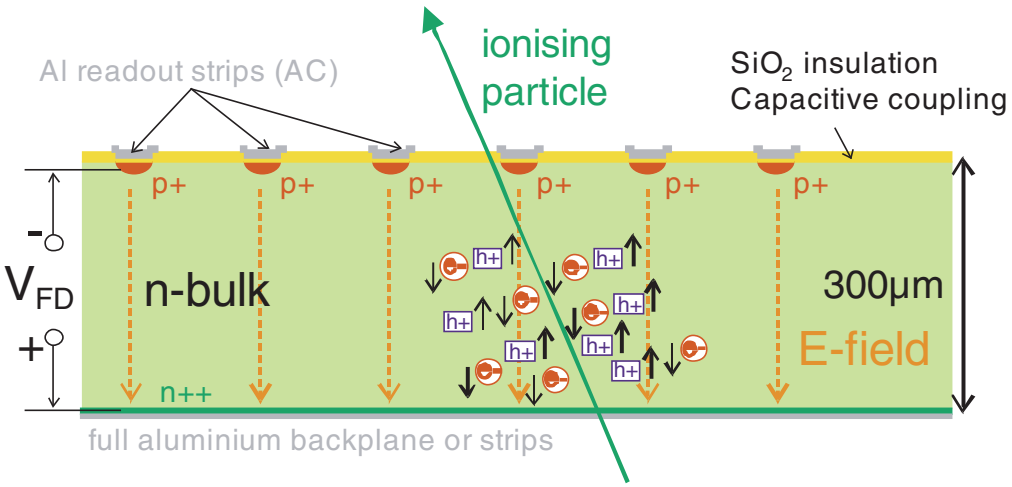

Figure 2.7: Working principle of an AC coupled strip sensor. The electron-hole pairs created by the ionizing particle are separated by the electric field in the sensor bulk. The holes are read-out at the p+ strips via capacitive coupling to the Al strips. The diagram is taken from [Hartma].

while considering:

$$\langle \Delta x^2 \rangle = 1/p \int_{-p/2}^{p/2} x^2 dx = \frac{p^2}{12}. \tag{2.46}$$

In equation 2.44 it is clearly visible that the resolution of a sensor benefits directly from a high signal over noise ratio. Even though the complete sensor bulk is depleted from free charge carriers during the operation of the sensor, several sources of statistical electron and hole fluctuations exist and contribute to the noise. Under the operational conditions of the tracker, the sensor's signal is limited by the charge created in the bulk. Consequently, the minimization of the noise value is an important aim.

If the electrical field inside the sensor bulk is exceeding a critical value, silicon sensors show a phenomenon called *charge multiplication*. In this case, more charge can be read out, than it has been initially generated. However, it should be noted that this critical value is far beyond the range of possible bias voltage settings of the CMS tracker. This effect is also used in avalanche photodiodes. It is dependent on the level of irradiation [Cassa].

Usually the noise is expressed as Equivalent Noise Charge (ENC) which corresponds to the number of electrons contributing to the noise. The total noise value is the square root of the squared sum of all independent noise sources. According to [Hartma], the different noise sources contributing to the final noise value are:

$$ENC = \sqrt{ENC_C^2 + ENC_{I_L}^2 + ENC_{R_P}^2 + ENC_{R_S}^2}, \tag{2.47}$$

with the capacitive term

$$ENC_C = a + b \cdot C_{strip} \tag{2.48}$$

forming the most important contribution. The parameters a and b are preamplifier specific, while C_{strip} is the total strip capacitance.

$$ENC_{I_L} = \frac{e}{2}\sqrt{\frac{I_L t_p}{q}}, \tag{2.49}$$

is the shot noise term from the leakage current, with the Euler number e the peaking time t_p and the electron charge q.

$$ENC_{R_P} = \frac{e}{q}\sqrt{\frac{k_B T t p}{2R_P}} \tag{2.50}$$

is the parallel thermal noise term from the bias resistance, with the Boltzmann constant k_B.

$$ENC_{R_S} = C_{strip}\frac{e}{q}\sqrt{\frac{k_B T R_S}{6t_p}}, \tag{2.51}$$

is the serial thermal noise from the metal strip resistance.

A bias ring connects all the strips to a single well defined potential. The bias voltage is applied between the bias ring and the backplane of the sensor.

A guard ring is usually used to shape the electric field inside the sensor volume and ensure a homogeneous field, especially for the strips at the edges of the sensor. There are different approaches to achieve this aim, but further details are beyond the scope of this thesis.

2.2 Radiation Damage in Silicon Particle Detectors

In a high radiative environment such as the region around an interaction point of the LHC, it is crucial to understand the impact of radiation on the detecting devices. Hence, an overview of radiation damage in silicon is given. An introduction to radiation damage phenomena in silicon sensors can be found, for example, in [Moll].

2.2.1 Bulk Damage

High energetic particles traversing the silicon bulk not only ionize the material as discussed in subsection 2.1.5, but also interact with the atomic bodies themselves. There are several final states of these interactions:

The atom is completely removed from its lattice position which forms a vacancy (V).

An atom is placed in between the usual lattice formation and forms an interstitial (I).

A combination of a vacancy and interstitial which is called *Frenkel pair*.

There are also higher orders of these defects like di-vacancies, di-interstitials etc. All these defects can also interact with the impurity atoms which are commonly present in the material, e.g. oxygen, carbon, phosphorus etc. Some examples of these lattice defects are shown in figure 2.8.

The maximum transferred energy $E_{R,max}$ can be approximated for particles with mass m_p and kinetic energy E_p:

$$E_{R,max} = \frac{2m_{Si}E_p(E_p + 2m_pc^2)}{(m_p + m_{Si})^2c^2 + 2m_{Si}E_p}. \tag{2.52}$$

The differences in the average recoil energy are even more pronounced. In table 2.1 the maximum and average recoil energy for different particle types is shown. The long ranging Coulomb force favors small energy transfer, while the nuclear interactions tend to deposit higher amounts of energy.

	Electron	Proton	Neutron
Force	Coulomb	Coulomb and nuclear	Elastic nuclear
$E_{R,max}$ [keV] / $E_{R,avg}$ [keV]	0.155 / 0.046	133.7 / 0.21	133.9 / 50

Table 2.1: Maximum and average energy transfer for different particle types with 1 MeV kinetic energy onto silicon material.

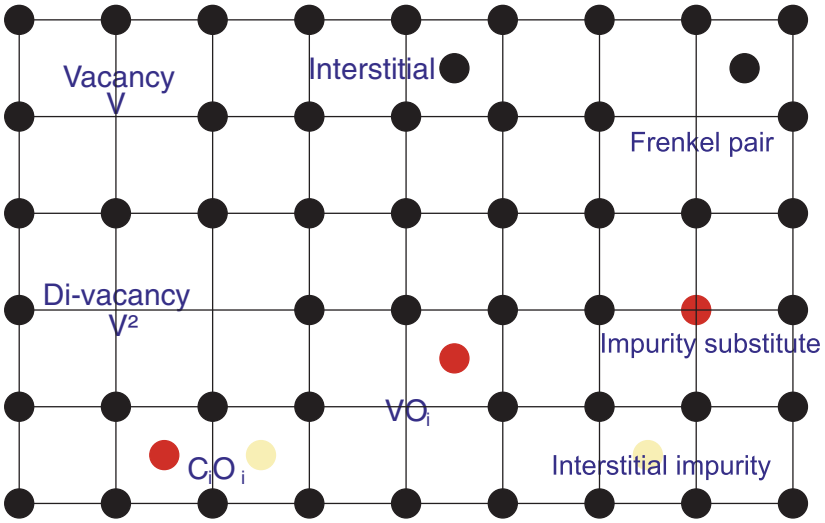

Figure 2.8: Examples of lattice deformations induced by particle radiation. Impurity clusters are labeled with their atomic sign in combination with an index indicating whether it is a substitute (S) or interstitial (I). The modified lattice structure has an impact on the energy scheme of the semiconductor and thus affects the general properties of the sensor. This figure is taken from [Hartma].

The threshold displacement energy for the different defect types is approximately $E_{pointdefect} \approx 25$ eV for point defects and $E_{cluster} \approx 5$ keV for cluster defects. Therefore low energy transfers lead to point defects, whereas high energy transfers lead mostly to cluster defects.

In figure 2.9 a simulation of the path of a primary knock on atom with the resulting cascade of vacancy displacements is shown for a 1 MeV neutron irradiation. This is a typical energy in the highly energetic radiation environment at the LHC. One can clearly see the formation of vacancy clusters.

The defects form new energy levels in the band structure of the semiconductor, this affects also the macroscopic properties of the silicon sensors. The influenced quantities are mainly:

- Increase of leakage current (primarily induced via energy levels near the mid of the band gap, see subsection 2.1.4)
- Modification of the full depletion voltage due to a change of N_{eff}, the effective doping concentration (mainly induced via energy levels near the conduction and valence band, see subsection 2.1.2)
- Decrease of the charge collection efficiency due to so-called traps

A schematic depiction of these effects can be found in figure 2.10.

Radiation Induced Leakage Current

The experimentally well confirmed relation between radiation and the increase in leakage current is given by:

$$\Delta I = \alpha(t, T)\Phi_{eq}V \tag{2.53}$$

for a normalized particle fluence Φ_{eq} and a volume V. The $\alpha(t, T)$ parameter is called the *current related damage rate*. A more extensive discussion about the leakage current evolution is given in subsection 2.2.3.

Radiation Induced Change in Depletion Voltage

For the effective doping concentration the situation is more complex. For $n - type$ bulk material, like it is used in the CMS strip tracker, a combination of the creation of acceptor impurities and the removal of donors takes place. Examples are the formation of $V + V + O \rightarrow V_2O$ and $P + V \rightarrow VP$, respectively. During irradiation, the bulk becomes more and more a $p-$like material. When the acceptors exceed the donors, the material "type inverts". Since the depletion voltage is proportional to the effective doping concentration (see equation 2.29), the full depletion voltage first drops and then rises again after the type inversion has taken place. Since annealing effects are crucial to describe the change in depletion voltage quantitatively, a detailed elaboration is provided in subsection 2.2.3.

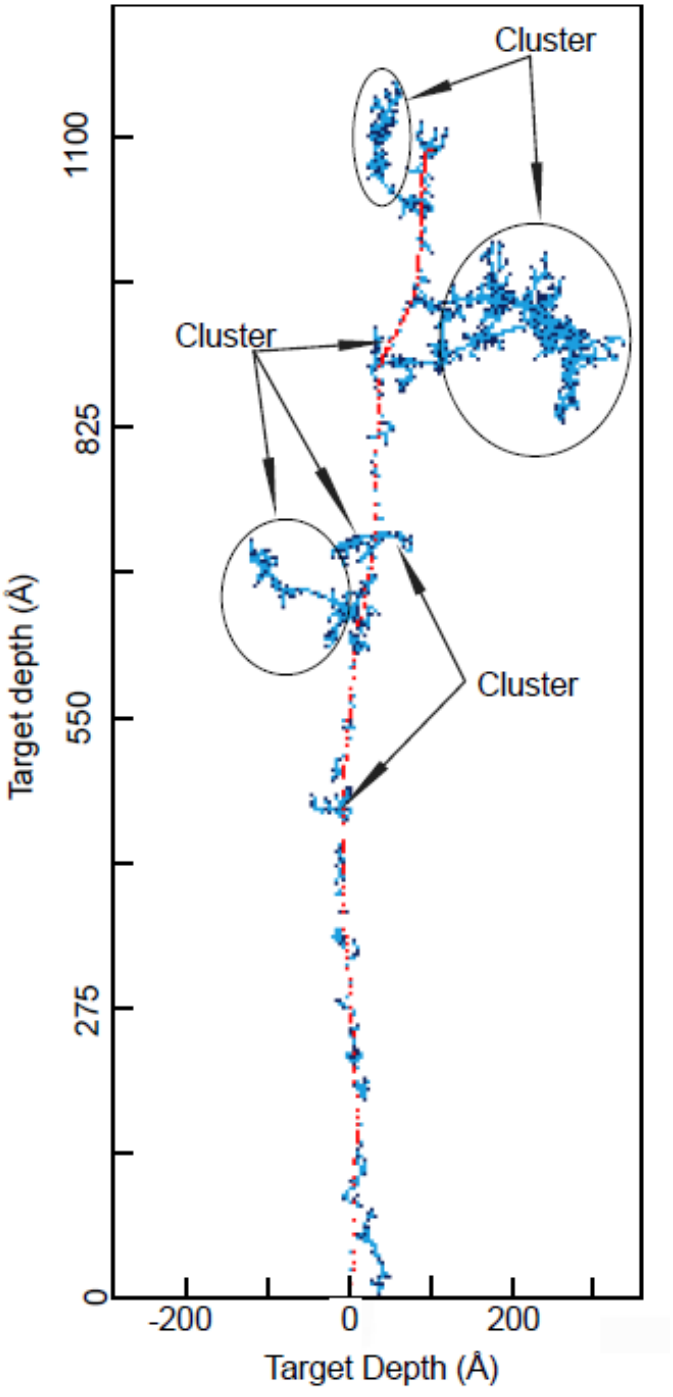

Figure 2.9: Simulation of the path of a primary knock on atom (indicated by the red dots), creating a cascade of vacancies (marked with blue dots) throughout the silicon material. The cluster regions are found at the end of the cascades. The figure is taken from [Junkes].

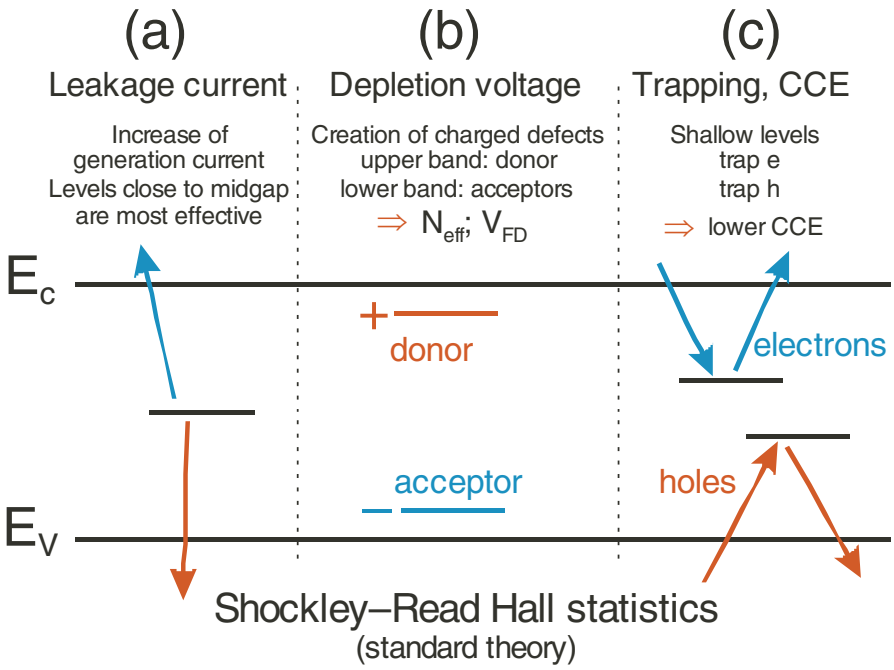

Figure 2.10: The different energy levels introduced due to radiation affect different macroscopic properties depending on their position within the energy band gap. Energy levels near the mid of the band gap mainly contribute to the leakage current (a). Energy levels near the conductive and valence band mainly affect the full depletion voltage (b). Deep levels with long trapping time, compared to the read-out time, reduce the charge collection efficiency (c). The figure is taken from [Hartma].

Charge Trapping Due to Irradiation

The trapping probability is proportional to the concentration of unoccupied trapping centers N_i and can be written as

$$\frac{1}{\tau_{eff}} = \sum_i N_i(1 - P_i)\sigma_i v_{th}, \tag{2.54}$$

for the occupation probability P_i and the charge carrier cross section σ_i. In first order the fluence dependence of the trapping centers is linear $N_i \propto \Phi_{eq}$, thus the trapping rate can be written as

$$\frac{1}{\tau_{eff}} = \gamma(t, T)\Phi_{eq}, \tag{2.55}$$

for the damage parameter $\gamma(t, T)$. The different mobility of electrons and holes leads to a diverse impact of radiation on the electron and hole trapping respectively. The degradation of the charge collection efficiency due to charge carrier trapping is given by:

$$Q_{e,h}(t) = Q_{0_{e,h}} \exp\left(-\frac{t}{\tau_{eff_{e,h}}}\right). \tag{2.56}$$

When the average traveling distance $v'_{sat}\tau_{eff}$ for a given saturation velocity v_{sat}, is substantially smaller than the thickness of the silicon bulk, trapping becomes a severe issue for the read-out.

According to [Hartma], the main limiting effects for operating silicon sensors can be roughly estimated based on the level of irradiation Φ_{eq}:

- starting from $10^{14}/\text{cm}^2$, leakage current is the main problem
- at $10^{15}/\text{cm}^2$, the high full depletion voltage might become problematic, too
- at $10^{16}/\text{cm}^2$, the charge collection efficiency drop becomes the fundamental problem

2.2.2 The NIEL Hypothesis

One possibility to normalize different types of radiation lies in the use of the Non Ionizing Energy Loss (NIEL) hypothesis. More details about this approach can be found in [Huhtin].

The displacement damage can be written as:

$$D(E) = \sum_i \sigma_i(E_{kin}) \int_0^{E_{R,max}} f_i(E_{kin}, E_R)P(E_R)dE_R, \tag{2.57}$$

with σ_i being the cross section of the process, f_i being the probability of a collision for particles with energy E_{kin} and a given transferred recoil energy E_R. $P(E_R)$ is

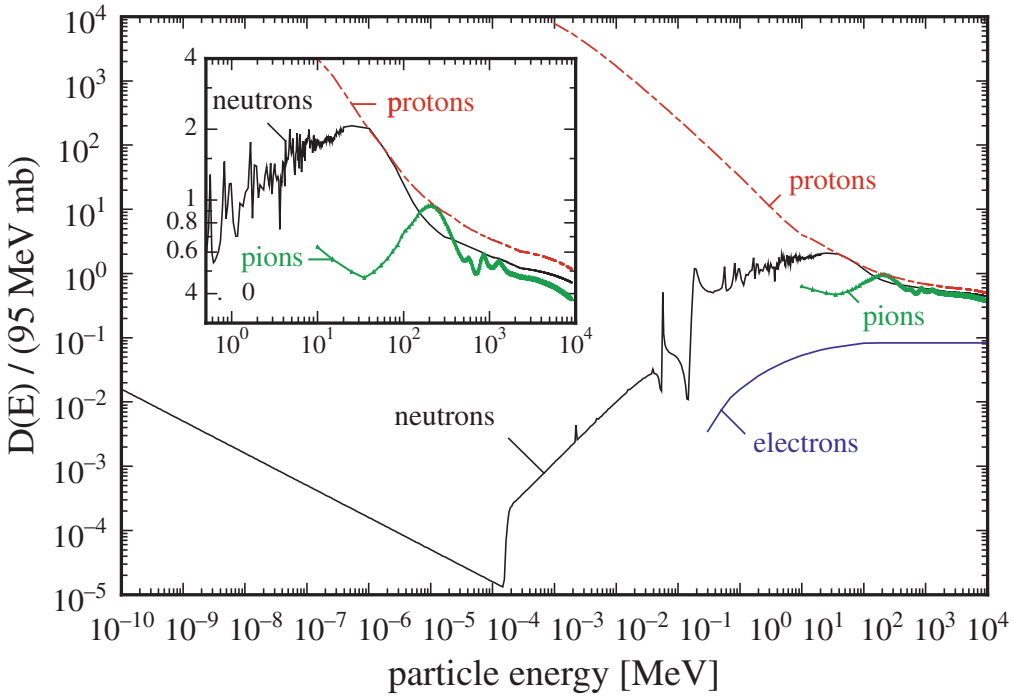

Figure 2.11: Displacement damage function normalized to 95 MeV mb for different particles. The vertical axis corresponds to 1 MeV neutron equivalent damage due to the normalization. The inserted picture shows a zoom into the most important region for sensor devices high energy physics. The figure is taken from [Moll].

the Lindhard partition function specifying the fraction of energy going into the silicon displacement. Details about that can be found in [Lindha]. A common convention is to scale the different radiation sources to the equivalent radiation damage caused by a neutron with 1 MeV kinetic energy.

For these particles the displacement function yields

$$D_{neutron}(1\,\mathrm{MeV})/\mathrm{cm}^2 = 95\,\mathrm{MeVmb}/\mathrm{cm}^2. \tag{2.58}$$

The displacement damage function normalized to 95 MeV mb is shown in figure 2.11.

Using equation 2.58, it is possible to scale radiation of different particles and energies based on their impact on the silicon bulk with respect to radiation damage. The result is the so-called 1MeV neutron equivalent fluence, or Φ_{eq}. The corresponding scaling factor is given by:

$$\kappa = \frac{\int D(E)\phi(E)dE}{95\mathrm{MeVmb}\Phi} = \frac{\Phi_{eq}}{\Phi}, \tag{2.59}$$

with ϕ being the particle fluence.

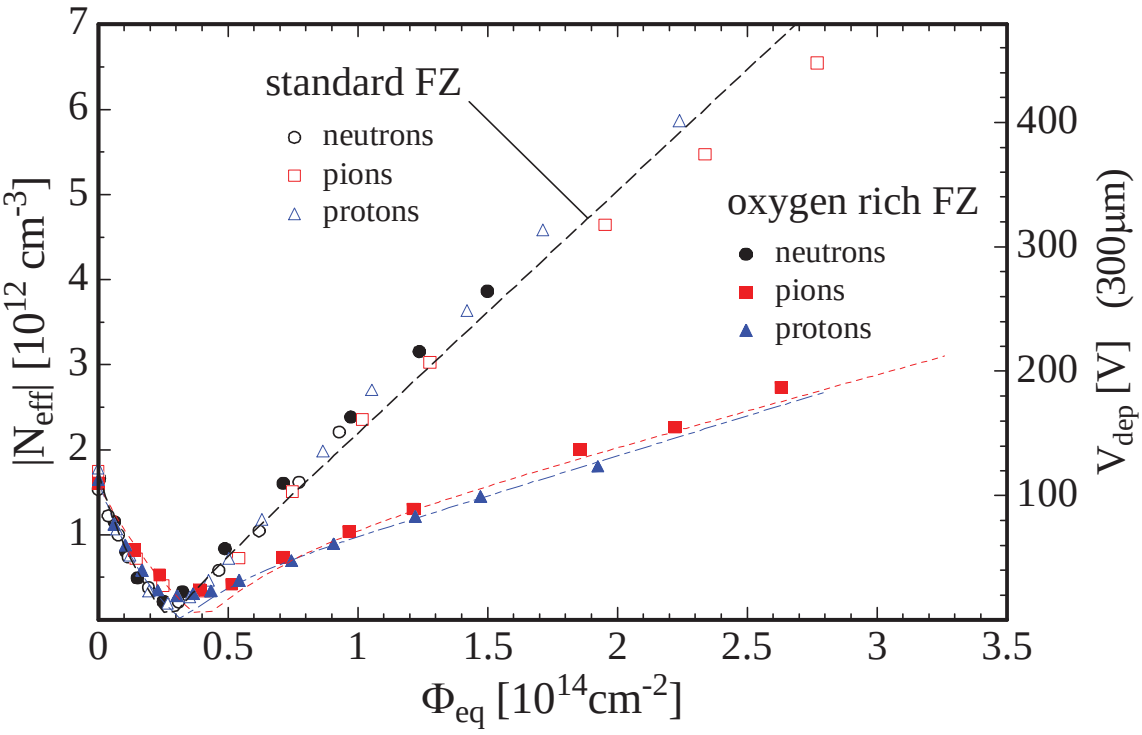

Figure 2.12: Measurement of the evolution of the full depletion voltage for standard FZ (see section 2.3.2) and oxygenated silicon with different types of irradiation scaled to 1 MeV neq according to the NIEL hypothesis. It is clearly visible that for oxygenated silicon charged particles have a reduced impact compared to standard silicon material. The figure is taken from [MollRS].

Violations of the NIEL Scaling

It has been shown experimentally that, in some cases, the NIEL scaling is not valid. One example manifests itself in the evolution of the full depletion voltage of oxygenated silicon. The material has been irradiated by 24 GeV protons, 192 MeV pions and reactor neutrons. The fluence of both radiation types has been scaled with the NIEL hypothesis to 1 MeV neq, so that an identical impact on the effective doping concentration was expected. It turned out, however, that the charged particles have a reduced effect on the modification of the full depletion voltage for oxygenated silicon compared to standard silicon, while the impact of the neutrons does not differ significantly between the two types of sensor material. The measurement is shown in figure 2.12.

It was demonstrated in [Huhtin], that the reason for this deviation lies in the different spatial distribution of the defects within the silicon lattice for different radiation types. In figure 2.13 simulations of the vacancy distribution for protons with 10 MeV and

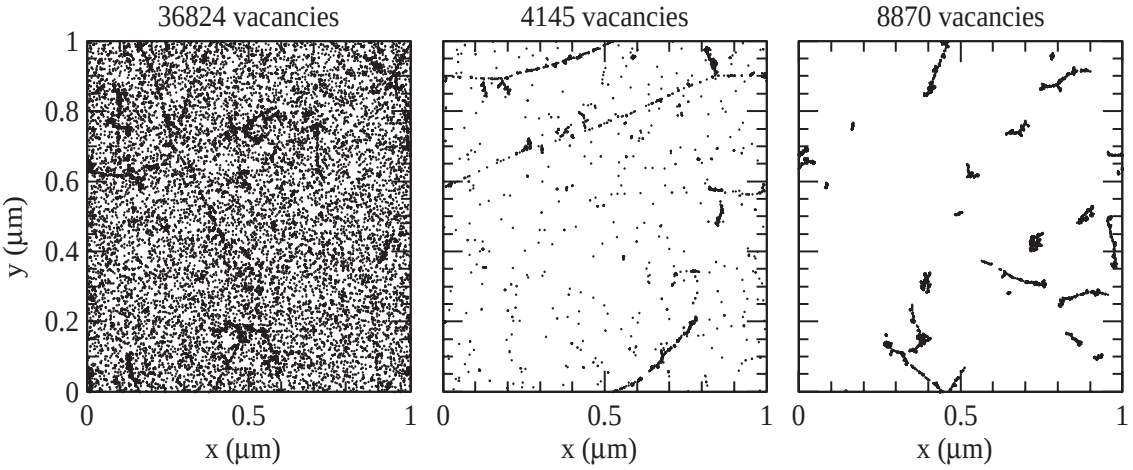

Figure 2.13: Simulation of vacancy distribution immediately after irradiation with: 10 MeV protons (left), 24 GeV protons (middle) and 1 MeV neutrons (right). The fluence corresponds to 10^{14}cm^{-2}. The figures are taken from [Huhtin].

24 GeV and for neutrons with 1 MeV are shown. It is noteworthy that charged particles predominantly create point wise defects, while the neutrons are only building clusters.

It was mentioned before that the displacement energy for point defects and clusters (compare subsection 2.2.1) are different. For the charged particles, a high fraction of their interactions is of Coulomb type with small energy transfers, whereas the neutrons interact via elastic scattering at the nucleus with a essentially higher energy transfer. When the oxygen concentration in the material is high, point-like vacancies tend to form VO defects. If, however, the vacancy concentration is high (e.g. clusters), or if the point wise defects do not have oxygen in their vicinity (low oxygen concentration), the defects can travel within the lattice and build the V_2O complex, which has a high impact on N_{eff}.

The NIEL hypothesis for γ irradiation is also violated, as it was shown in [MoFeFr]. Nevertheless, for standard float-zone material, the NIEL hypothesis is still a good approximation.

2.2.3 Annealing Effects

Even after irradiation wears off, the formed defects migrate, break-up, re-configure or recombine driven by thermal excitation. These processes are called annealing. At temperatures starting from about $150K$, the interstitials and vacancies are mobile in the silicon lattice. There are different actions taking place with different temperature dependencies. According to [Hartma], the main effects, ordered by their time constants from short to long, are:

- Recombination of Frenkel pairs ($I + Si_V \rightarrow Si$)
- Combination of vacancies or interstitials (e.g. $V + V \rightarrow V_2$)
- Combination of complex defects (e.g. $C_i + O_i \rightarrow C_iO_i$).

Annealing of Leakage Current

As already indicated in equation 2.53, the α parameter is dependent on the annealing time and the temperature during annealing. Experimentally, the α parameter can be parametrized as follows [Moll]:

$$\alpha(t,T) = \alpha_0(T) + \alpha_I e^{-\frac{t}{\tau_I(T)}} - \beta \ln \frac{t}{t_0}. \tag{2.60}$$

The parameters were determined to be:

$$\begin{aligned} \alpha_0(T) &= -(8.9 \pm 1.3) \cdot 10^{-17}\text{A/cm} + \frac{1}{T}(4.6 \pm 0.4) \cdot 10^{-14}\text{AK/cm} \\ \alpha_I &= (1.23 \pm 0.06) \cdot 10^{-17}\text{A/cm} \\ \frac{1}{\tau_I(T)} &= k_{0I} \exp\left(-\frac{E_I}{k_B T}\right) \quad with \quad \begin{aligned} k_{0I} &= 1.2^{+5.3}_{-1} \cdot 10^{13} s^{-1} \\ E_I &= (1.11 \pm 0.05) eV \end{aligned} \\ \beta &= (3.07 \pm 0.18) \cdot 10^{-18}\text{A/cm}. \end{aligned} \tag{2.61}$$

In figure 2.14, the linear increase of leakage current with irradiation level is shown on the left plot. The right plot shows the annealing behavior, which is decreasing the amount of leakage current and therefore a desired effect. The deep level defects (see equation 2.35) recombine over time. The reaction rate of this process depends on the respective temperature.

Annealing of the Full Depletion Voltage

The *Hamburg model*, proposed in [Moll], provides a description of the change in full depletion voltage, taking into account both irradiation and annealing. According to it, the effective doping concentration can be described in the following way:

$$\Delta N_{eff}(\Phi_{eq}, t, T) = N_{C,0}(\Phi_{eq}) + N_A(\Phi_{eq}, t, T) + N_Y(\Phi_{eq}, t, T). \tag{2.62}$$

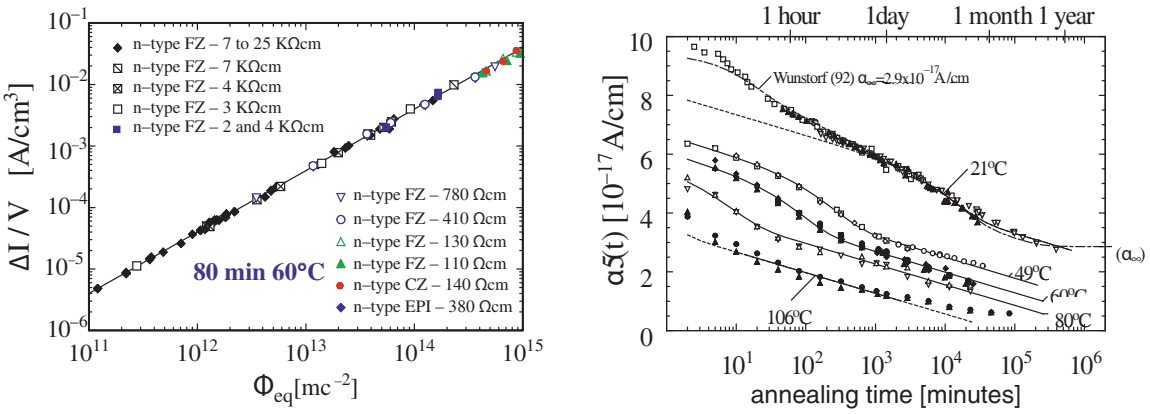

Figure 2.14: The linear leakage current increase with rising irradiation level is shown on the plot on the left-hand side with double logarithmic scale. The linearity factor α is stable even for different n-type materials. The right-hand side plot shows the annealing effect of the leakage current over time (logarithmically) for different annealing temperatures. The plot is taken from [Moll].

The Stable Damage Term $N_{C,0}$

$N_{C,0}$ is the dominant term for high radiation environments like the CMS detector and is called stable damage term. It describes the effects of donor removal and the creation of acceptor defects on the free charge carrier concentration (see subsection 2.2.1).

$$N_C(\Phi_{eq}) = N_{C,0}(1 - e^{-c\Phi_{eq}}) + g_c\Phi_{eq} \tag{2.63}$$

c is the donor removal constant and g_c is the damage parameter for the creation of acceptor like defects, $N_{C,0}$ is the asymptotic value of the donor removal term assuming that the donor removal is incomplete with a finite final value. The latter can be expressed with the removal factor r_c and the initial effective doping concentration resulting in:

$$N_{C,0} = r_c \cdot |N_{eff,0}|. \tag{2.64}$$

The Beneficial Annealing Term N_A

Immediately after the irradiation wears off, a process occurs that increases the positive space charge. A compensation of positive and negative space charge leads to smaller final full depletion voltage values, as the space charge is negative after the type inversion. Since low final full depletion voltage values are desirable for operation, this effect is called *beneficial annealing*. It can be written as:

$$N_A(\Phi_{eq}, t, T) = \Phi_{eq} \sum_i g_{a,i} \exp\left(-\frac{t}{\tau_{a,i}(T)}\right) \approx \Phi_{eq} g_a \exp\left(-\frac{t}{\tau_a(T)}\right), \tag{2.65}$$

for damage parameters $g_{a,i}$ and time constants $\tau_{a,i}(T)$. For particle detectors it is usually not relevant to quantify the changes on the minute or hour level, thus the parameters can be approximated by the longest decay time constant ($g_{a,i} \to g_a, \tau_{a,i}(T) \to \tau_a$).

Due to the short time constant of these processes, this effect is also called *short term annealing*.

The Reverse Annealing Term N_Y

Reverse annealing leads to a decrease in space charge and thus to an increase in the final depletion voltage value after type inversion. Since the time constant for these processes is larger than for the short term annealing, it is also called *long term annealing*. It can be parametrized by:

$$N_Y(\Phi_{eq}, t, T) = g_Y \Phi_{eq} \left(1 - \frac{1}{1 + t/\tau_Y(T)}\right), \tag{2.66}$$

with the respective damage parameter g_Y and time constant $\tau_Y(T)$. The parameters of this model are not independent of the material under investigation. A more detailed discussion will be presented in chapter 6.

A graphical representation of the different full depletion effects is shown in figure 2.15. An overview of the time constants for beneficial and reverse annealing is summarized for different temperatures in table 2.2.

Annealing temperature [°C]	-10	0	10	20	40	60	80
Beneficial annealing τ_a	306d	53d	10d	55h	4h	19min	2min
Reverse annealing τ_Y	516 y	61y	8y	475d	17d	21h	92min

Table 2.2: List of annealing time constants for beneficial and reverse annealing [Moll]. Silicon detector collaborations aim to maximize the beneficial annealing while still avoiding as much reverse annealing as possible.

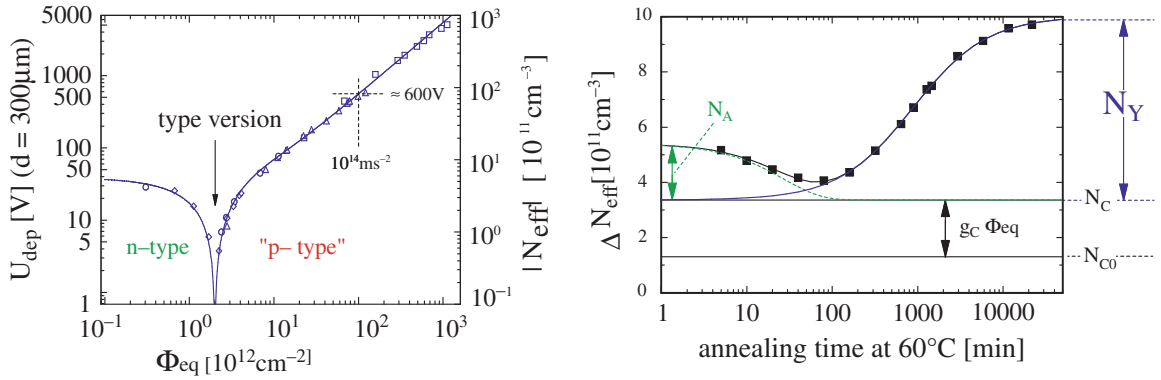

Figure 2.15: The change of full depletion voltage with irradiation is shown in the plot to the left. During irradiation, the full depletion voltage decreases until the n-type bulk becomes a p-type bulk (type inversion). Afterwards it increases. In the plot on the right-hand side, the different annealing terms are schematically drawn. The short term annealing acts first, followed by the long term annealing. The two effects have opposite impacts [Moll].

2.2.4 Surface Damage of Silicon Sensors

The surface of modern silicon microstrip sensors is usually formed by highly doped silicon strips, a silicon oxide (SiO_2) insulation layer with metal strips on top. This metal-oxide semiconductor forms a *MOS* structure whose properties are discussed in more detail, for example, in [Lutz]. The main damage process is ionization.

The mobility of electrons is several orders of magnitude higher than the mobility of holes, therefore, positive holes accumulate in the SiO layer. The flat-band condition describes the situation in which bands are flat over the MOS structure. The flatband voltage is the voltage that needs to be applied to create this configuration. Usually, the MOS part of the sensors are not biased with a potential. Additional holes in the oxide layer change the flatband voltage in the following way:

$$\Delta V_{flatband} = -\frac{1}{\epsilon_{ox}\epsilon_0}\left(\sigma_{int} d_{ox} + \int_0^{d_{ox}} \rho(x) x dx\right). \tag{2.67}$$

for the respective epsilon values, the density of introduced additional charge $\rho(x)$, the surface charge at the $Si - SiO_2$ interface σ_{int} and the oxide thickness d_{ox}.

This relationship can be utilized to determine the amount of radiation a sensor has been exposed to by measuring the flatband voltage. Due to the accumulation of positive charge within the oxide layer electrons are attracted from the bulk towards the strips. These electrons decrease the inter-strip resistance and increase the polarisability and inter-strip capacitance. The latter effect leads to an increase in noise for sensors with n-type strips.

2.3 Growth Techniques for Silicon Sensors

This section introduces some well established methods to turn pure sand or quartzite (SiO_2) into mono crystalline silicon, which can then be used for the construction of particle tracking devices later on. In addition to a high minority charge carrier lifetime, a high resistivity (above 1 kΩcm) is one design goal for silicon sensor material, since a high resistivity corresponds to low full depletion voltage values (see equation 2.14 and 2.29). High generation lifetimes are desirable (see equation 2.35) to reduce the leakage current and thus unnecessary power load as well as noise.

2.3.1 Obtaining Pure Silicon

The first step to obtain pure silicon is performed in a furnace with various forms of carbon, melting the pure sand or quartzite at around 1780 °C. Even though many reactions take place, the predominant reaction is:

$$SiO_2 + 2C \rightarrow Si + 2CO. \tag{2.68}$$

Silicon obtained through this procedure is called *metallurgical grade silicon*, and commonly has a purity of about 98%.

In a second step, the silicon is pulverized and treated with hydrogen chloride at about 300 °C. In this way, trichlorosilane is formed, which is liquid at room temperature

$$Si + 3HCl \rightarrow SiHCl_3 + H_2. \tag{2.69}$$

The trichlorosilane has a low boiling point of 32 °C, thus it can be repeatedly distilled to remove unwanted impurities. When the purity is at its desired level the trichlorosilane is put into a hydrogen reduction reaction, where a heated silicon rod acts as the nucleation point,

$$SiHCl_3 + H_2 \rightarrow Si + 3HCl. \tag{2.70}$$

After this procedure, the highly pure silicon has become so-called *electronic-grade* silicon.

2.3.2 Float-Zone Silicon

Float-zone silicon (FZ) is the material used at the CMS silicon particle detectors. The float-zone method is capable of producing single crystal silicon of high purity.

A simplified schematic of the process is depicted in figure 2.16. Vertically aligned within a quartz envelope a highly pure polycrystalline silicon rod is rotated with a seed crystal at the bottom. Starting from the seed, a radio-frequency heater is slowly guided along the whole rod, melting a small band of the rod at a time. When the heater moves upwards, a single crystal freezes at the lower end of the *floating zone*. The environment is filled with an inert atmosphere of argon.

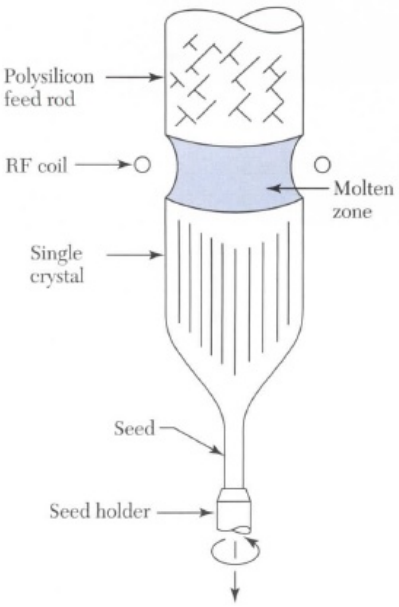

Figure 2.16: Schematic of a float-zone production process of single crystal silicon, taken from [Sze].

2.3.3 Research and Design of New Silicon Sensor Materials

It is a major effort of scientists all over the world, to investigate new approaches which could lead to the improvement of silicon properties for sensor material. An overview of results of the RD50 collaboration, which is specialized on the research of radiation hard semiconductor devices, can be found in [RD50].

Other important materials that are topic of investigation besides FZ silicon are mainly:

- Oxygen enriched float zone silicon (DOFZ)
- Magnetic Czochralski silicon (MCz)
- Epitaxial Silicon (Epi)

For DOFZ the oxygen concentration is enhanced by diffusing oxygen from a SiO2 layer coating the wafer at high-temperatures. The Czochralski process, named after its inventor J. Czochralski [Czochr], is an alternative technique to grow single crytal silicon. He determined the crystallization velocity of metals by pulling out crystals out of a melt. It is an alternative technique to grow single crystal silicon.

A silicon single crystal (seed) is pulled out, while rotating, of a silicon melt. The process takes place in an inert atmosphere of argon and is called Czochralski technique. If an additional a strong magnetic field is applied to control the convection of the silicon and to slow the migration of impurities into the crystal, this type of silicon is referred to as MCz silicon. The magnetic field leads to silicon with less impurities, also the impurities are distributed more homogeneously.

Another important material is the so-called *epitaxial silicon* (Epi). There are several different types of and techniques for producing epitaxial silicon (for details see [Dezill]). All these techniques share the fact that a silicon layer is built upon a substrate wafer.

A common approach is the vapor-phase epitaxy, which uses a compound-like silicon tetrachloride ($SiCl_4$) in gas form to condensate on the substrate. The reaction takes place at around 1200 ° C and can be simplified as:

$$SiCl_4 + 2H_2 \rightarrow Si + 4HCl. \tag{2.71}$$

The benefit of this method is that the impurity concentration can be adjusted in a controlled way in the gaseous phase, leading to a well known and homogeneous impurity concentration of the sensor bulk. For large-scale particle detectors the material is not suitable yet since the removal of the non-active substrate layer is difficult and expensive. For scientific research however, this material is commonly used.

Chapter 3

The Large Hadron Collider Experiments

The *European Organization for Nuclear Research* (CERN, formerly known as *Conseil Européen pour la Recherche Nucléaire*) is situated near Geneva astride the Franco-Swiss border. It was founded in 1954 as an international organization for fundamental particle physics research. Among CERN's most significant achievements in the field of particle physics are the discovery of the Z and W bosons in 1983 [Rubbia] and most recently the discovery of the Higgs boson [CMSHIG]. Besides the fundamental research the technologies developed at CERN have influenced today's life in many ways. The most prominent example is the world wide web, which has been invented at CERN [WWW] in 1990.

The major facility hosted by CERN is the *Large Hadron Collider* (LHC), the most powerful particle accelerator ever built. Its main scientific purpose is the collision of protons with protons with all-time high energies. The design center-of-mass energy is $\sqrt{s}$ =14 TeV, whereas the LHC is currently running at a center-of-mass energy of 8 TeV during 2012 operations. Although they cannot be discussed in further detail, the LHC is providing lead-lead collisions several weeks per year, which already resulted in unexpected observations e.g. *jet quenching* found by the two major collaborations ATLAS [DijetA] and CMS [Quench].

There are seven experiments connected to the large hadron collider. These are CMS [CMS] (*Compact Muon Solenoid*) and ATLAS [ATLAS] (*A Torodial LHC ApparatuS*) with their two big general purpose particle detectors. The ALICE (*A Large Ion Collider Experiment*) [ALICE] main field of research is the investigation of quark-gluon plasmas created during the heavy ion collisions at the LHC. LHCb (*Large Hadron Collider beauty*) [LHCb] is putting focus on B meson physics, especially on the measurement of CP-asymmetries. TOTEM's (*TOTal Elastic and diffractive cross section Measurement*) [TOTEM] main purpose is the measurement of luminosity and p-p cross sections as well as a precision measurement of the proton size. LHCf (*Large Hadron Collider forward*) [LHCf] uses particle cascades created at the LHC in order to gain insights on cascades produced from cosmic rays. The MoEDAL (*Monopole & Exotics*

Detector at the LHC) experiment's [MoEDAL] main task is the search for magnetic monopoles. An overview of the main experiments is depicted in figure 3.1.

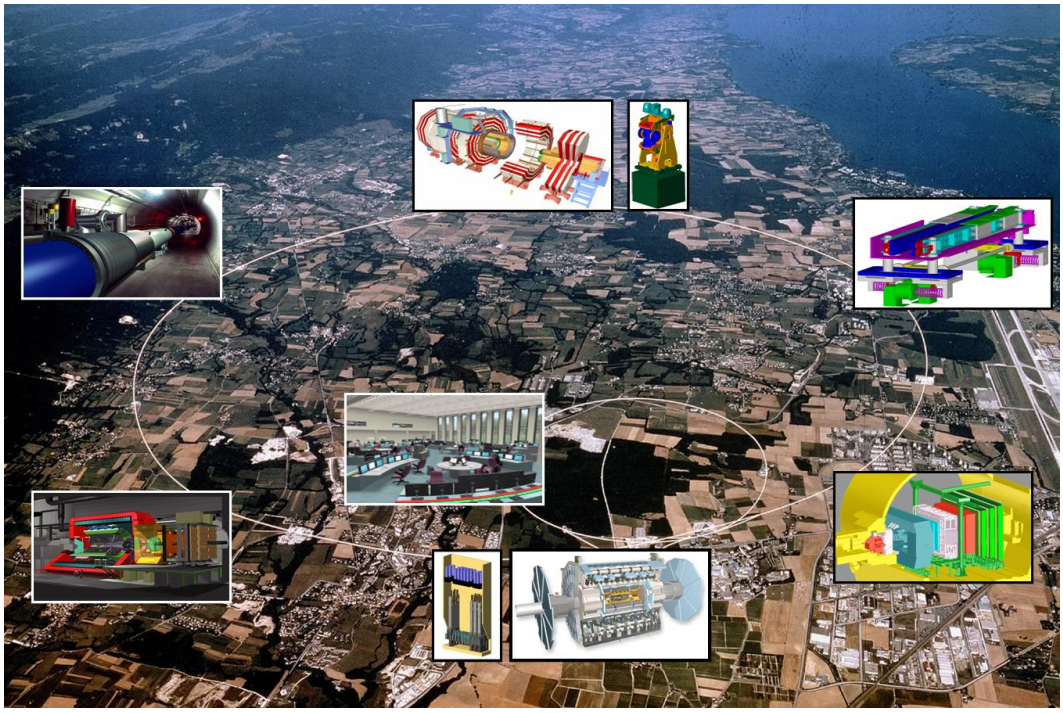

Figure 3.1: Geographical sight on the LHC site taken from [LHCEXP]. The course of the LHC tunnel and the SPS is indicated with the white circles. The inserted figures around the LHC ring are clockwise, starting from the the top: CMS, Beam Dump System, LHCb, ATLAS, ALICE, the RF system. In the center, a schematic of the LHC control room (CCC) is shown.

3.1 The Accelerator Complex

3.1.1 Introduction to the LHC Accelerator Complex

The LHC itself is only the final cycle in a chain of different accelerators. A schematic overview of the accelerator facilities at CERN is displayed in figure 3.2. Unfortunately, further discussion of all the accelerators in detail is out of the scope of this thesis; a comprehensive description can be found in [EvaBry].

The first step of the accelerator chain is the *duoplasmatron*. In this device electrons are emitted into a vacuum chamber. Then hydrogen gas is introduced into the chamber. The free electrons interact with the gas and ionize the hydrogen atoms. The protons obtained this way are fed into the *Radio Frequency Quadrupole* (RFQ). The ions leave this short accelerator of 1.75 m with an energy of 750 keV. Afterwards, the protons

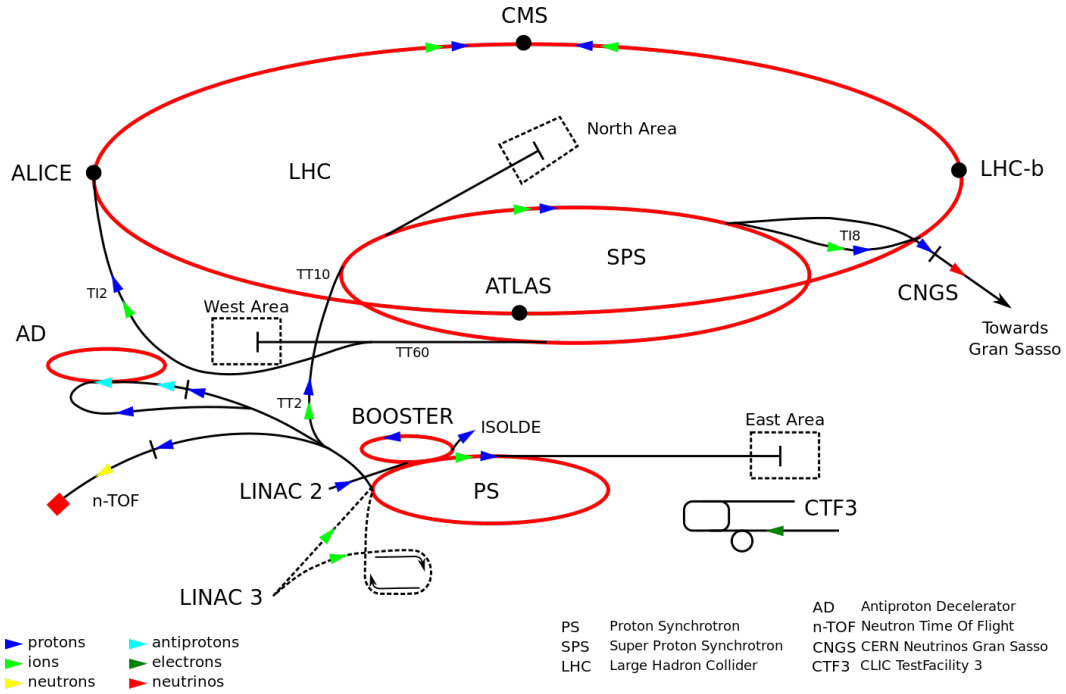

Figure 3.2: Overview of the different accelerator facilities at CERN, taken from [Lefevr]. The protons are successively accelerated in several pre-accelerators. The first step of this sequence is the linear accelerator Linac2, followed by three circular accelerators: the Booster, the Proton Synchrotron (PS) and the Super Proton Synchrotron (SPS). In the Large Hadron Collider (LHC) itself the protons are accelerated further to the final center-of-mass energy of 4 TeV per beam during 2012 operations.

are further pushed to 50 MeV in the electromagnetic cavities of the *Linear Accelerator* (Linac2) within a length of 30 m. The next step is the first circular accelerator, the *Proton Synchrotron Booster* (PSB) with a diameter of 50 m and a final energy of 1.4 GeV. The *Proton Synchrotron* (PS) increases the kinetic energy of the ions to 25 GeV and has 628 m of circumference. The last pre-accelerator is the *Super Proton Synchrotron* (SPS). It has a circumference of 6912 m and can achieve beam energies up to 450 GeV. It has 744 bending dipole magnets and 216 focusing quadrupole magnets. Besides it's role in the LHC pre-accelerator chain, it is also used for fixed target experiments like COMPASS [COMPAS] and NA61 [NA61]. Moreover the neutron streams for the CNGS experiment [CNGS] are produced in the SPS. Finally, the protons are injected into the LHC main ring. An overview of the size and energy of each accelerator contributing to this complex is shown in table 3.1.

Accelerator	Type	Length/Circumference	Maximum Energy
RFQ	linear	1.75 m	750 keV
Linac2	linear	30 m	50 MeV
PSB	circular	157 m	1.4 GeV
PS	circular	628 m	25 GeV
SPS	circular	6912 m	450 GeV
LHC	circular	26.7 km	3.5 - 7 TeV

Table 3.1: List of the accelerator chain for proton-proton collisions at the LHC.

The LHC has been built in the tunnel of the former *Large Positron Electron Collider* (LEP). It is approximately 100 m below the surface with a total of more than 26 km circumference. It is designed to ramp up both proton beam energies to 7 TeV each, using superconducting high frequency cavities. The proton beams are guided in two separate beam pipes in opposite directions. 1323 superconducting dipole magnets are utilized to constrain the beams to circular orbits.

Due to space constraints in the tunnel the magnets' structure is shared between both beam pipes. The bending magnetic field strength reaches up to 8.33 T. In order to keep the magnets superconducting, they are cooled with superfluid helium to an operational temperature below 2 K (-271.15 ° C) by a complex cryogenic system. 7000 normal and superconducting additional magnets are employed to focus the beams.

The fatal consequence of a cooling failure was impressively demonstrated in 2008 a conductor between two LHC magnets lost its superconductivity [Rossi]. The heat generated due to the new resistance led to an explosion of 6 tons of superfluid helium. During this accident, 37 magnets have been heavily damaged, so that they needed to be replaced. Including the long warm up and cool down periods, the costly repair and recommissioning of the LHC took more than a year. This experience contributed to the decision to run the LHC below the design energy of 7 TeV per beam. It is planned,

however, to perform various upgrades during the long shutdown of 2013 and 2014 to safely reach the designed beam energy afterwards.

There are four interaction points (IPs) where the two beams can be brought to collision and around which the four major experiments are built: CMS, ATLAS, LHCb and ALICE.

3.1.2 LHC Operation

The beam energy is an important parameter, since it has a high influence on the production cross section of processes (compare figure 1.3). The final goal of a particle accelerator is to generate as many events of interest as possible. In order to achieve this, another quantity is crucial: the *instantaneous luminosity* L.

According to [EvaBry], the number of events generated per time with a cross section of σ_{prod} is given by

$$\dot{N} \equiv \frac{\partial N}{\partial t} = L \cdot \sigma_{prod}. \tag{3.1}$$

The instantaneous luminosity is defined by various beam parameters:

$$L = \frac{N_1 N_2 f \gamma}{4\pi\epsilon\beta^*} F, \tag{3.2}$$

with N_1 and N_2 being the number of particles in each beam, f is the frequency of the beam revolution, γ the relativistic gamma factor.

The *emittance* ϵ is a measure of the average spread of the particles in the position-momentum phase space. The *beta function* β describes the oscillation envelope of the beam, while β^* is the value of the beta function at the interaction point. Further details about the emittance and the beta function can be found in [Lee]. The geometric luminosity reduction factor F is defined by:

$$F = \left(1 + \left(\frac{\theta_c \sigma_z}{2\sigma^*}\right)^2\right)^{-1/2}, \tag{3.3}$$

with the crossing angle of the beams θ_c, the standard deviation of the bunch length in beam direction σ_z and the standard deviation of the bunch width in transverse direction σ^*. For this formula, the beam characteristics are assumed to be identical for each beam and the beam bunches are considered Gaussian distributed. In addition, $\sigma_z \ll \beta^*$ is used.

The LHC is operated 24/7, whereas not all the time colliding beams are present in the machine. About 30 weeks per year are dedicated to data taking (for details see [LHCSCH]), whereas the rest is used for maintenance and optimization. The collision time is structured in so-called fills which can last from a couple of hours to a whole day. For each fill the proton bunches are injected into the LHC and then ramped up

to their final energy. The instantaneous luminosity is slowly decreasing during the fill due to side effects e.g. beam-beam interactions.

Over longer time intervals, the *integrated luminosity* $\mathcal{L}$ gives an estimate of the overall performance of the collider. The amount of events generated is defined by:

$$N = \int L dt \sigma_{prod} = \mathcal{L}\sigma_{prod}. \tag{3.4}$$

The beam parameters differ from fill to fill. An example set of beam characteristics for a standard 2012 proton-proton fill is listed in table 3.2, together with the original design values.

Parameter	2012 Standard Fill	Design Value	Unit
Proton Energy	4	7	TeV
Number of Bunches	1380	2808	-
Bunch Spacing	50	25	ns
Number of Protons per Bunch	$1.5 \cdot 10^{11}$	$1.5 \cdot 10^{11}$	-
Normalized Transverse Emittance ϵ	2.79	3.75	μm rad
Beta Function at the IP β^*	1.5	0.55	m
Instantaneous Luminosity	$6.49 \cdot 10^{33}$	$10 \cdot 10^{33}$	$\mathrm{cm}^{-2}\mathrm{s}^{-1}$

Table 3.2: Comparison of typical parameters of a standard filling schema of 2012 p-p collisions at the LHC and their respective design values.

3.2 The Compact Muon Solenoid Detector

The events generated at the IPs of the LHC are measured and recorded in the particle detectors of their respective experiments. The CMS detector is with 14000 tons the heaviest of the LHC detectors and is situated at the LHC access point 5. The basic features are summarized in table 3.3, the layout of the detector is shown in figure 3.4. Further details about the various sub-detectors is presented in the following subsections.

Feature	Value
Total Weight	14000 T
Overall Diameter	15m
Overall Length	21.5 m
Magnetic Field Strength	3.8 T

Table 3.3: Summary of basic CMS features.

An important quantity, which is commonly used to describe the solid angle coverage of the various detectors, is the *pseudorapidity*:

$$\eta \equiv -\ln(\tan(\theta/2)), \tag{3.5}$$

for the polar angle θ in beam direction. Since the proton beams are not polarized the particle decays are expected to be rotationally symmetric. Thus, cylindrical coordinates are commonly used (r,ϕ). A draft of the coordinate convention is shown in figure 3.3.

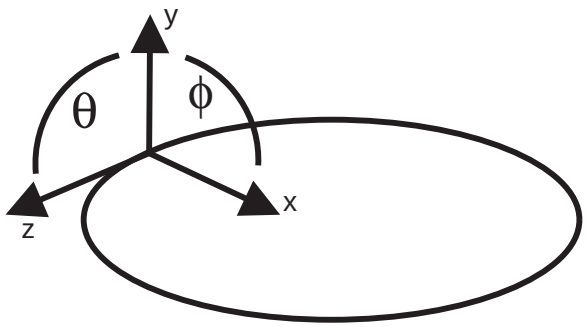

Figure 3.3: Schematic illustration of the coordinate convention used at the LHC experiments.

The pseudorapidity is an approximation of the *rapidity* for high energetic particles which is defined as:

$$Y \equiv \frac{1}{2}\ln\left(\frac{E + p\cos(\theta)}{E - p\cos(\theta)}\right) \tag{3.6}$$

with the energy E and momentum p of the particle. For massless particles the rapidity and pseudorapidity is equivalent.

3.2.1 The Tracker

The tracker consists of two major detectors: the *pixel detector* and the *silicon strip tracker*. A schematic cross section of the tracker is depicted in figure 3.5.

The Pixel Detector

The pixel detector is a silicon detector with high granularity. It is covering an area of more than 1 m^3, with a cell size of 100 μm $\times$150 μm. It is distributed in three layers parallel to the beam pipe (the barrel region with $\approx$ 48 million pixels) and two disks at each side perpendicular to it (the end cap region with $\approx$ 18 million pixels). The closest distance to the beam pipe is 4.3 cm, leading to a primary vertex resolution below 50 μm [KotSta]. The pixel detector is built out of oxygenated n-in-n silicon

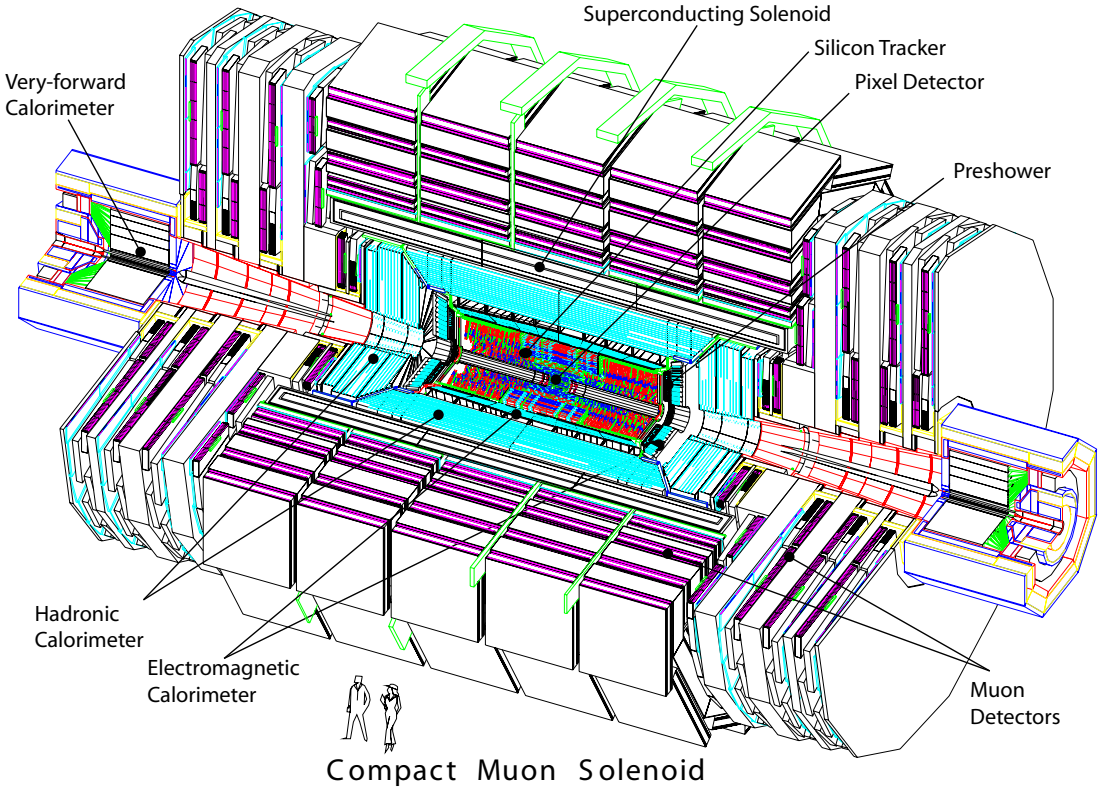

Figure 3.4: Layout of the CMS multipurpose detector from [CMSLAY]. For further details about the different parts of the CMS detector see the following subsections.

material, designed to endure in this high radiation region during the coming years of nominal LHC luminosity.

Silicon Tracker

The silicon microstrip tracker is the largest silicon detector in the world. It has a surface of more than 200 m^2 with a total of 24328 sensors. The 9.3 million read-out channels are wire bonded to 75000 read-out chips (APV25 with 128 channels [FrJoMo]).

It has four different partitions (compare figure 3.5):

TIB The Tracker Inner Barrel

TID The Tracker Inner Disk (plus and minus side along z)

TOB The Tracker Outer Barrel

TEC The Tracker End Cap (plus and minus side along z)

In total, there are more than 20 different module designs. A single module consists of one or two sensors, the read-out electronics and a support frame. The latter is made

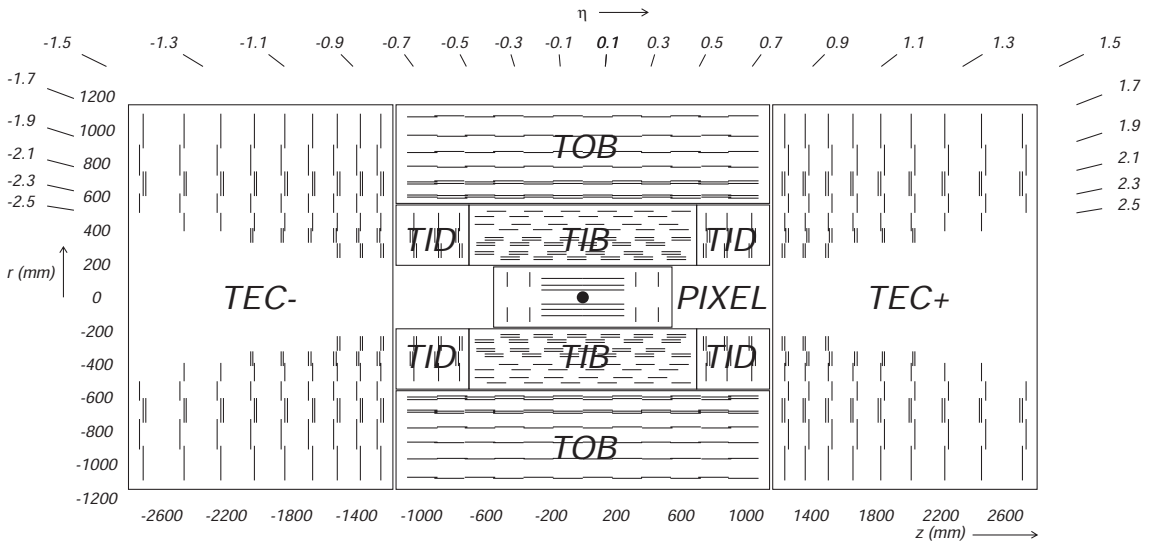

Figure 3.5: Draft of a cross section through the CMS tracker. The black dot in the middle indicates the interaction point. The acronyms are specified in the text (see subsection 3.2.1). The total tracking coverage lies within a pseudorapidity of $|\eta| < 2.5$. The double lines indicate back-to-back modules delivering stereo hits [CMSCOL].

of carbon fiber with a high stiffness and good thermal conductivity.

The read-out electronics integrate four to six APV25s in a *hybrid*. Each two APV25s share one optical fiber output. In some layers two modules are mounted back to back (see figure 3.5). One sensor is tilted against the other in an angle of 100 mRad in order to improve the spatial resolution in strip direction.

In the TIB partition the modules have one sensor with a thickness of 320 μm and a strip length up to 12 cm. In the TOB two sensors are bonded together on each module to reach a total strip length of up to 19 cm. Since the noise increases with the strip length, the thickness of the TOB modules (500 μm) has to be higher to achieve a signal over noise ratio equal to the TIB. Additionally, in the TID partition 320 μm sensors are used, while in the TEC partition both 320 μm and 500 μm thick sensors are employed. The majority of sensors are built by Hamamatsu Photonics K.K. (HPK), while about 4% of the sensors are produced by ST Microelectronics.

All sensors are AC coupled and use single-sided p^+-implant strips in n-bulk material. There are two reasons why oxygenated silicon is not used for the sensors even though this would have a beneficial effect on the radiation hardness (compare section 2.2.2). First, the production of oxygenated silicon was not a standardardized process and no guarantee would have been given for the quality of the material. And secondly, for neutrons the radiation damage is the same in oxygenated silicon and standard silicon. Depending on the position within the strip tracker, neutrons form 20-50% of the radiative flux.

The crystal orientation of the modules has been chosen to be $\langle 100 \rangle$ since $\langle 111 \rangle$ orientation shows more surface damage after irradiation according to [Braiba].

The resistivity varies from approximately 1.5 kΩcm to 3 kΩcm for the thin sensors. For the thick sensors the resistivity lies between 3.5 kΩcm and 7.5 kΩcm. These values are directly connected to initial values of the full depletion voltage between 100 V and 300 V. The sensors are aligned in a way that regions with higher irradiation levels (especially the first layer in TIB) have higher initial full depletion voltages. During the expected 10 years of irradiation by the LHC the p-in-n sensors will undergo type inversion (see subsection 2.2.3), this implies that higher initial full depletion voltage values result in lower final full depletion voltage values. The aim is that the final full depletion voltage is still low enough to operate the sensors with high efficiency. The present bias voltage is 300 V for the vast majority of modules.

The cooling pipes are integrated in the support structures of the subsystems, which are petals for the end caps and rods for the outer barrel region (see figure 3.6).

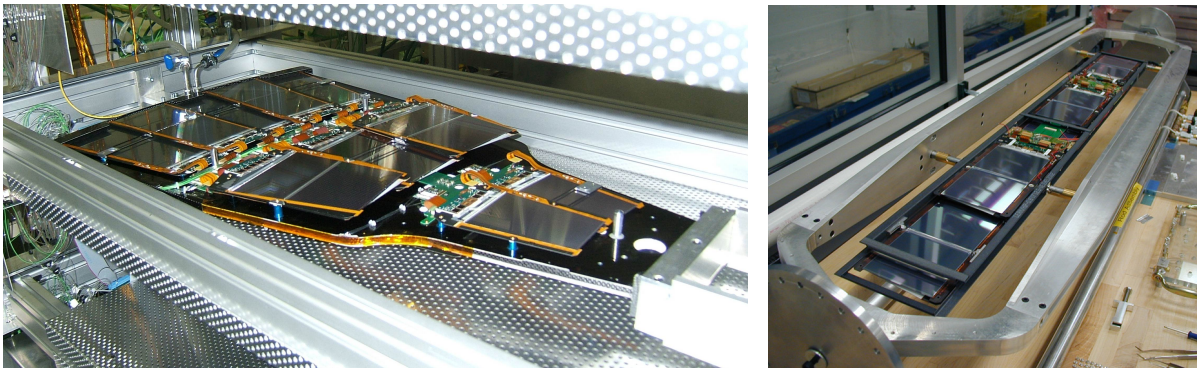

(a) Petal (b) Rod

Figure 3.6: Photos of CMS tracker support structures. The modules are assembled on petals in the end cap region (a) and on rods in the barrel region (b) [CMSPho, Fermil].

The hit efficiency of a silicon microstrip layer is one of the fundamental factors for a good tracking performance. It is defined as the ratio with which a signal hit is found at the position where the traversing particleÂ´s trajectory, calculated by the remaining layers, crosses the layer of investigation. In figure 3.7 the 2011 results of the hit efficiency for the tracker layers computed by the *detector performance group* (DPG) is shown [DPG].

Further details on the excellent physics performance of the silicon microstrip tracker of CMS fcan be found in [TraPer].

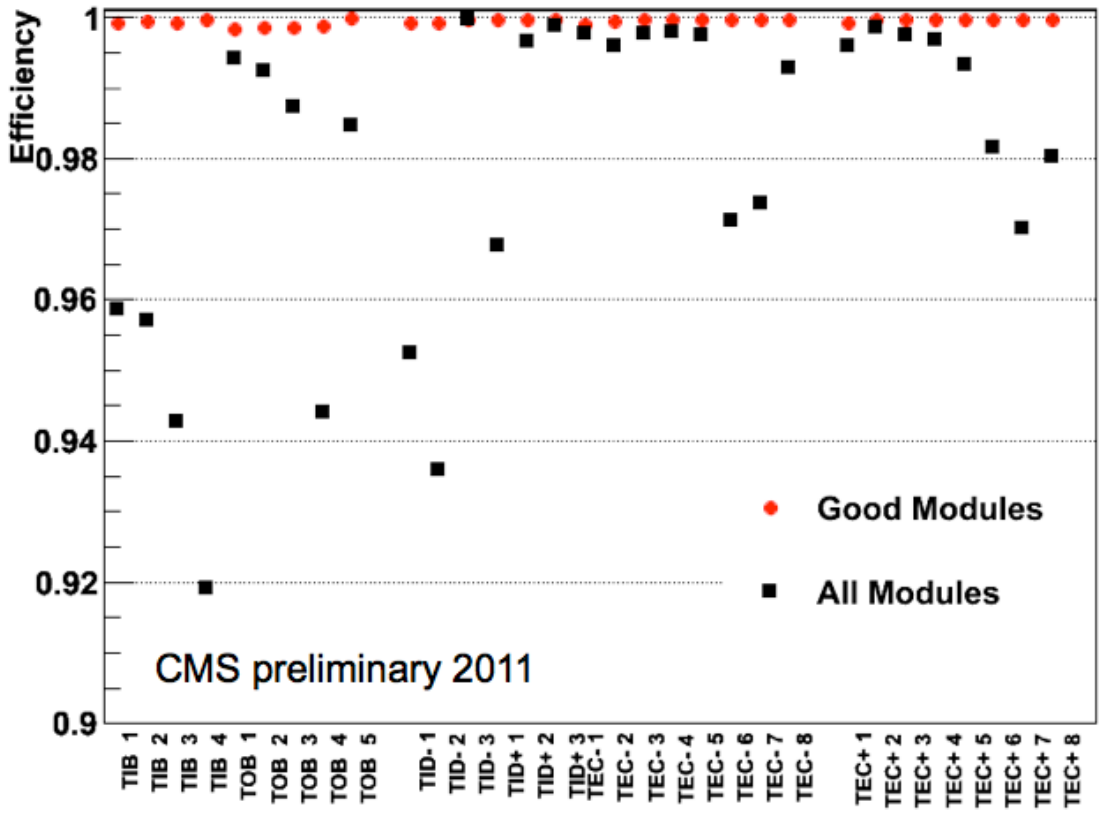

Figure 3.7: Hit efficiency of the tracker layers during 2011 operations. The red dots represent the hit efficiency only for modules considered as good, while the black dots indicate the hit efficiency values for all modules. The figure is taken from [DPG].

3.2.2 The Calorimeters

Preshower Detector

The preshower detector is situated between the silicon tracker and the electromagnetic calorimeter. It consists of two layers of lead radiators with about 2 and 1 radiation length thickness respectively, each followed by a silicon microstrip detector. Photons traversing the lead generate a particle shower due to bremsstrahlung and electron-positron pair production. The products of these cascades are detected in the adjacent silicon layers with high accuracy. The purpose of this approach is to improve the spatial resolution for photons. The resolution of the electromagnetic calorimeter is lower than the resolution of the silicon detectors. For most particles, spatial information from the tracker is combined with the data from the calorimeter (see subsection 3.2.5). Since photons do not create a trace in the silicon strip detector this special structure is needed.

Electromagnetic Calorimeter (ECAL)

The ECAL is built of lead tungstate ($PbWO_4$) crystals (61200 in the barrel region and 14648 is the end caps). The crystal is easy to grow, dense (8.28 g/cm^3) and optically clear. It has a radiation length of $X_0 = 0.89$ cm and a Molière radius of 2.2 cm. The scintillating light generated by traversing, electromagnetic interacting particles (mainly photons and electrons) is detected by silicon avalanche photo diodes in the barrel region ($|\eta| < 1.48$) and vacuum photo triodes in the endcap region ($1.48 < |\eta| < 3$). The crystals are radiation hard and have a scintillation decay time with 80% of light yield within the nominal crossing time of 25 ns.

Hadronic Calorimeter (HCAL)

The HCAL consists of brass layers interleaved with plastic scintillators. To maximize the share of material inside the magnetic field, the read-out is performed in hybrid photo diodes connected via wavelength shifting optical fibers. A photo cathode inside the photo diode is followed by several millimeter gap, with a strong electric field applied. The accelerated electrons are detected by a silicon diode target.

Very Forward Calorimeter

The *Hadronic Forward* (HF) is located on both sides of the detector in high eta region. It consists of steel absorbers and quartz fibers, both very radiation tolerant materials. Since the magnetic flux is relatively low in this region the read-out is performed with standard photomultipliers.

3.2.3 Muon Detectors

There are three different sub detectors contributing to the muon measurement. The *Drift Tubes* (DT) are situated in the barrel region, the *Cathode Strip Chambers* (CSC) are in the end cap region and the *Resistive Plate Chambers* (RPC) is a dedicated trigger detector covering both regions. All muon detectors are embedded in the return yoke of the magnet. The muon momentum resolution is 1% - 6%, depending on the pseudorapidity [PerMuo].

3.2.4 The Magnet

The superconducting solenoid of CMS is with a length of 13 m and a diameter of 5.9 m, the largest of its kind. It provides a magnetic field strength of 3.8 T. The operating current is more than 18 kA, resulting in a stored energy of 2.3 GJ.

3.2.5 Particle Identification at CMS

Most physics analyses of CMS are using particle flow event reconstruction. In this approach, information from all relevant sub detectors are combined to individually reconstruct each stable particle in the event. The high magnetic field strength in combination with the excellent performance of the large silicon tracker contribute to the enormous success of this method. Further details about particle flow can be found in [PFlow] and [BeaBen]. Figure 3.8 shows a schematic of different particles and their interactions with the CMS sub detectors.

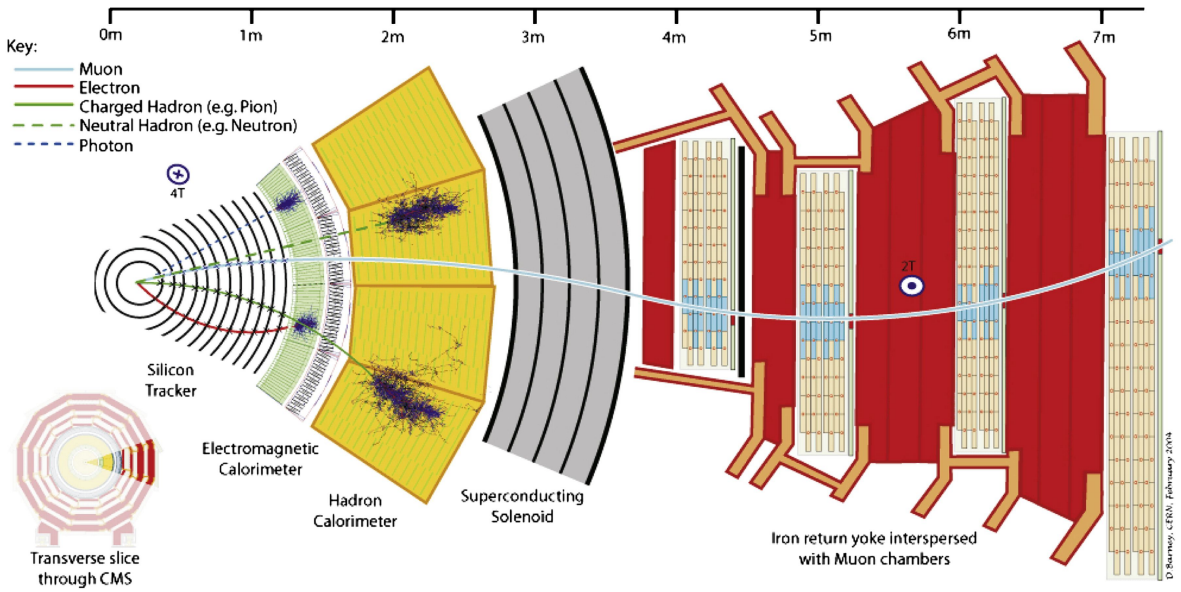

Figure 3.8: Sketch of a transverse slice through the CMS detector. The differently colored lines represent different particle types with their specific signature within the CMS detector complex, taken from [WIKI].

Chapter 4

The Particle Flux Estimation

An important topic for the CMS tracker collaboration is the estimation of the radiation damage on the silicon material caused by running at the LHC. Even though there is a huge variety of radiation studies, the conditions during the ongoing experiments are different than in any laboratory.

One of the first steps in order to determine radiation damage effects quantitatively is to obtain a profound knowledge of the particle flux exposure of the different sensors.

4.1 The Fluka Simulations

The Fluka package is a tool computing particle interactions with matter and electric or magnetic fields based on Monte Carlo simulations [Ferrar, BaMuSa]. It was used [Müller] to model the geometry of the CMS detector and has been recently updated by Moritz Guthoff to increase accuracy. In combination with the DPMJET3 [RoEnRa] event generator a map of the average radiation within the tracker volume per p-p collision could be obtained. The radiation field is dependent on the center-of-mass energy of the collision. The calculations have been performed for 7 TeV and for 14 TeV. A statistical error is calculated by comparing different runs. It stays below 2%, with a statistic of 15000 p-p collisions. The results provided in cylindrical coordinates are symmetric in the azimuthal angle. In the model also the energy of the particles is used. In this way, it is also possible to weight different particle contributions according to the NIEL hypothesis (see section 2.2.2). Figure 4.1 shows the average particle flux, re-weighed to 1 MeV neutron equivalent, inside the tracker volume.

It is worth noting that the distribution of radiation levels is different for charged and neutral particles. While charged particles are predominantly coming from the main collision and are falling off in r, the situation for neutral particles is different. For neutrons the material budged plays a substantial role consequently the radiation distribution is dominated by these. In figure 4.2 a comparison between charged and neutral contributions to the particle fluence is shown.

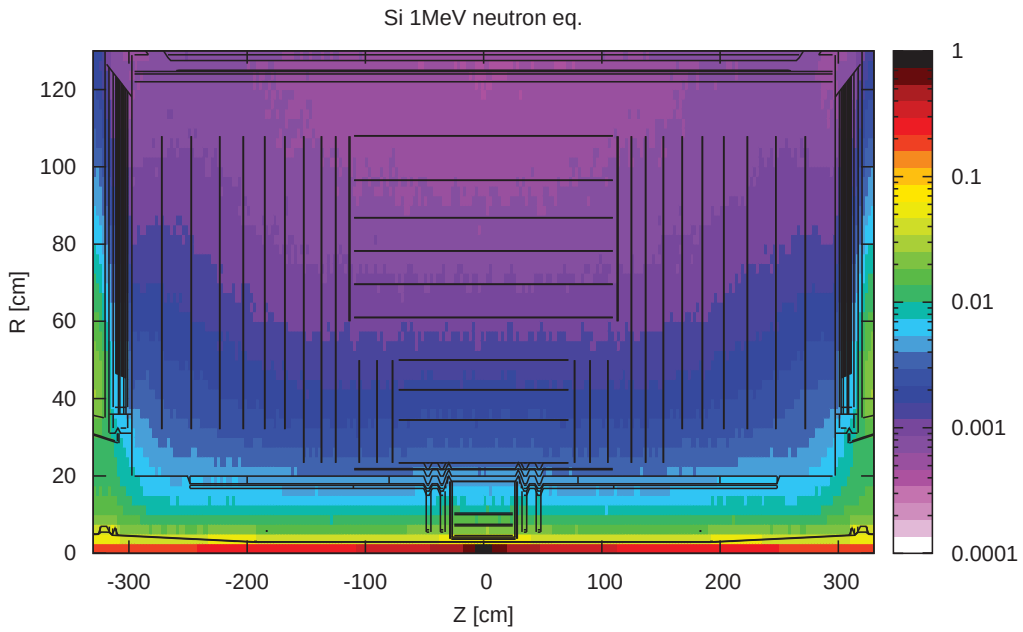

Figure 4.1: The average particle fluence, equivalent to 1 MeV neutron flux, is shown in the tracker volume per p-p collision in cylindrical coordinates. The different colors correspond to different radiation levels. The black lines indicate material budged, such as silicon layers of the tracker and support structures. All calculations were done for 7 TeV center-of-mass energy [Guthof].

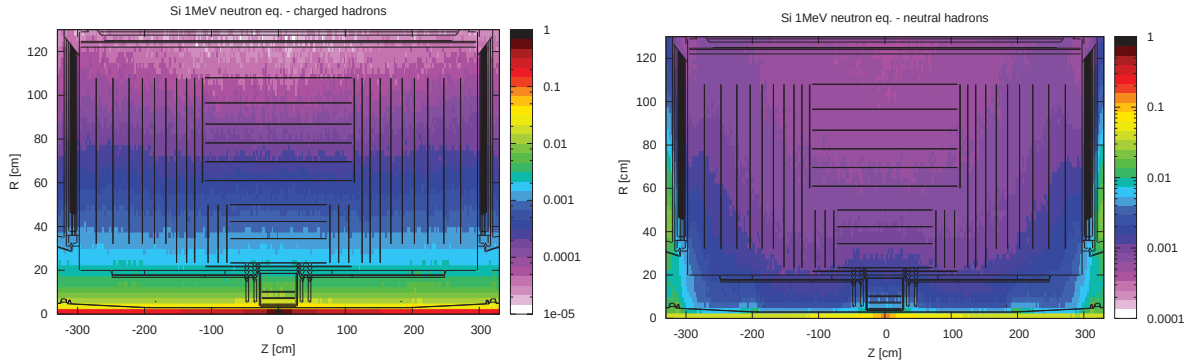

(a) Charged particles (b) Neutral particles

Figure 4.2: Contributions to the particle fluence for (a) charged particles only and (b) neutral particles only per p-p collision. Both plots are simulated at a center-of-mass energy of 7 TeV and scaled to 1 MeV neq according to the NIEL hypothesis [Guthof].

4.2 Luminosity Estimation and p-p Cross Section

An accurate measurement of the luminosity (compare section 3.1.2) is important due to a variety of reasons:

Firstly, it defines the production rate of physics events, whose maximization is one of the primary aims.

A detailed knowledge of the luminosity is important for many physics analyses, when the number of expected events is important.

The luminosity is a direct measure of the amount of radiation exposure of the sensors.

The online luminosity measurement in CMS is performed using data from the HF (see subsection 3.2.2). The luminosity is calculated every few seconds. The achieved accuracy is 11%. The measurement is calibrated with dedicated *Van der Meer* (VDM) scans pioneered at CERN in the 1960's. In these special fills the beams are varied through one another and the beam size at the interaction point is determined. Further details about VDM scans and the luminosity measurement of CMS can be found in [MeaLum]. In addition, an offline calculation of the luminosity based on an analysis of the read out pixel clusters is performed (see [UpdLum]).

Two different luminosity values are stored in the CMS databases:

The delivered luminosity, which is the raw luminosity created by the LHC, important to assess the radiation damage to the microstrip tracker.

The recorded luminosity, which results out of folding the raw luminosity with the data taking efficiency of the CMS detector. This quantity is important for physics analyses.

The final ingredient for a conclusive information of the particle fluence within the detector is the p-p cross section value. With the cross section and the integrated luminosity the number of created events can be derived (see equation 3.4). This can be further translated into a fluence value for a given location within the tracker volume using the Fluka results (see section 4.1). The inelastic p-p collision cross section was one of the main fields of research of the TOTEM collaboration and has been determined to be 73.5 mb [PPCros].

Chapter 5

Leakage Current within the CMS Tracker

5.1 Leakage Current Measurement Techniques of the CMS Tracker

The increase of the sensor's leakage current is one of the most striking effects of radiation. For that reason a strong effort has been put into an accurate monitoring of this quantity with a high granularity. The specific details of the leakage current determination are discussed in the next subsections.

5.1.1 The Detector Control System

The *Detector Control System* (DCS) is the main interface to the hardware of the tracker. Its main purpose is to manage the operational state of the tracker and to monitor the voltages, currents, temperatures and humidities. The DCS is built with PVSS (Prozess Visualisierungs- und Steuerungs-Software) a *supervisory control and data acquisition* (SCADA) software package developed by the ETM company [ETM]. The tracker DCS ([MaLiFi]) is a huge software project, with around 100000 parameters from the power supply system, 100000 parameters from the data acquisition (DAQ) (see subsection 5.1.2) and about 1000 environmental probes inside the tracker volume. It is distributed on 10 PCs and 10 PLCs. A *finite state machine* (FSM) is managing the transitions between the various tracker states. Alerts are defined for the relevant temperature and power supply readouts, informing the central DCS shifter immediately. The central DCS shift is one of the most important shifts for the safety of CMS and is covered day and night, seven days a week.

In addition to the control and monitoring of the above-mentioned parameters, the DCS system is archiving all important data in a dedicated database. The stored data covers all alerts and alarms, the currents and voltages in each of the 4000 power supply

channels, the temperature and humidity measurements, the data sent from the DAQ and much more.

Each of the power supply channels serves power to 3 to 12 modules. The readout electronics are provided with low voltages (1.25 V and 2.5 V). The sensors are biased with a high voltage (HV) of 300 V to deplete the bulk from free charge carriers. The corresponding current measurements of the HV lines contain the bulk leakage current and the surface current. The surface current has been determined to be in the order of less than 100 pA during the quality assurance phase [Bergau], while the bulk leakage current is in the order of 10 μA (compare figure 7.7). Thus, the total leakage current is clearly dominated by the bulk leakage current. In the following, the term *leakage current* is used for the bulk leakage current if not specified differently.

This type of leakage current measurement has a high precision ($\pm$ 1 μA) and is available at any time, even when the DAQ is not running. Its disadvantage is the low granularity, since the read-out value is a superimposition of the leakage current values of all connected modules.

5.1.2 The Detector Control Unit

The *Detector Control Unit* (DCU) is an *Application-Specific Integrate Circuit* (ASIC) mounted on the hybrid of all modules in the silicon strip tracker. Further details about the DCU can be found in [MaMaMo]. The DCU is able to provide temperature measurements at the hybrid and at the sensor itself. In addition, the leakage current and the operational voltage of the low voltage channels powering the electronics can be retrieved. The whole data is read out by the data acquisition for each module individually during periods in which the data acquisition is running. Each 300 seconds the DAQ is sending the DCU measurements via a PSX server to the detector control system of the tracker (see subsection 5.1.1).

The main benefit of the DCU measurement is the high granularity, with one individual measurement per module. The correlation between the power supply leakage current measurements and the sum of the corresponding DCU measurements is shown in figure 5.1.

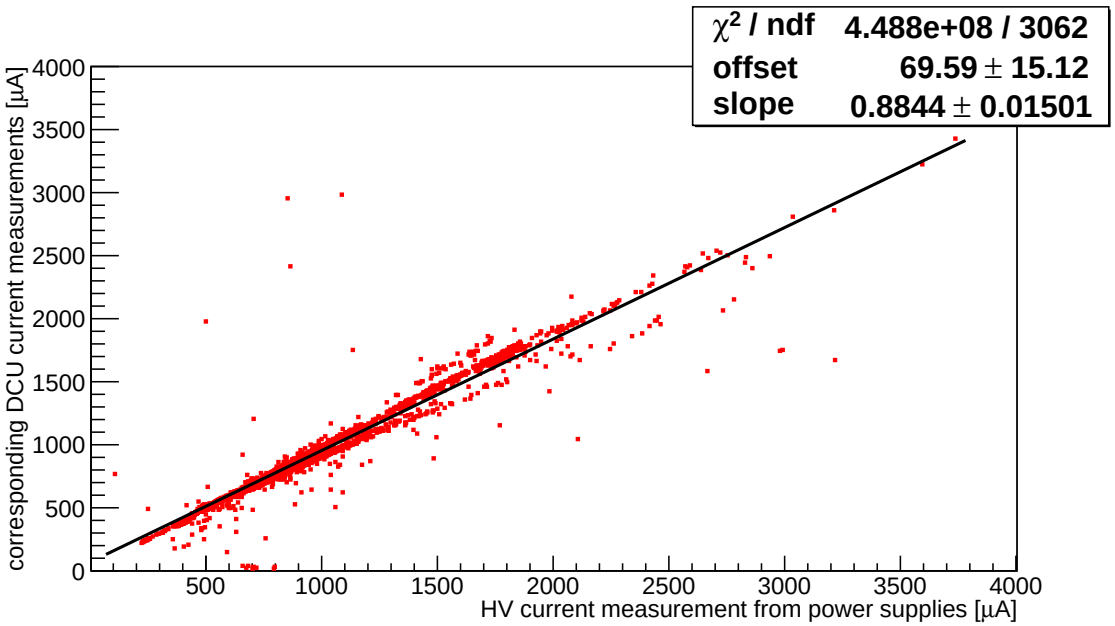

Figure 5.1: Correlation plot between the leakage current measurements of the power supply system and the summed leakage current of the DCU measurements of the corresponding modules. The red squares represent measurements, the distribution is fitted with a first order polynomial (black line). The plot was generated mid 2012 at a integrated luminosity of about 20 fb^{-1} [Potenz].

The accuracy of the temperature reading of the DCU is not as good as the leakage current measurement for the sensors within the tracker. The reason for that is the discrepancy between the average sensor temperature and the design value of the temperatures. The DCUs are optimized with regard to their dynamic range for low temperature values between -10 °C and 10 °C. In some regions of the innermost TIB layer of the detector the sensor temperatures exceed 40 °C, and therefor the linearity of the output is not optimal anymore.

5.2 Properties of the Leakage Current of the CMS Tracker

5.2.1 I-V Behavior

The leakage current is dependent on the depletion zone width (see subsection 2.1.4), and thus also on the bias voltage applied to the sensor. In principle, the leakage current increases with the bias voltage and saturates when the full depletion voltage is reached. If the applied bias voltage exceeds a certain threshold, an *avalanche breakdown* occurs leading to a large increase in current. This happens when the electric field is strong

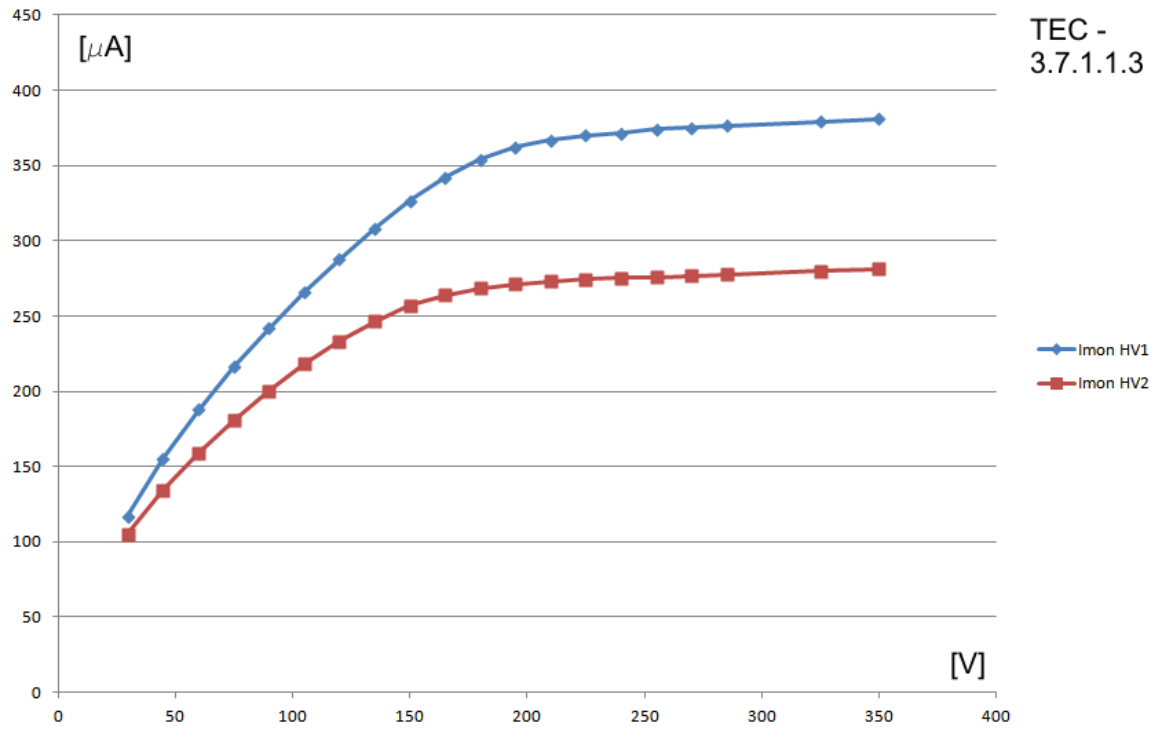

Figure 5.2: I-V curve of the two high voltage channels of one power supply of the CMS microstrip tracker.

enough to sufficiently accelerate the charge carriers in the transition region to create electron-hole pairs on their own due to collisions with bound electrons. The sensors of the CMS tracker have been tested during the quality assurance phase and possess a guaranteed breakdown voltage above 500 V, most sensors even above 800 V ([Dierla]). The optimal operating point of the sensors is at the plateau between full depletion and the breakdown.

An example curve of the I-V behavior of one power group of the tracker is shown in figure 5.2.

5.2.2 Temperature Distribution in the CMS Tracker

It has been shown in equation 2.39 that the bulk leakage is strongly dependent on the temperature of the material. The temperature distribution within the CMS strip tracker is not uniform. A snapshot of the sensor temperatures within the CMS tracker is shown in figure 5.3.

This temperature distribution differs considerably from the design goal of $-10°$ C. There are several reasons for the deviations:

The set point of the cooling plant is set to 4° C, since the humidity measurements around some support structures in the bulkhead region of the tracker indicate

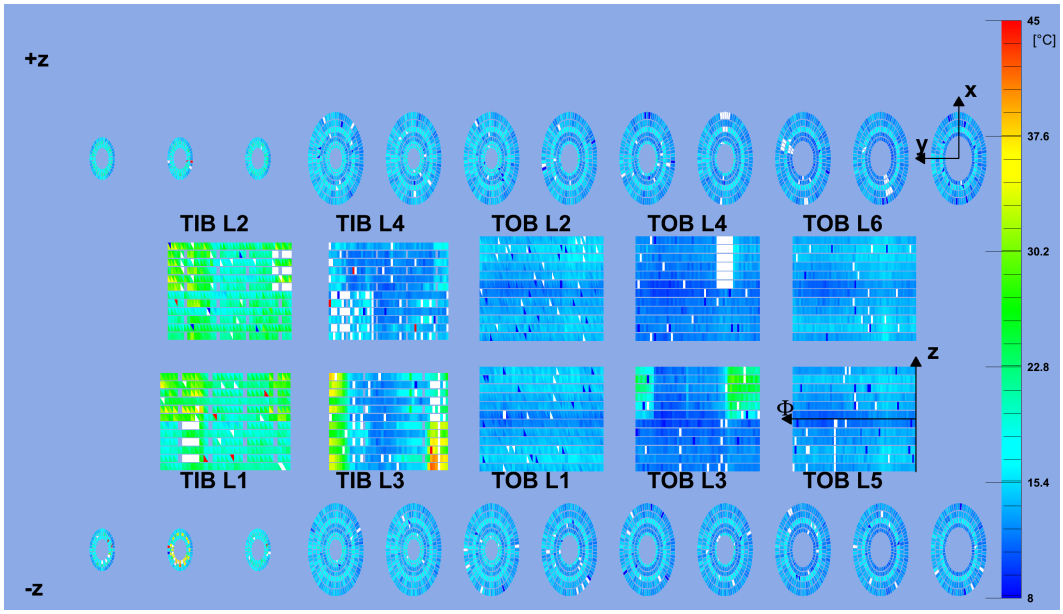

Figure 5.3: Map of the sensor temperatures within the CMS silicon strip tracker measured by the DCUs during data taking. The colors represent the different temperatures while each square or triangular in the double sided layers symbolizes a module. White fields correspond to missing or uncalibrated DCU readings. Clearly visible are high temperatures in the first two layers of TIB, where the modules are mounted back to back. In addition, modules with a suboptimal cooling contact (mainly in TIB layer 3 and TOB layer 3) can be identified.

that the environment is not dry enough to further reduce temperature. It is one of the primary goals of the long shutdown in 2013 and 2014 (LS1) to correct the sealing of these offending structures. The improved humidity protection gained in this way will allow to operate the CMS tracker at lower temperatures.

Some of the cooling loops have been closed on purpose due to high leakage rates of the cooling liquid within these circuits. These areas are only cooled passively by the surrounding air. There are also plans to partially recover parts of this outage during LS1, however it is expected that it will not be possible to recover all leaking circuits. With only passive cooling the modules will most probably not endure the planned LHC irradiation within the next 10 years. Projections for future leakage current evolutions will be presented in section 8.1. A list of the closed cooling loops is shown in table 5.1.

Besides these unwanted effects, the temperature also depends on the density of the operated sensor material. This applies most demonstratively to the layer one and two of the TIB partition. In this region, two single sided modules are mounted back to back (see subsection 3.2.1).

Partition	Side	Power Group	Cooling Plant	Cooling Loop
TIB	+	3.6	Ss2	26
TIB	-	3.5	Ss2	25
TIB	-	3.6	Ss2	23
TID	-	4	Ss2	30
TOB	+	3.1	Ss2	44

Table 5.1: List of the closed cooling loops within the CMS microstrip tracker.

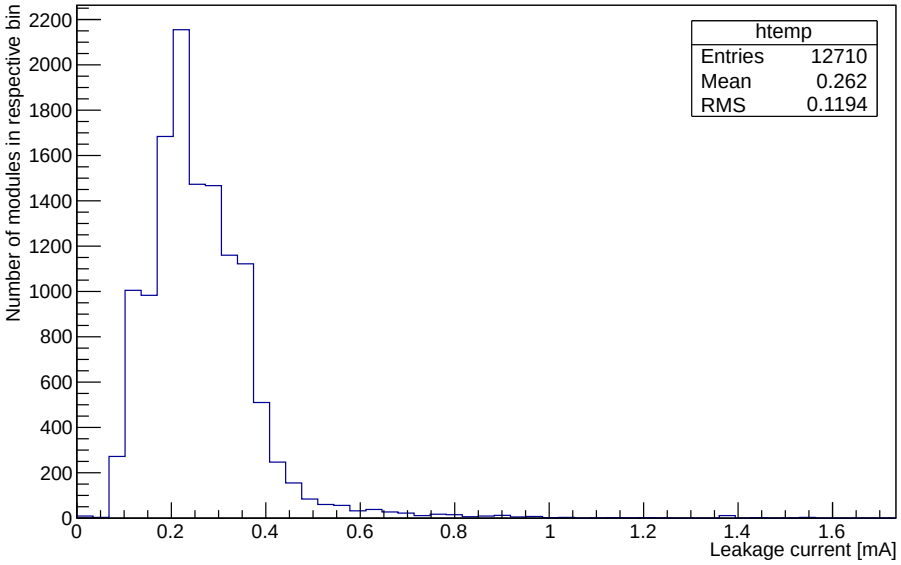

Figure 5.4: Histogram of the leakage current measurements of the calibrated DCUs at an integrated luminosity of 25 fb^{-1}.

5.2.3 The Leakage Current after 25fb^{-1}

The high operational temperatures lead to high thermally induced leakage currents (see equation 2.38). The distribution of the leakage current values measured by the DCUs at an integrated luminosity of 25 fb^{-1} is drawn in figure 5.4.

In the innermost layer of the TIB partition high operational temperatures meet high fluence exposures. In this region the most severe leakage currents can be found. The distribution of the TIB layer 1 leakage currents is shown in figure 5.5.

5.2.4 Effective Alpha Values

As previously shown, the increase in leakage current is proportional to the fluence, the sensor volume and a temperature dependent damage factor called α (see equation 2.53). Additionally, the leakage current decreases with time, depending on the given temperatures as it was shown in subsection 2.2.3.

The particular characteristic of the leakage current evolution in a running experiment

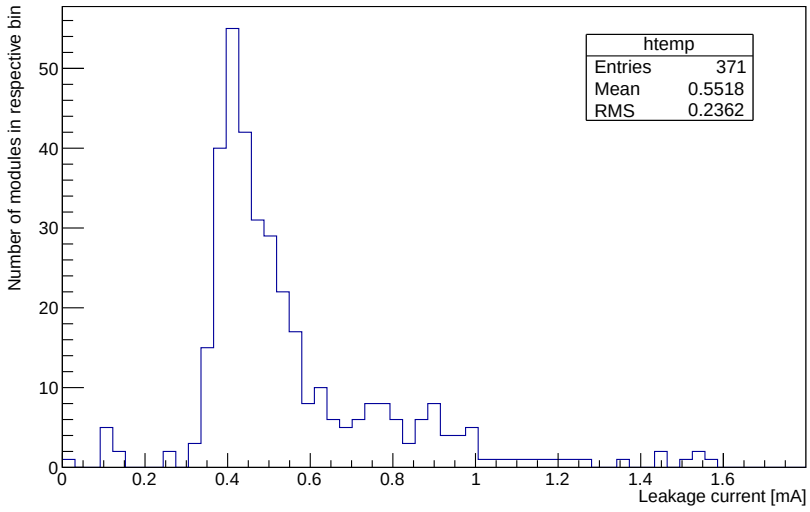

Figure 5.5: Histogram of the leakage current measurements of the calibrated DCUs at an integrated luminosity of 25 fb^{-1} for layer 1 of TIB.

compared to a conventional laboratory measurement is, that the fluence exposure is distributed over long periods. Due to this, an *effective alpha* value also depends on the fluence distribution over time $\Phi(t)$. Moreover, the sensor temperatures vary with the different states of the detector. Thus an effective α value also depends on the temperature profile $T(t)$:

$$I = I_0 + \alpha_{eff}(t, T(t), \Phi(t))\Phi V. \tag{5.1}$$

Further details about the effective α value and its calculation are given in chapter 7.

In order to compare the leakage current values they have been normalized with respect to three different dependencies:

To account for different temperatures, we scaled the currents to a reference temperature of 0 °C, which has been performed using equation 2.39.

The comparability of different sensor volumes are warranted by calculating the leakage current per unit volume of 1 cm^3.

The fluence dependency is expressed in a leakage current increase per fb^{-1} of integrated luminosity.

Based on these assumptions, the slope of the normalized leakage current over the particle fluence will give us the effective alpha value of the silicon sensors. We expect the slope to change with altering fluence and temperature profiles.

In figure 5.6 two example distributions for different integrated luminosity values are shown for the normalized leakage current against the calculated particle fluence. Both plots are created with measurements at a certain point in time. The differences in fluence arise from the various positions within the tracker volume, and thus with distinct doses of radiation. The fluence estimation is performed using the module position and a fluka simulation (4.1). The leakage current is normalized to an active sensor volume of 1 cm^3, to a temperature of 0 °C (based on equation 2.39) and to 1 fb^{-1} integrated luminosity. The leakage current is also averaged for equal fluence values.

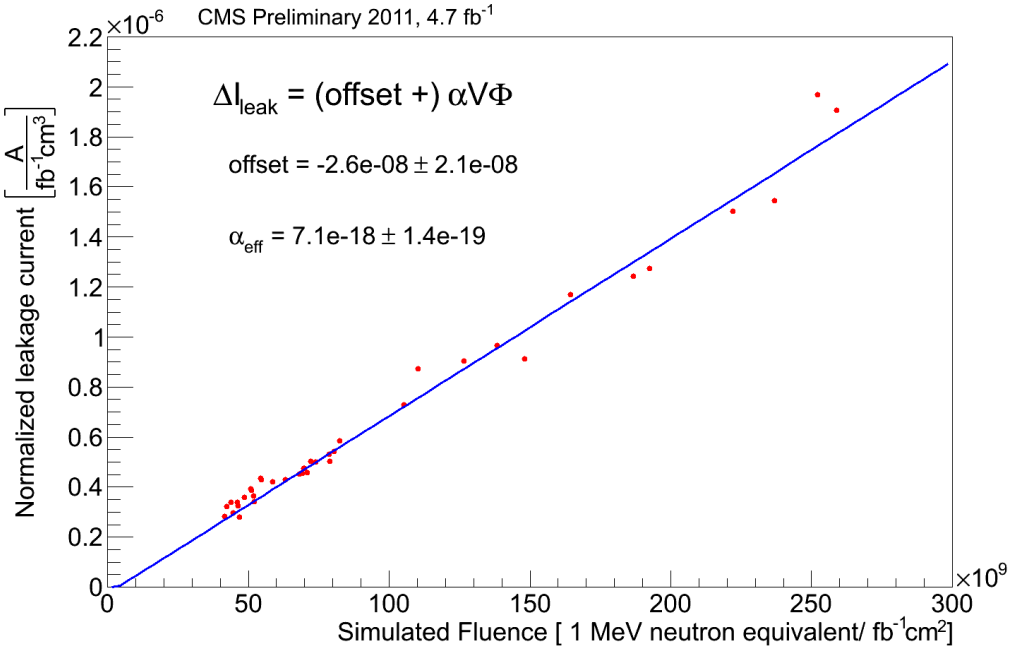

(a) Normalized leakage current vs. fluence for 4.7 fb^{-1}

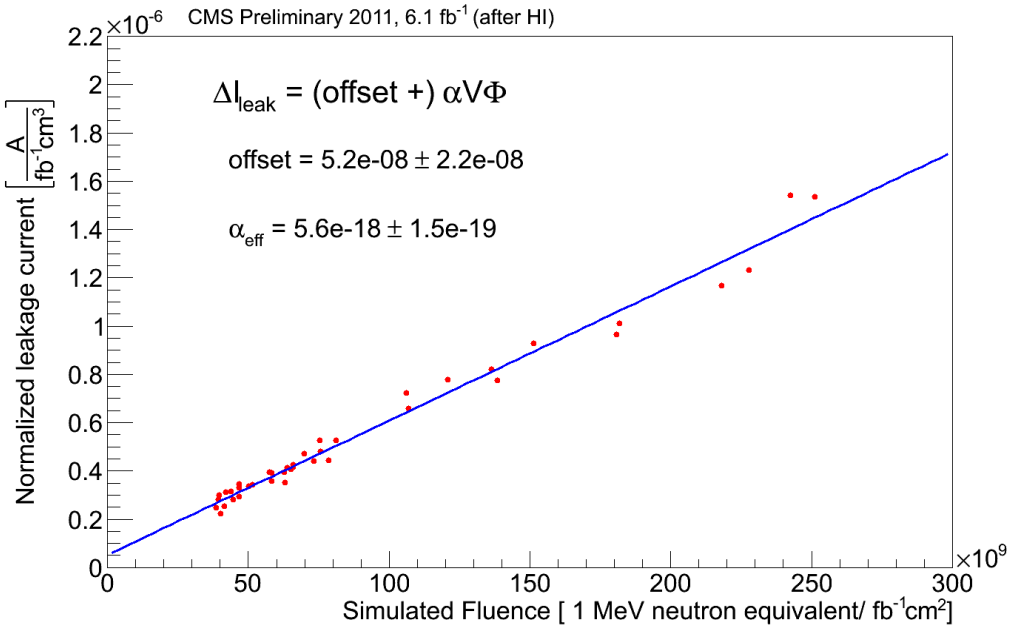

(b) Normalized leakage current vs. fluence for 6.1 fb^{-1}

Figure 5.6: The figures show two different snapshots of the normalized leakage current distributions in the barrel layers of the CMS tracker plotted against the calculated 1 MeV neq. fluence. The upper plot was made for measurements at 4.7 fb^{-1} towards the end of 2011 proton-proton collision running. The lower plot uses data from the end of 2011 heavy ion running at 6.1 fb^{-1}. During the heavy ion period the luminosity of the LHC is very low, making annealing the dominant source of leakage current change.

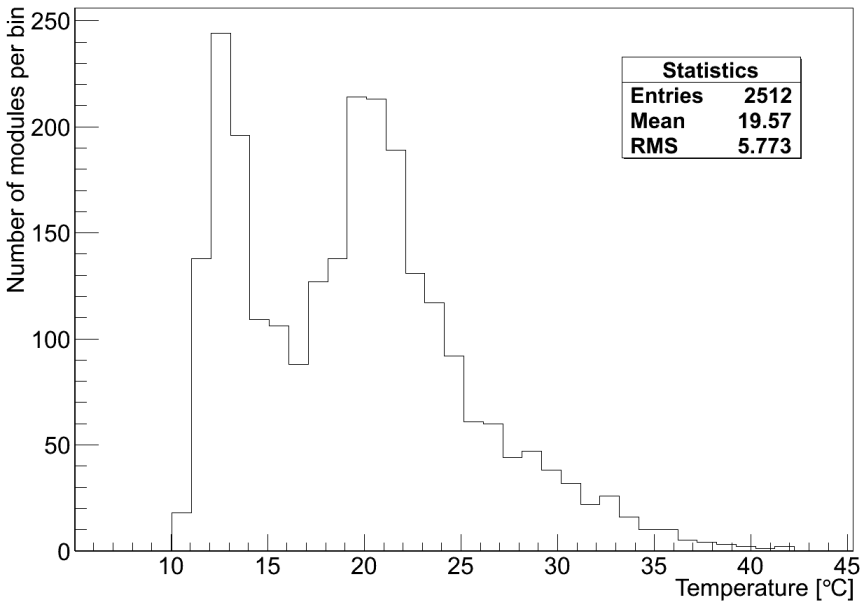

Figure 5.8: Histogram of the temperature distribution for the inner barrel layers of the CMS tracker. The double peak structure arises from the fact that in TIB layer 1 and 2 modules are mounted back to back (compare 3.2.1) leading to higher temperatures then the single sided modules in layer 3 and 4.

The total integrated luminosity delivered by the LHC during 2009 and 2010 was 19.57 fb^{-1}. During 2011 running, a total integrated luminosity of 6.1 fb^{-1} has been achieved (see figure 5.7). Considering the different orders of magnitude, the radiation damage before 2011 is negligible.

Even though the leakage current values are scaled with regard to the temperature in the plots of figure 5.6, it is not expected that the distribution is linear. Since the temperatures are changing with the position in the barrel layer, the annealing effect is also different at distinct locations. Nevertheless, a rough comparison between the measurement and the expectations can be performed.

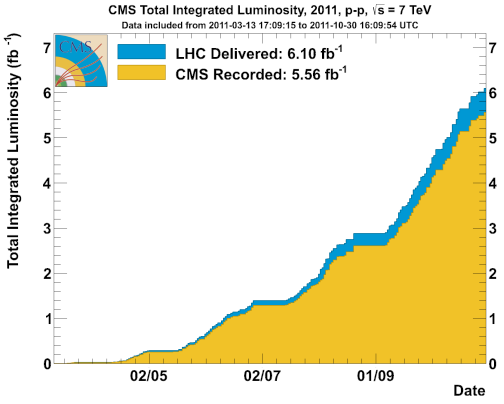

Figure 5.7: Luminosity profile of 2011 p-p collision running. Taken from [Lumino].

In order to classify the effective α value measurement, the value needs to be scaled to the original temperatures, since the temperatures are essential for the annealing terms. The temperatures in the inner barrel region vary from 10 °C to 42 °C (see figure 5.3). In a rough approximation, the mean value of the temperature distribution is employed, which is 19.6 °C. The distribution is shown in figure 5.8.

A scaling of the temperatures from 0 °C to 19.6 °C translates into a factor of 6.4

according to equation 2.39. For the slope derived in figure 5.6a this leads to a resulting α value of $4.54 \cdot 10^{-17} \mathrm{A}/\mathrm{cm}$.

In figure 5.9 the standard parameters (see equations 2.61) are used to determine the α value in dependency on the temperature for different annealing lengths. A value of $4.54 \cdot 10^{-17}$ A/cm at 19.6 °C would correspond to annealing durations between 5 and 20 days. The effective alpha is a superimposition of multiple annealing durations between minutes and several months. The contribution of shorter annealing periods is larger since the slope of the integrated luminosity profile is increasing over the year (compare figure 5.7). In this context, the fitting procedure delivers reasonable results, using only this rough approximation.

The slope of figure 5.6b corresponds to $3.58 \cdot 10^{-17}$ A/cm, which translates to an annealing duration of slightly more than 50 days according to figure 5.9. The measurements were taken at the end of heavy ion running in 2011, with more than one month of annealing time between the last irradiation from p-p collisions. Given that the fluence during heavy ion collisions is negligible, the fitted value matches the expectations sufficiently for this qualitative validation.

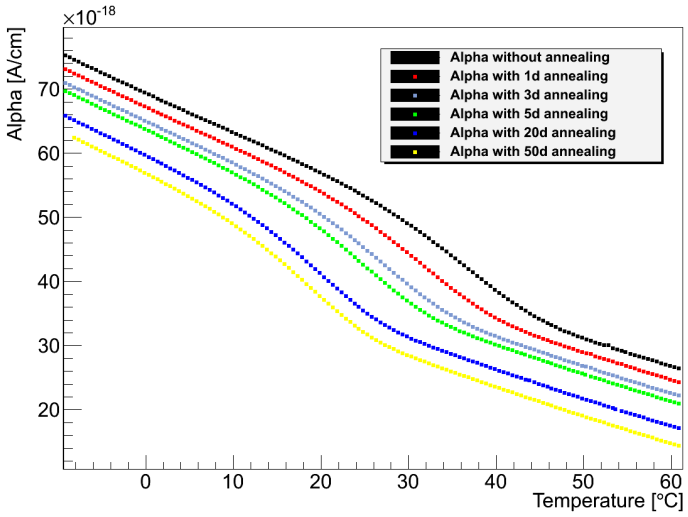

Figure 5.9: Alpha value for different annealing durations in dependency on the temperature; based on the parameters presented in [Moll].

5.2.5 Leakage Current Fluka Simulation Correlations

For the barrel partitions of the CMS tracker, the fluence profile is sufficiently flat (compare figure 4.1) to perform another sanity check: compare r-dependency of the normalized leakage current with the corresponding values from the Fluka simulations. The analysis has been performed using the same normalization as before: to 0 °C and per cm^3.

The needed α value to compare fluence with leakage currents was taken from the two fits in section 5.2.4. Figure 5.10 shows the measurements of the normalized leakage current for the barrel partitions of the tracker at 4.7 fb^{-1} versus the distance to the beam pipe r (red dots). The blue curve is a fit of these measurements using a power

law approach. The red curve corresponds to the calculated leakage current using the Fluka simulation of the particle fluence and the fitted effective alpha value of plot 5.6a.

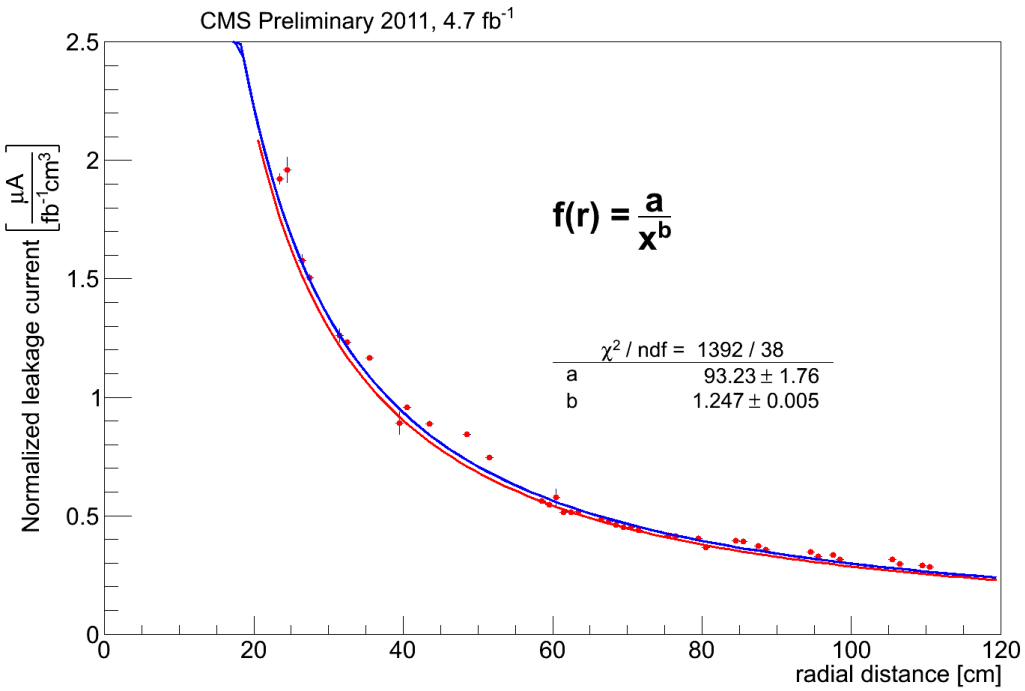

Figure 5.10: Comparison between the measured leakage current in the barrel region of the tracker (red dots fitted with blue curve) and the Fluka simulations of the particle fluence (red line), scaled with an effective alpha value obtained from a linear fit of the leakage current versus expected fluence plot.

Since the effective alpha value was obtained by a linear fit already using the Fluka simulations as an input, per construction we do not expect a large deviation between the two curves. The fact, however, that the radial trends of the two curves are similar supports the credibility of the fluence expectations.

It has to be noted that the used Fluka simulations were created by Moritz Guthoff using an updated material budged of the tracker and differ from the expected fluence profiles presented in the technical design report of the tracker [TDR].

Chapter 6

The Full Depletion Voltage within the CMS Tracker

The full depletion voltage depends on the effective charge carrier concentration and the thickness of the sensor (see equation 2.30). These values vary within the tracker from about 100 V to almost 300 V. It was mentioned before (compare subsection 3.2.1) that the p-in-n sensor technology undergoes type inversion during irradiation. In order to utilize this effect beneficially, the sensors were selected in a way, that the sensors with the highest initial full depletion voltage are mounted at the inner layers, where the fluence exposure is the biggest. For the modules with two sensors, the difference in the full depletion voltage of the two sensors was kept as small as possible.

The initial full depletion voltage of the sensors has been determined in C-V measurements during the construction of the tracker. In this type of measurement the capacitance of the sensor is measured while the applied bias voltage is varied within the region of interest.

The capacitance of the sensor depends on the width of the depletion zone. With an increasing depletion zone width, the capacitance decreases up to the asymptotic value. This value is reached when the complete bulk is depleted. An example curve of a C-V measurement is shown in figure 6.1.

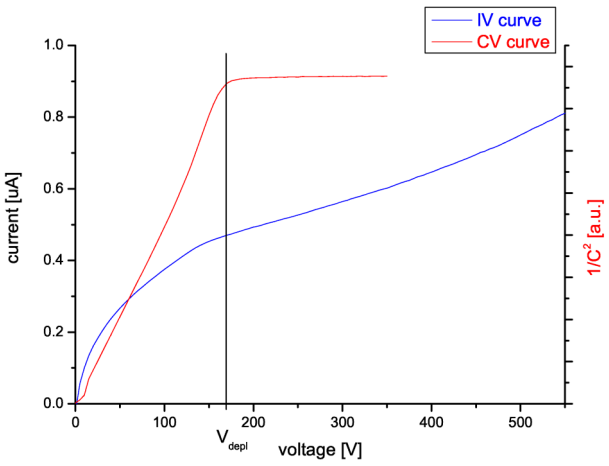

Figure 6.1: Example of the current and $1/C^2$ over bias voltage measured during the quality assurance phase of the tracker construction. The saturation point of the $1/C^2$ curve defines the full depletion voltage of the sensor [Berga2].

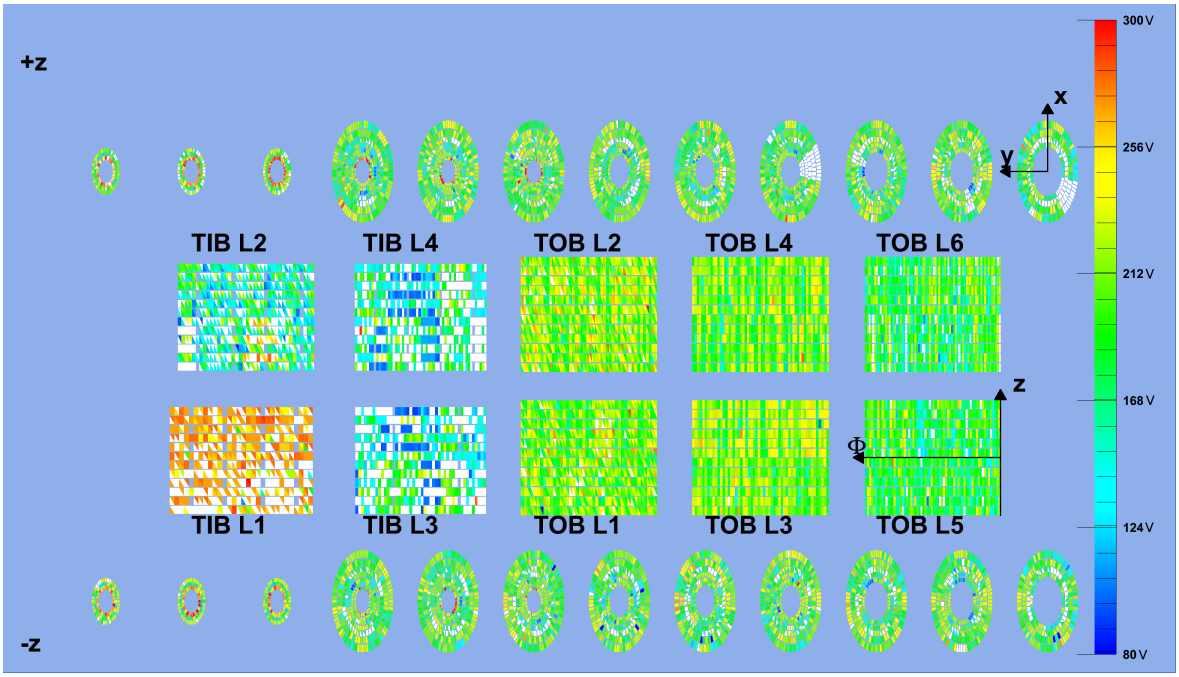

Figure 6.2: Map of the initial full depletion voltage values of the CMS tracker. The six small rings on the left correspond to the TID partition. The 18 big rings represent the wheels of the TEC partition. In the middle the four layers of the TIB and the six layers of the TOB are shown.

In figure 6.2 a map of the modules of the CMS tracker is shown. The different colors represent different initial full depletion voltage values. Also, one has to keep in mind that the thickness has been chosen in such a way that the thin modules are at locations with higher fluence exposure, while the thick sensors are further away from the interaction point (see section 3.2.1).

All full depletion voltage measurements do have one aspect in common: a scan of the bias voltage settings is needed. The bias voltage can be set by the tracker DCS system for every *high voltage* (HV) channel independently. The tracker uses A4601 power supplies from the CAEN company. According to the specifications, the accuracy of the voltage setting versus the voltage output is $\pm 1\% \pm 0.5$ V [CAEN]. In practice, an accuracy of ± 3 V was considered to be realistic among the whole range of the scans.

As long as the leakage current within the module's sensors is negligible, it is fair to assume that the bias voltage applied to the actual sensors is close to the voltage set at the power supply system. With increasing leakage currents this approximation is getting worse due to the leakage current induced voltage drop on the module and the cable. In figure 6.3 the computed correction of the effective bias voltage is plotted versus the power supply HV value for an example module. The extent of correction is highly dependent on the leakage current of the individual module.

The total voltage drop on the cable and the module can be written as:

$$\Delta V = I_{HVChannel} R_{MotherCable} + I_{Module} R_{Module} \tag{6.1}$$

The resistance values can be estimated to be $R_{MotherCable} = 1\,\mathrm{k}\Omega$ and $R_{Module} = 13.8\,\mathrm{k}\Omega$ [Demari]. The leakage current itself is also dependent on the applied bias voltage, and thus it is not constant during a HV scan (see figure 5.2). In order to correct the bias voltage ($V_{effectivebias} = V_{powersupply} - \Delta V$), an individual correction for each step of the scan needs to be computed based on the corresponding leakage current measurement.

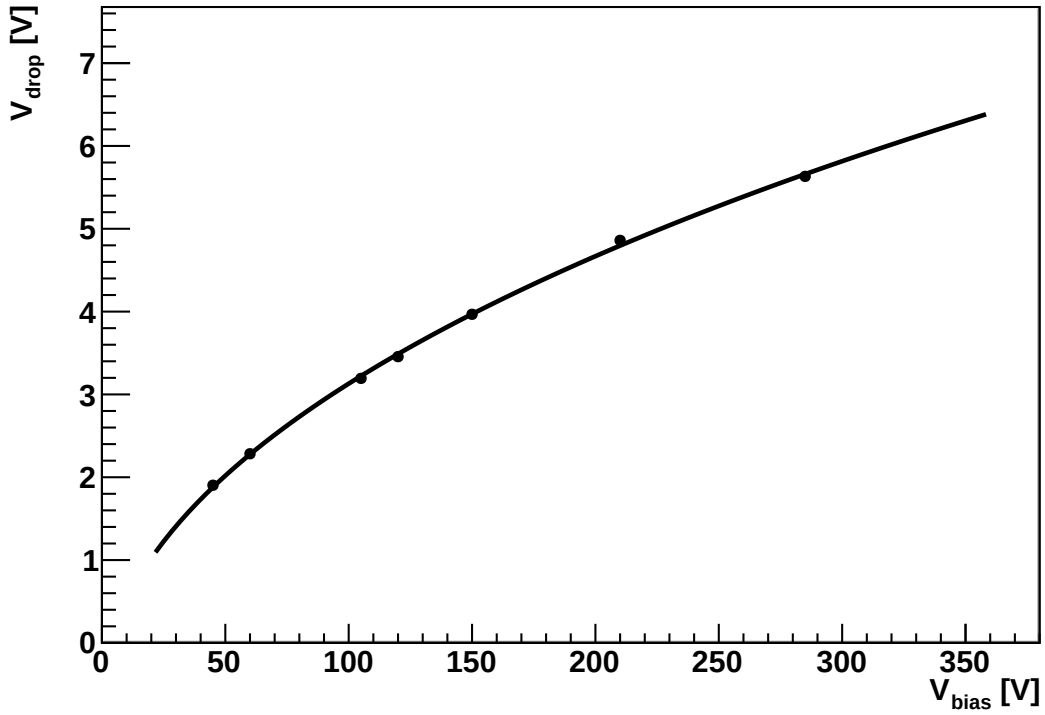

Figure 6.3: The computed bias voltage correction V_{drop} caused by a voltage drop on the mother-cable and the module's electronic due to leakage current, is plotted versus the applied high voltage for an example module [AgrFon].

In the next two sections an introduction to two measurement approaches is given, developed to determine the full depletion voltage during the running experiment. Some details about the methods are also discussed in [Barth1].

6.1 The Noise Bias Voltage Scan: An In-Situ Approach

For the operation of a high energy physics experiment, it is important to monitor the sensor's evolution of full depletion voltage. The measurement of this property, however, is more complex than the measurement of the leakage current. It cannot be measured without interrupting normal operation, as it is possible for the leakage current. Also, a standard method to determine the full depletion voltage, the C-V measurement cannot be performed in the CMS since there is no option to directly measure the capacitance.

Yet, it is possible to analyze the noise behavior in dependency on the applied bias voltage. As it was previously mentioned (see section 2.1.6), the noise depends on the capacitance, and thus also on the full depletion voltage.

The development of the noise bias scan has been done on an experimental detector: the *cosmic rack* (CRack). As the name suggests there is no particle accelerator connected to the rack, which makes it possible to measure only cosmic rays. The main purpose of this device is, however, to provide a station for the development and testing of upgrades or modifications for the main detector under similar conditions. In this CRack [LaKaSa] sensor rods are built in, which are identical to the ones employed in the TOB partition of the CMS tracker. Also the detector control system and the data acquisition is similar to the one used at point 5.

6.1.1 Principles of the Noise Approach

As mentioned before, the sensors are operated with a reverse bias voltage applied, which increases the depletion zone width. A solid approximation for the width of the depletion zone in the sensor bulk can be obtained by neglecting the built-in potential in equation 2.28 ($V_{bias} \gg V_{bi}$) and further use equation 2.14 under the assumption that we have a dominant doping concentration. This leads to:

$$W = \sqrt{2\epsilon_{Si}\rho\mu V_{bias}}. \tag{6.2}$$

The sensor can be estimated to behave similar like a planar capacitor. Thus, the bulk capacitance decreases linear with the width. This can be expressed by:

$$C_{bulk} = \begin{cases} A\sqrt{\frac{\epsilon_{Si}}{2\rho\mu V_{bias}}} & V_{bias} < V_{FD} \\ A\frac{\epsilon_{Si}}{W_{depletion}} & V_{bias} \geq V_{FD} \end{cases} \tag{6.3}$$

for the full depletion voltage V_{FD} and the sensor thickness $W_{depletion}$.

It was introduced before that the capacitance is one of the main sources of noise. With

2.32, 2.47 and 2.48, the noise can be expressed in terms of the applied bias voltage by:

$$N = \begin{cases} \sqrt{(A + B \cdot \frac{\epsilon_{Si}}{2\rho\mu V_{bias}})^2 + N_0} & V_{bias} < V_{FD} \\ \sqrt{(A + B \cdot \frac{\epsilon_{Si}}{W_{depletion}})^2 + N_0} & V_{bias} \geq V_{FD} \end{cases} \tag{6.4}$$

for the APV specific parameters A and B. N_0 denotes the sum of the remaining squared noise sources, namely

$$N_0 = ENC_{I_L}^2 + ENC_{R_P}^2 + ENC_{R_S}^2 + ENC_{optical\_link}^2 \tag{6.5}$$

with the sensor noise terms out of equation 2.47 and the noise introduced by the optical link.

When a sensor is operated the output of the module, even without traversing particles, is a non-zero value. The average of this strip specific value is called *pedestal* and can be written as:

$$p_s = \frac{1}{N} \sum_{n=1}^{N} r_{s,n}, \tag{6.6}$$

for the number of events N and the readout of strip s at event n: $r_{s,n}$.

The noise value, also called *raw noise*, is the standard deviation of this signal. It is defined by:

$$n_{s,raw} = \sqrt{\frac{1}{N-1} \sum_{n=1}^{N} (r_{s,n} - p_s)^2}. \tag{6.7}$$

It is part of the commissioning of the tracker to measure the pedestal value of each strip regularly several times per year in so-called *pedestal runs*. When the recorded pedestals are found to be reasonable they are stored in the configuration database of the DAQ and used to calibrate the output of the strips.

The bias voltage scan using noise data is performed during downtimes of the LHC. The CMS tracker is brought into local control of both the DAQ and DCS. Local pedestal runs are started for all partitions. During the ongoing runs the bias voltage of all sensors are modified. The high voltage ranges from 30 V to 350 V, in steps of 15 V between 30 V and 300 V, and in steps of 25 V afterwards. Each bias voltage setting is kept until 2000 events per partition are stored.

The resulting pedestal runs are separated later on into a single pedestal and noise analysis per bias voltage setting.

The saturation of the noise over applied bias voltage curve can be used to determine the full depletion voltage. The benefit of this approach is that no beam time is used for this measurement. Thus, it can be done during technical stops without losing any data for physics analysis. The downside of this method is that the accuracy is not very high and that the identification of the saturation can be difficult under certain conditions. Nevertheless, it is a promising approach that has been proven to work.

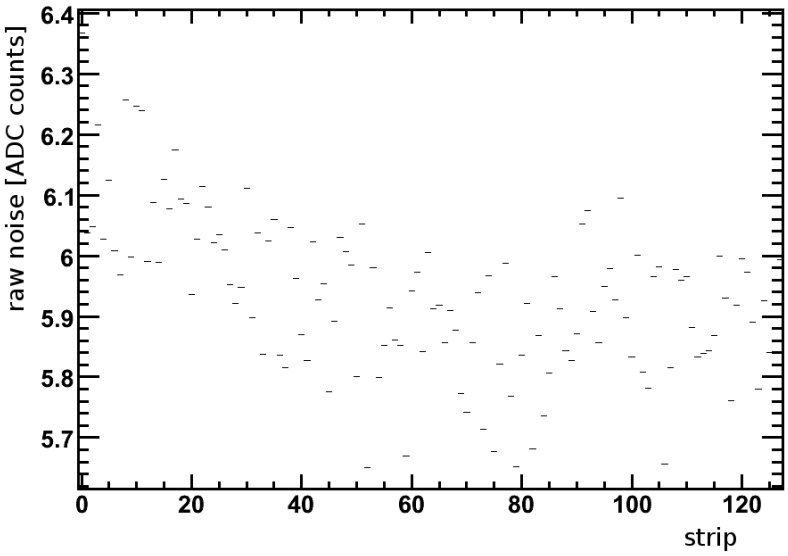

Figure 6.4: Histogram of the noise value per strip of an APV example with 128 channels. The noise value is provided in ADC counts by the analog digital converter.

The improvement of the analysis and the automation of the measurement is an ongoing effort of the tracker collaboration.

6.1.2 Analysis of the Noise Method

The analysis of the noise bias scan is performed in several steps. After the raw files have been separated into one file per partition and bias voltage setting, the standard pedestal analysis is executed. Part of the analysis is the computation of a raw noise value per strip. Figure 6.4 shows an example of the noise values within an APV of a module at a bias voltage above full depletion.

The noise values are stored in one histogram per APV. The resulting distribution can be approximated by a Gaussian fit, which describes the random fluctuations. However, there are also effects that alternate the distribution. Faulty or noisy strips jut out of the common range. In addition, secondary noise can be induced in the strips by its surroundings, primarily in the strips at the borders.

For the noise versus bias voltage relationship, we focus on the bulk of the distribution and cut out noise values that exceed the mean value of the distribution by a distance of one sigma. The mean value of the trimmed distribution is stored together with its spread. This value is used as the average noise value (or uncertainty of the noise value respectively) per APV and per bias voltage setting.

In figure 6.5 the distribution of the noise values of an APV is shown with the initial

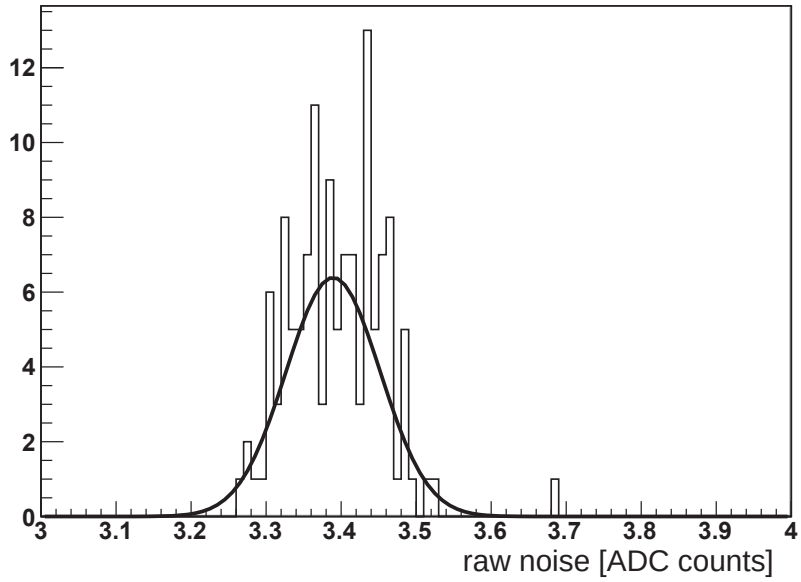

Figure 6.5: Example distribution of the noise values from the pedestal run analysis of an APV. The noise value is given in ADC counts, while the y-axis defines the number of entries in the respective ADC bin. The distribution is fitted with a Gaussian curve.

Gaussian fit.

The noise values obtained in this way are plotted in one graph per APV in dependency of the applied bias voltage. An example plot is shown in figure 6.6. The graph is fitted with the following function:

$$N(V) = \begin{cases} \sqrt{(A + B \cdot \frac{\epsilon_{Si}}{W_{depletion}} \frac{V_{FD}}{V_{bias}})^2 + N_0} & V_{bias} < V_{FD} \\ \sqrt{(A + B \cdot \frac{\epsilon_{Si}}{W_{depletion}})^2 + N_0} & V_{bias} \geq V_{FD} \end{cases} \tag{6.8}$$

using equation 6.4 and 6.2.

N_0 has been fixed, in order to reduce the number of floating parameters. This choice has several reasons:

A measurement of one of the dominant sources in the term that describes the non capacitance noise (N_0) is known, namely the link noise. It has been determined in dedicated commissioning runs of the tracker.

Even with a fixed N_0, the fit is able to account for non capacity dependent noise terms with the parameters A and B.

For A and B the range of the parameters have been limited to improve the stability of the fit. In order to achieve reasonable boundaries on A and B we used the first noise bias voltage scan performed in mid 2010. At this point in time, the radiation exposure

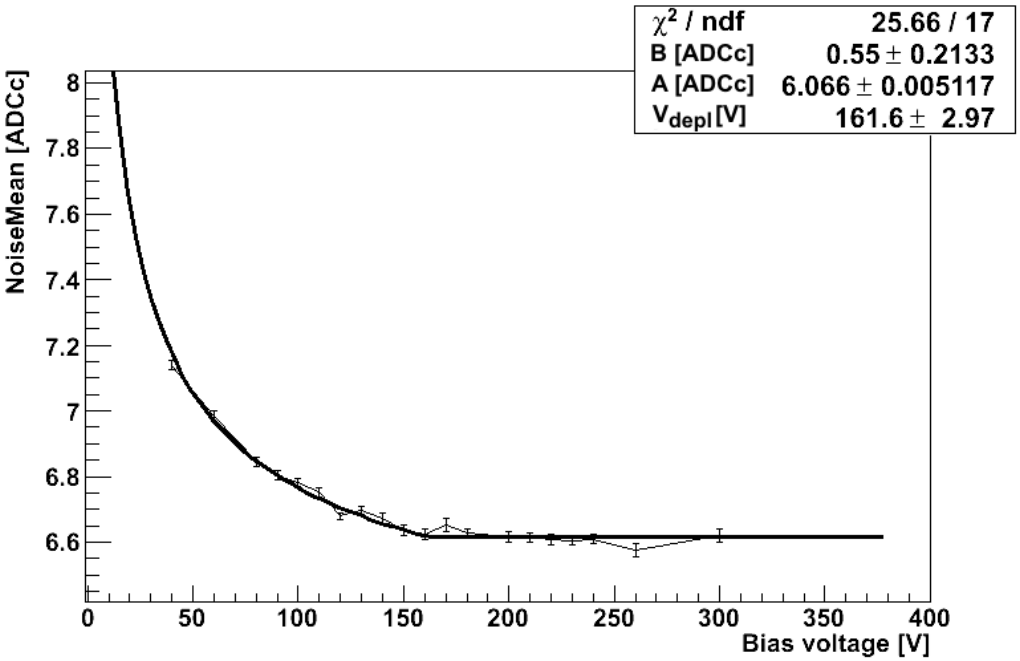

Figure 6.6: The mean value of the Gaussian fit of the noise distribution of an example APV is plotted versus the applied bias voltage. The error bars represent the sigma of the Gaussian fit. The fit in the figure uses the two APV specific parameters A and B (see text). The error margins of the full depletion voltage in the statistics box arises only from the fit and does not correspond to the total uncertainty of the measurement.

of the tracker was minimal, which means that no alternation of the full depletion voltage was expected. We used the full depletion voltage values obtained during the quality assurance phase of the tracker construction with C-V measurements as fixed parameters for the fit. The noise data was then fitted with only A and B being free parameters. The range of the resulting A and B values obtained with the fits are used as limits of the respective parameters.

6.1.3 Performance of the Noise Method

One of the first validations that has to be done is to check the consistency of results obtained by the APVs that are mounted on a single module. The resulting full depletion voltage values should be compatible with each other. Figure 6.7 shows the relative deviation between the fitted full depletion voltage obtained by an APV and the average full depletion voltage of all connected APVs of the respective module, for the TEC minus partition of the tracker.

The comparison of the results of the noise bias scan with the different full depletion voltage measurements is shown in section 6.3.

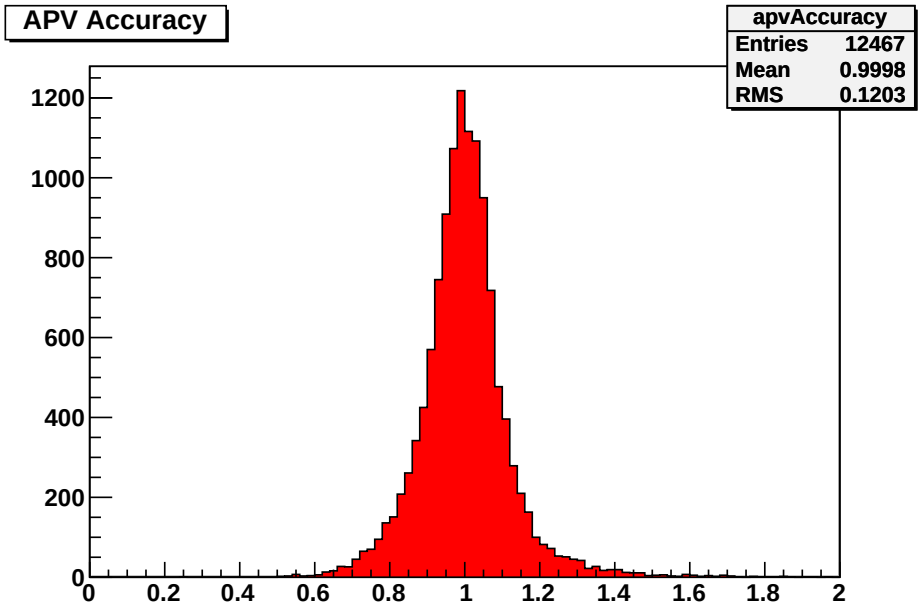

Figure 6.7: Relative deviation between the full depletion voltage measurement of a single APV and the average value of the full depletion voltage from all APVs mounted on the respective module.

As mentioned before, the improvement of the noise bias scan is an ongoing effort. This is true for the measurement itself as well as for the analysis of the data.

A dedicated run type is created for the noise bias scan and tested at the CRack. With this setup the interplay between the detector control system and the data acquisition is synchronized so that the bias voltage is set automatically to the new value between the steps of the measurement. Also, the logging of which bias voltage is applied at which event is done automatically. In this way, no manual action during the scan is needed.

For the analysis it is planned to use the APV specific parameters A and B previously determined by using the measured full depletion voltage values as fixed parameters for all future scans. However, there are several obstacles which need to be overcome.

One problem is that the fit cannot reliably determine the full depletion voltage of sensors if it is high (approximately above 250 V). The reason is that the relative difference between a $1/\sqrt{V_{bias}}$ behavior and a constant value becomes smaller with increasing V_{bias}. At some point the accuracy of the measurement is not high enough to distinguish between these two curves. The way to cope with this is to increase the precision of the measurement. This could be achieved by a more elaborate determination of the noise values and longer measurement durations. The latter approach benefits strongly from an automated measurement since the duration of the procedure as it is now is about 8 hours.

Since p-in-n sensors undergo type inversion it is important to be ready for this future

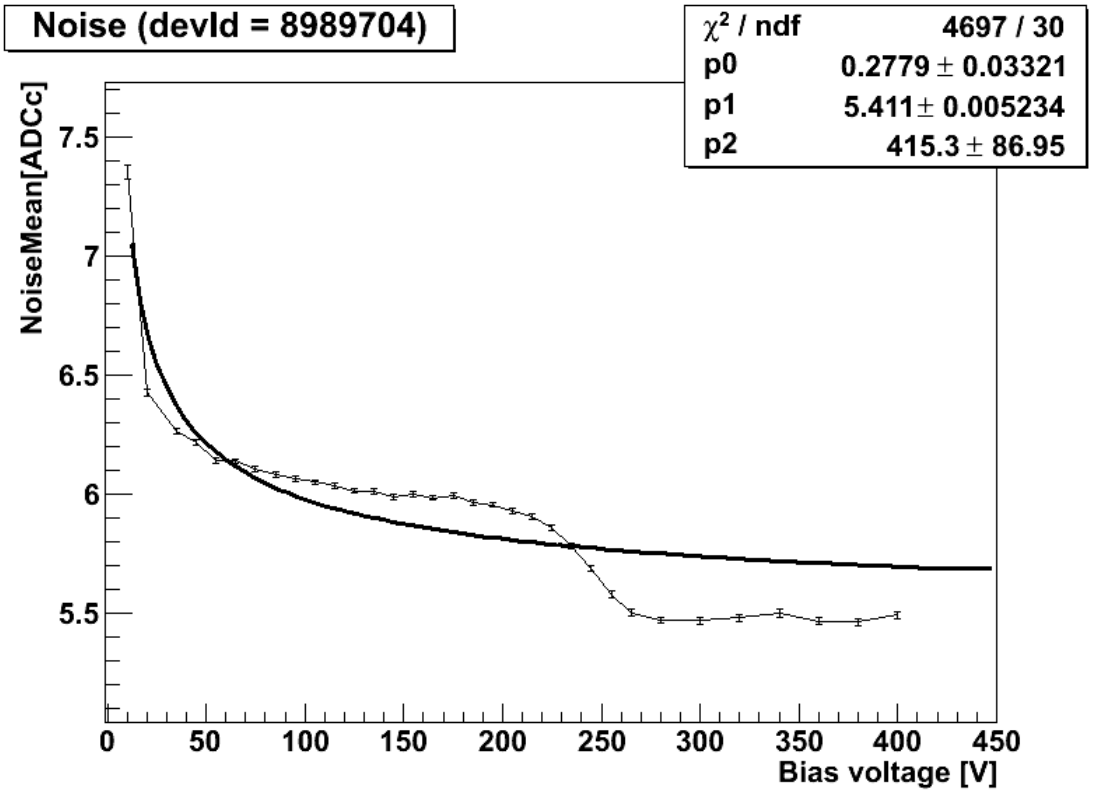

Figure 6.8: Average noise value versus applied bias voltage for an example APV in the TIB partition. The noise decreases in two steps which cannot be explained in the underlying model, thus the fit is failing to describe the behavior correctly.

property. After type inversion the depletion zone does not start around the strips, but from the backplane of the sensor. The consequence of this is that the important region around the p^+ implants is only depleted when the applied bias voltage equals or exceeds the full depletion voltage. This leads to a high inter strip capacitance and low inter strip resistance, and thus to high noise before full depletion. This has been studied for example in [LeCaCi]. This would lead to a pronounced kink in the noise versus bias voltage curve, which would make the identification of the full depletion voltage comparatively simple. Nevertheless, the fitting function needs to be adapted for this future scenario.

Another problem of the noise bias scan is that a number of modules are showing an unexpected behavior: the noise value is decreasing with $1/\sqrt{V_{bias}}$ and saturates eventually. Afterwards, however, it decreases again and saturates at a second level. This characteristics is primarily appearing in the inner layers of the barrel that are mounted with single sensor modules. An example evolution of the noise is shown in figure 6.8.

The reason for this characteristic is not yet understood. It is under investigation to identify under which circumstances the noise profile is having this shape. It can be

excluded that the sensors did already undergo type inversion. A possibility is that the simplified view, that the depletion zone starts around the strips before type inversion and from the backplane after type inversion, is not sufficiently accurate even for lightly irradiated sensors.

6.2 The Signal Bias Voltage Scan: An In-Situ Approach

A more accurate way to determine the full depletion voltage of the sensors in the running experiment is the analysis of the charge collection in dependency on the applied bias voltage. This procedure is called *signal bias scan*. The particle signal approach is similar to the noise bias scan, with respect to the variation of the applied bias voltage. One of the differences is that the signal scan takes data in an ordinary physics fill, and not in a special local run. The main benefit of a signal scan is its higher precision. The disadvantage of this approach is that beam time is needed for the measurement. In order to find a balance between minimizing the beam time loss and maximizing our understanding of the full depletion evolution, the tracker management has agreed to perform this type of measurement two times per year for the whole tracker, and once per month for a small selection of modules only (see table 6.1).

Partition	Side	Power Group
TIB	+	1.6.2.5
TOB	+	4.3.3.8
TEC	-	3.7.1.1.2
TEC	-	3.7.1.1.3
TIB	-	1.2.2.1

Table 6.1: List of power groups which are part of the small bias scan.

One criterion for the selection is a broad distribution in the z and the ϕ angle (see 3.3) to avoid overlaps and limit the impact on the tracking efficiency. Furthermore, it was important to probe different regions and partitions, while simultaneously keep the number of contributing power groups low.

6.2.1 Principles of the Signal Method

The amount of charge collected at each event depends on the amount of charge that is created by the traversing particle and the *charge collection factor* (CCF)

$$C_{coll} = C_{gen} \cdot CCF. \tag{6.9}$$

The CCF is also known as the charge collection efficiency because it is defined as the fraction of generated charge that is collected. However, with strong fields the collected

charge may exceed the initially generated charge due to charge multiplication. Thus, the expression charge collection factor is more universal.

The CCF strongly depends on the bias voltage. There are three main effects how the applied voltage influences the CCF:

The variation of the depletion zone width is undoubtedly the main effect. Only charge generated in the depleted region can by read out. The dependency of depletion width on the bias voltage is given in equation 6.2.

The variation of the mobility of charge carriers can also contribute significantly. Different E-field strength generated by the applied bias voltage lead to a modification of the mobility of the charge carriers. When the mobility becomes sufficiently low not all charge can be read out in the time frame of the read out. It is clear that this also depends on the width of the sensor and on the given read out mode that defines the time frame for the read out.

The change in capacitance of the sensor modifies the shaping of the APV by altering the raise time of the signal pulse. This causes the timing of the trigger to be suboptimal with respect to the signal, resulting in a reduced collected charge. In section 6.1.1 it was shown that the capacitance depends on the bias voltage.

We accounted for these three effects in a model that we use to generate template curves for the collected charge over the applied bias voltage. This family of curves is used later on to fit the measured data. The technical details of the model is described in the following subsection.

6.2.2 Modeling the Signal Strength Dependency on Bias Voltage

The time frame for the readout of the signal depends on the used readout mode. Each channel of the APV consists of a preamplifier and a shaping amplifier (shaper) which produces a 50 ns pulse shape. The shaper output is then sampled in a pipeline, from which it is read out by a circuit called *Analogue Pulse Shape Processor* (APSP). The APSP can operate in one of two readout modes: *peak* mode and *deconvolution* mode. In peak mode, only one sample per channel is read from the pipeline. In deconvolution mode, three samples are read sequentially and combined into one output using a weighted sum. The latter mode results in an alteration of the analogue pulse shape. The curve becomes way steeper, peaking at 25 ns, and returning rapidly to the baseline again. Details about the readout modes and their performance can be found in [RaCeFr]. In figure 6.9 the pulse shapes in peak and deconvolution mode are shown.

In this approach all relevant parameters (like the full depletion depletion voltage, the temperatures and module geometry) are assumed to be known. Based on these, the course of the collected charge versus bias voltage curve is modeled. The three effects mentioned in subsection 6.2.1 are discussed in the following.

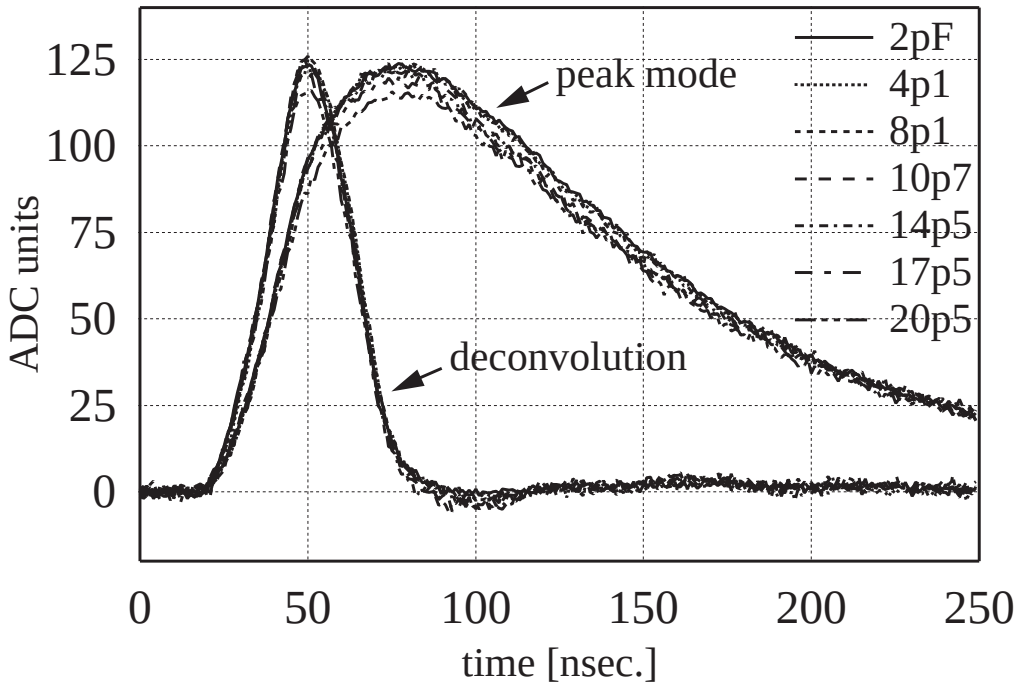

Figure 6.9: APV pulse shape in peak and deconvolution modes, for a range of input capacitance. The plot is taken from [RaCeFr].

The Variation of the Depletion Zone Width

The depletion zone width is modeled in analogy to 6.8:

$$W = \begin{cases} W_{depletion}\frac{V_{bias}}{V_{FD}} & V_{bias} < V_{FD} \\ W_{depletion} & V_{bias} \geq V_{FD} \end{cases} \tag{6.10}$$

The generated charge that is simulated is proportional to the depletion zone width. It is assumed to be distributed homogeneously within the depleted region. The absolute value of the generated charge is arbitrary. The plateau height is one of the two free fit parameters. The other one is the full depletion voltage. Only the relative change of the signal is of interest within this simulation.

The Variation of Drift Velocity

The drift velocity v_d is modeled using a parametrization described in [JaCaOt] :

$$v_d = v_m \frac{\mathcal{E}/E_c}{[(1 + (\mathcal{E}/E_c)^\beta]^{\frac{1}{\beta}}}, \tag{6.11}$$

for the electric field $\mathcal{E}$, and the empirically determined parameters v_m, E_c and β. The

values for these parameters are listed in table 6.2 in dependency of the temperature given in units of Kelvin.

	Electrons	Holes	Units
v_m	$1.53 \cdot 10^9 \cdot T^{-0.87}$	$1.62 \cdot 10^8 \cdot T^{-0.52}$	cm/s
E_c	$1.01 \cdot T^{1.55}$	$1.24 \cdot T^{1.58}$	V/cm
β	$2.57 \cdot 10^{-2} \cdot T^{0.66}$	$0.46 \cdot T^{0.17}$	-

Table 6.2: List of empirically determined parameters for the determination of drift velocity in dependency of the temperature and the electric field taken from [JaCaOt].

The temperature has been approximated to be 290 K. In figure 6.10 the impact of modified temperature assumptions on the resulting curves is shown. The outcome of this study suggests that the importance of creating model functions for the different temperature regimes is low since the overall alteration is below 1% per 10 °C.

The electric field is assumed to increase linearly in the following way:

$$\mathcal{E}(x) = \begin{cases} \frac{2V}{W}(1 - \frac{x}{W}) & V_{bias} < V_{FD} \\ \frac{2V_{FD}}{W_{depletion}}(1 - \frac{x}{W}) + \frac{V - V_{FD}}{W_{depletion}} & V_{bias} \geq V_{FD} \end{cases} \tag{6.12}$$

Based on this electric field and the corresponding mobilities, the charge carrier transport in the sensor bulk is simulated. This histogram contains the charge transported to the borders of the sensor in dependency on the time, using the initial charge distribution described in subsection 6.2.2.

Change of the APV Shaping Time

The capacitance per unit length of a sensor can be written as [BaCaVi]:

$$c = \epsilon_0 \epsilon_{Si} \frac{p}{W} \tag{6.13}$$

for the permittivities ϵ_0 and ϵ_{Si} (see table 6.3), the pitch p and the width of the depletion region W. For a given strip length l and potentially under-depleted sensors, this can be extended to:

$$\begin{aligned} C &= \epsilon_0 \epsilon_{Si} \frac{pl}{W_{depletion}} \sqrt{\frac{V_{depl}}{V_{bias}}} \text{ for } V_{bias} < V_{depl} \\ &= \epsilon_0 \epsilon_{Si} \frac{pl}{W_{depletion}} \text{ for } V_{bias} \geq V_{depl} \end{aligned} \tag{6.14}$$

The shift in the APV peak time has been estimated based on a simulation of the variation of the pulse shape with changing load capacitance values, performed by Mark

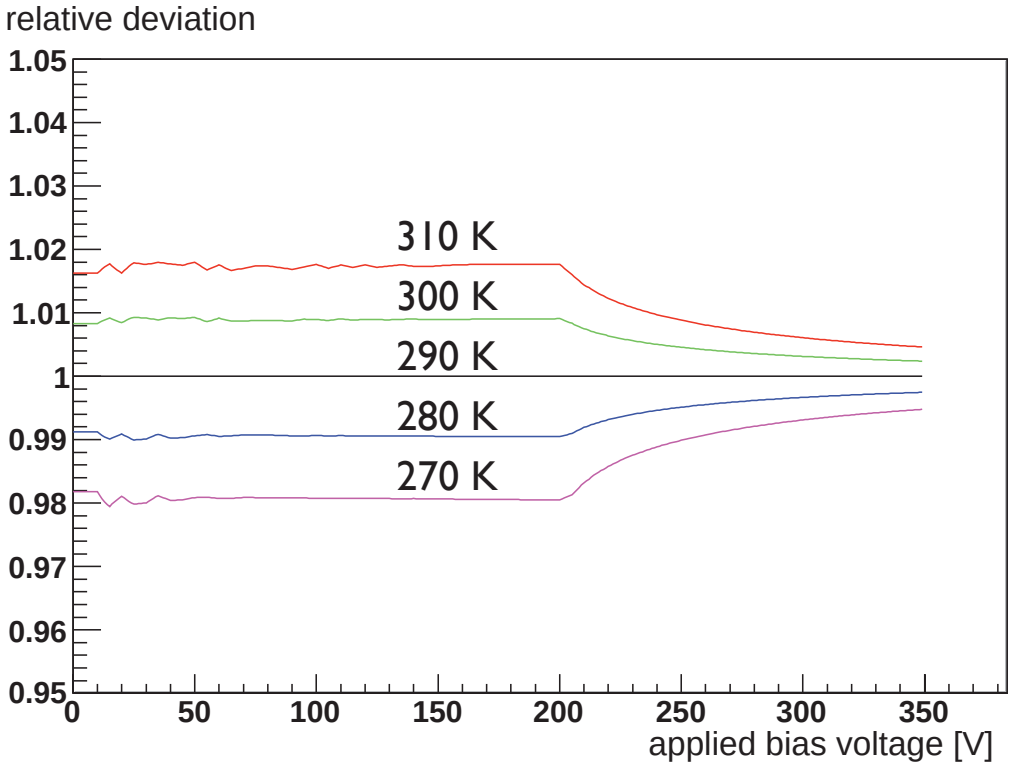

Figure 6.10: Relative deviation of the modeled signal curves based on different temperature assumptions versus the applied bias voltage [AgrFon].

Vacuum permittivity	ϵ_0	8.854 $^{pF}/_{m}$
Relative permittivity of Si at room temperature under 1 kHz	ϵ_{Si}	11.68

Table 6.3: Permittivity of Silicon.

Raymond. An example of the simulated pulse shapes for different load capacitance values is shown in figure 6.11.

The capacitance shift is in the order of 10 pF, mainly determined by the strip length. Even though the shift in the peak time $\Delta\tau$ is not strictly linear, it has been approximated, based on small ΔC values, to be

$$\Delta\tau(\Delta C) = 0.7\frac{ns}{pF}. \tag{6.15}$$

In order to assess the impact of the modified peaking time on the signal strength, another consideration is needed.

The pulse shaping in the APV of the tracker modules can be described in a simplified way: by a CR circuit followed by a RC circuit. The signal of the charge sensitive

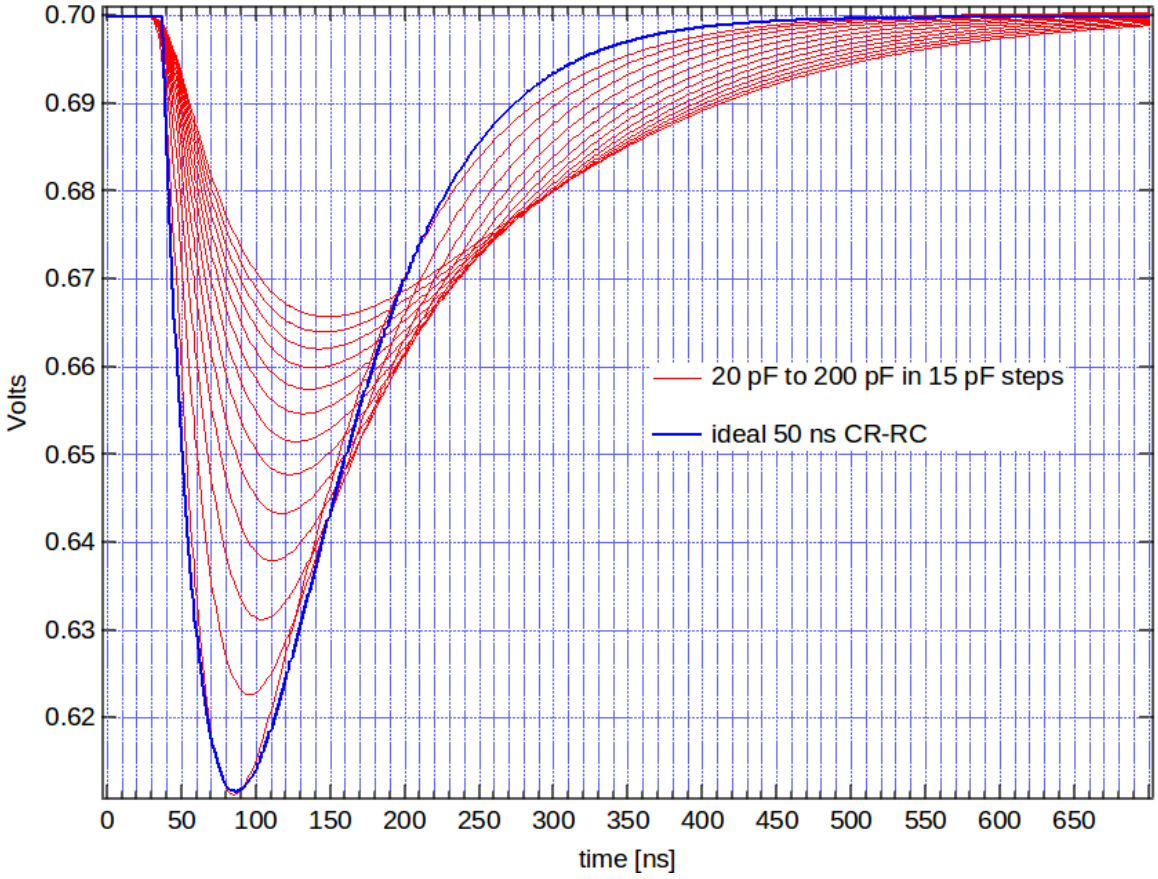

Figure 6.11: Simulated APV pulse shape dependency on the load capacitance for the TOB partition [Raymon].

preamplifier of the CMS tracker modules can be approximated with the Heaviside function

$$V_{in}(t) = \begin{cases} V_0 \text{ for } t > 0 \\ 0 \text{ for } t \leq 0 \end{cases} \tag{6.16}$$

with V_0 being proportional to the deposited charge in the sensor.

A convenient way of studying the response of a network is to use the Laplace transformations to switch into complex frequency domain (parametrized by s) of the different components. According to [Hiscoc] this leads to the following terms:

For the step function (compare equation 6.16), this leads to:

$$V(s) = \mathcal{L}[V(t)] = \frac{V_0}{s}. \tag{6.17}$$

For the CR circuit (high pass filter) the Laplace transformation is:

$$V_{out}(s) = \frac{\tau s}{1 + \tau s} V_{in}(s), \tag{6.18}$$

for $\tau = RC$ being the time constant of the CR circuit. For the RC circuit (low pass filter) the Laplace transformation is given by:

$$V_{out}(s) = \frac{1}{1 + \tau s} V_{in}(s), \tag{6.19}$$

assuming the same time constant as for the CR circuit. The equality of the two time constants is not necessarily given, but it is one of the aims to achieve the same time constants of 50 ns for well calibrated modules.

For the combined circuit this leads to

$$\begin{aligned} V_{out}(s) &= V_0 \cdot \frac{1}{s} \cdot \frac{\tau s}{1 + \tau s} \cdot \frac{1}{1 + \tau s} \\ &= V_0 \cdot \frac{\tau}{(1 + \tau s)^2}. \end{aligned} \tag{6.20}$$

If we perform a inverse Laplace transformation on equation 6.20, it yields the response in the time domain:

$$\mathcal{L}^{-1}[V_{out}(s)] = V_0 \cdot \frac{t}{\tau} \exp(-t/\tau). \tag{6.21}$$

The time constant of the circuit τ is called the shaping time. It is the time at which the maximum of the output pulse is reached.

One of the present research fields is to model the dependency of the APV response on a changed load capacitance in a non symmetric way ($\tau_{RC} \neq \tau_{CR}$).

In the scope of creating the template functions, the pulse shape is computed based on equation 6.21, with the shaping time τ altered by the capacitance induced shaping time shift, determined by equation 6.3 and 6.15.

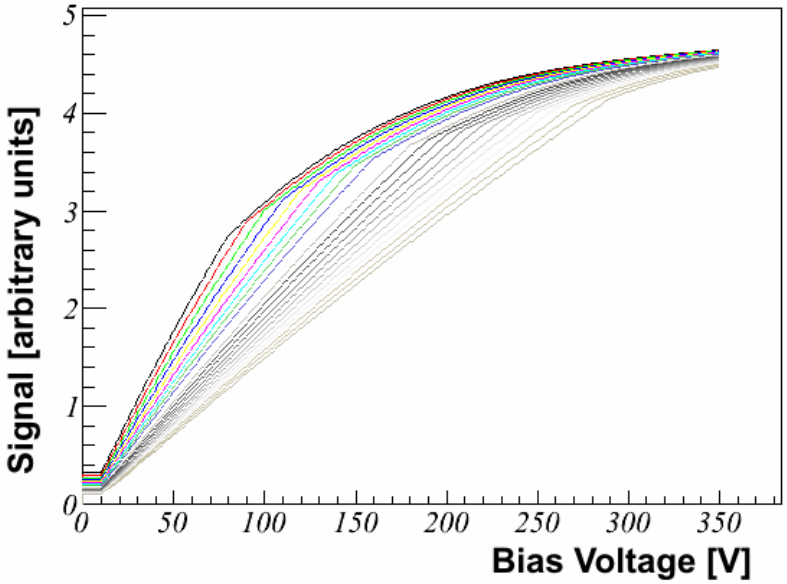

Figure 6.12: Simulated signal over bias voltage behavior for different full depletion voltages between 80 and 280 V. The kink corresponds to the full depletion voltage value of the corresponding curve.

Since the trigger is not dependent on the shaping of the APV, a modified shaping of a well-calibrated APV leads to a reduction of signal strength.

In figure 6.12 an example of the generated curves is shown for different bias voltage settings.

6.2.3 Analysis of the Signal Method

The first step of the analysis of the signal strength over bias voltage is a fit of the collected charge distribution for each sensor at each bias voltage setting. The distribution of the charge is a Landau distribution (compare section 2.1.5) smeared with a Gaussian in order to account for a finite accuracy of the detector.

It turned out, however, that a Landau fit of the distribution is comparably precise, while containing less variables. In figure 6.13 an example fit of the collected charge is shown.

The *most probable value* (MPV) and the sigma of all fits from one sensor is stored and put into a second graph, with the bias voltage setting being the x-axis. This graph is fitted with the family of curves created previously, as described in section 6.2.2. An example of this graph is shown in figure 6.14.

The full depletion voltage of the sensor is directly taken out of the fit, as one of the two free parameters.

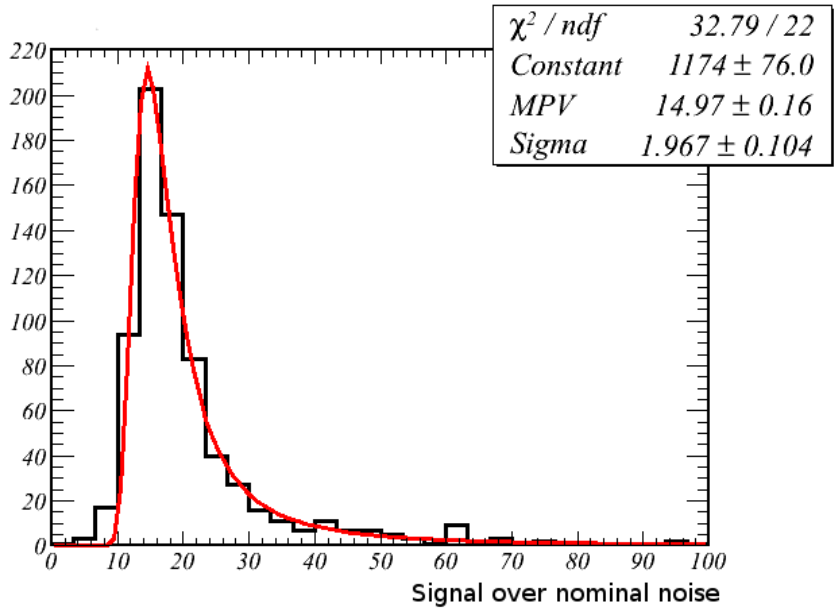

Figure 6.13: Example fit of the collected signal strength divided by the nominal noise value at the operational bias voltage setting. The red curve shows a Landau fit of the distribution.

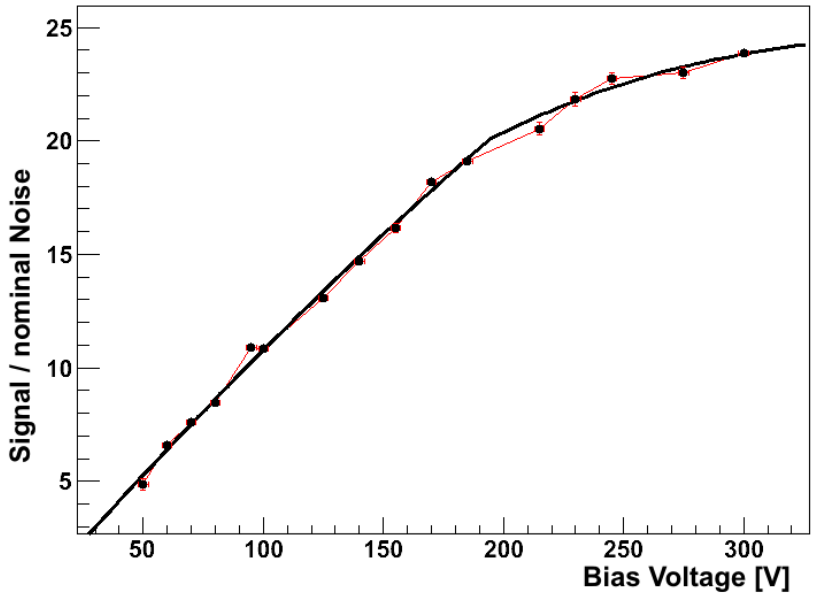

Figure 6.14: The most probable value of the signal strength is plotted versus the applied bias voltage. The graph is fitted with the family of curves generated in advance for various bias voltage settings. In this example the full depletion voltage is about 190 V.

6.2.4 Performance of the Signal Method

Similar to the noise approach, the improvement of the analysis procedures for the signal method is an ongoing effort. The fit functions are using detailed information about the sensors and the underlaying physics. This made it possible to get well suited functions with only two free parameters: the absolute signal height of the plateau and the full depletion voltage. However, this elaborate approach also bears a risk: the model needs to account for all underlying physics processes and their evolution with radiation. The change of the electric field distribution within the sensor with increasing irradiation is only one example of the challenging tasks.

6.3 Cross Validation Between the Different Approaches

An important assessment of the measurement's quality is its comparison with results obtained by other measurements. For this purpose we have three different approaches to compare:

The C-V measurement performed during production of the tracker.

The signal bias scan results.

The noise bias scan results.

A correlation plot between the results of an early signal bias scan and the C-V measurements is depicted in figure 6.15 for the TIB partition of the strip tracker.

The deviation between the two measurements is illustrated in figure 6.16.

Since the signal measurement was performed in the early stage of the CMS operations, we do not expect any deviation from the initial full depletion voltage values. Nevertheless, an offset is visible in figure 6.16. Additionally, the distribution is not strictly Gaussian. These two effects can be attributed to the systematic differences between the two approaches. Despite partial disagreement, the overall accordance shows that both techniques are viable to measure the full depletion voltage values.

The correlation between the noise bias scan approach and the signal scans values or C-V results respectively are shown in figure 6.17. Both in-situ bias voltage scans have been performed in early 2010, when the full depletion voltage is expected to match the initial full depletion voltage. It has to be noted that in the depicted TOB partition the modules are mounted with two sensors. Even though sensors with similar full depletion voltage values have been chosen to be mounted on each module, the full depletion voltage values differ to a certain extend. The C-V values in the plot are the average values of both full depletion voltage measurement results. It is clearly visible that the noise approach fails to determine the full depletion voltage reliably in the high depletion voltage regime. The reason for this mismatch is the difficulty to distinguish

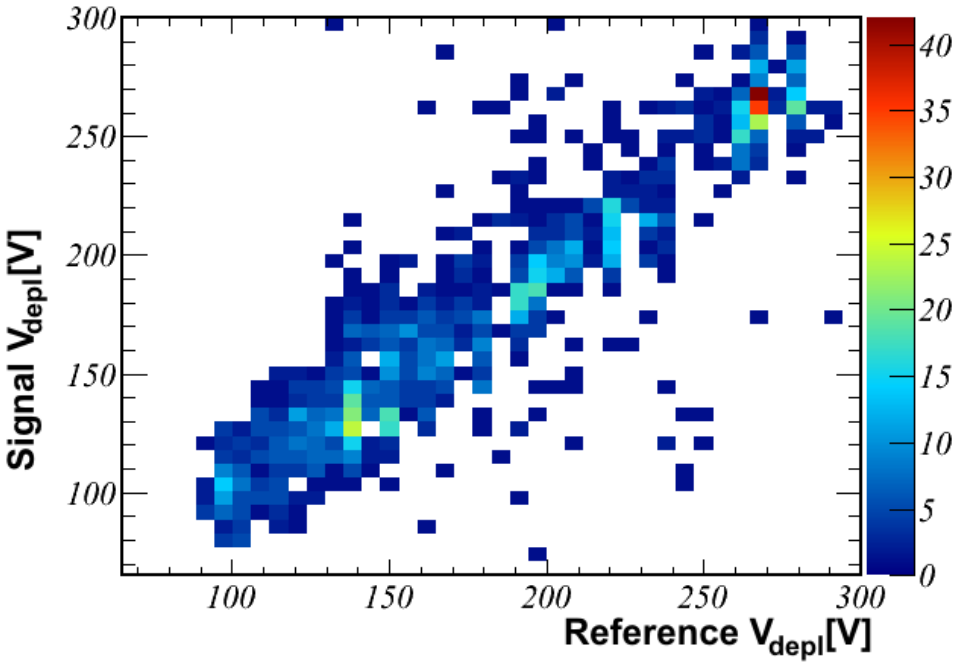

Figure 6.15: Correlation plot of the full depletion voltage values determined with the signal bias scan (y-axis) versus the corresponding results obtained by the C-V measurements (x-axis). The color code indicates the density of entries in the given bin. The dataset shows the results for the inner barrel of the silicon tracker.

between the $\frac{1}{\sqrt{V}}$ and the constant slope via the fit at high voltage values, as stated before in section 6.1.3.

Despite all deviations and inaccuracies, it can be stated that both developed in-situ methods are capable to determine the full depletion voltage values of the sensors.

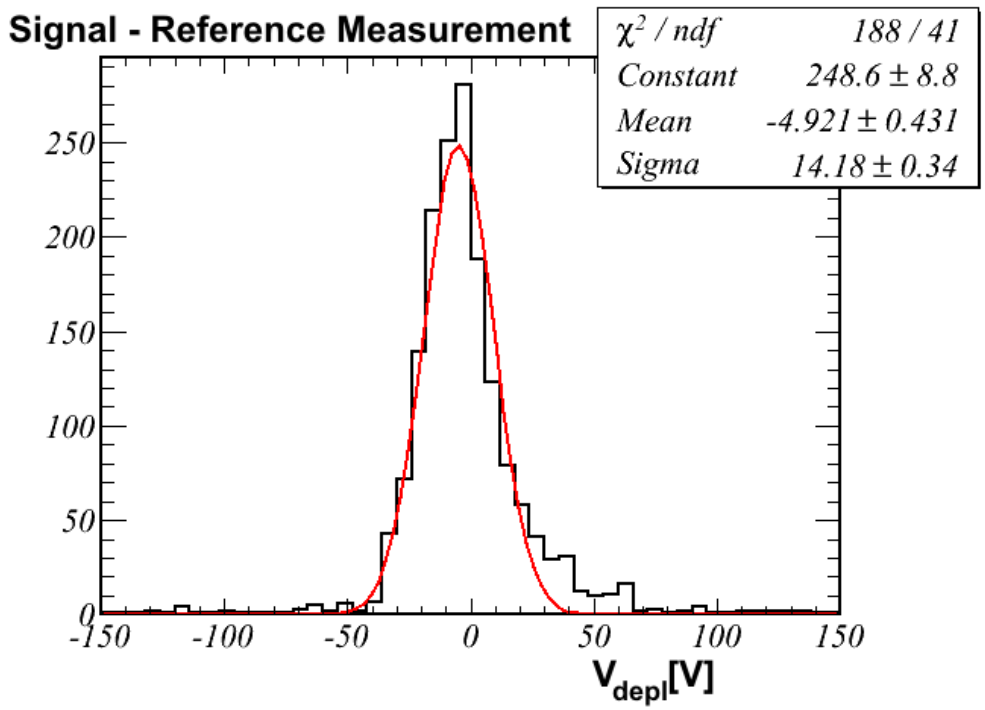

Figure 6.16: Deviation between the full depletion voltage values measured with the signal approach (after the sensors are built into the detector) and the corresponding value of the C-V measurement (performed during the production phase of the tracker).

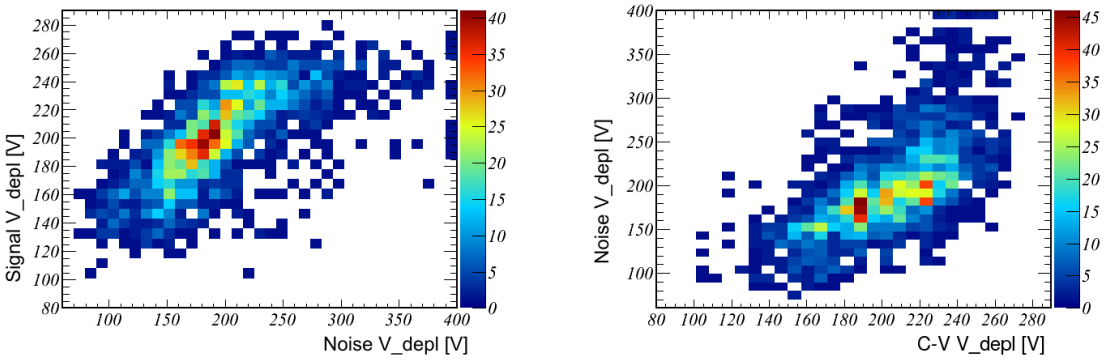

(a) Correlation between the full depletion voltage values obtained by the signal bias scan and the noise bias scan

(b) Correlation between the full depletion voltage values obtained by the noise bias scan and the average C-V measurements of the two sensors mounted on each module

Figure 6.17: Correlation plots of the full depletion voltage values obtained by the noise bias scan with the signal method results and the C-V measurements for the TOB partition of the strip tracker. Signal and noise bias scans have been performed in early 2010 when no change in full depletion voltage with respect to the initial values is expected.

Chapter 7

Estimation of the Detector Properties Evolution

All the relevant knowledge of the sensor properties and their dependency on radiation, temperature and time are put into a model to estimate the future evolution of these characteristics. The model scripts are programmed within the *ROOT* framework, which is based on the programming language C++. The framework was developed at CERN in 1995 and is continuously improved and maintained since then. It is widely used for data analysis, especially in high energy physics [ROOT].

7.1 Basic Principles of the Tool

The core purpose of the tool is to calculate the evolution of detector properties, given a specific radiation damage model, fluence exposure and temperature scenario. Important features of the tool are its ability to account for simultaneous annealing and radiation processes, as well as the possibility to assess the temperature increase due to heightened leakage currents by a thermal contact. In figure 7.1 an example of the input data sets for a radiation damage simulation is shown: the fluence exposure and the temperatures on a day by day basis.

For the full depletion voltage the Hamburg model presented in [Moll] was used, using slightly adjusted parameters determined during the quality assurance phase of the tracker production in [Dierla]. In table 7.1 an overview of the strip specific parameters is given using the nomenclature of the parameters introduced in section 2.2.3.

For the leakage current the parametrization according to 2.61 was used.

In order to account for the difference between a strip sensor and a p-n-junction a correction of the full depletion voltage according to 2.30 has been performed. For the sensors in the barrel region this is straightforward, while for the sensors in the discs and end caps the pitch of the strips is not constant due to the trapezoid shape. For the

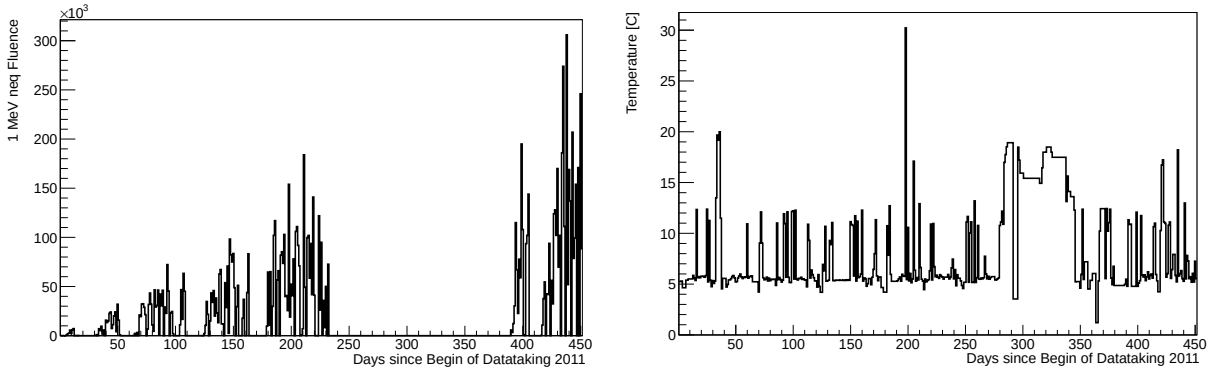

(a) Fluence profile used for simulation (b) Temperature profile used for simulation

Figure 7.1: Fluence and temperature profile used to simulate the evolution of leakage currents. Between day 240 and 380 the fluence exposure (a) was negligible. This corresponds, at first, to a heavy-ion collision period followed by a year end technical stop. During the technical stop the cooling plant was partially switched off, as it is visible in heightened temperatures in plot (b).

Parameter	320 μm sensors	500 μm sensors
g_c	$1.49 \cdot 10^{-2} \frac{1}{cm}$	$1.6 \cdot 10^{-2} \frac{1}{cm}$
r_c	0.9	0.9
c	$10.9 \cdot 10^{-2} \frac{1}{N_0 \ cm}$	$10.9 \cdot 10^{-2} \frac{1}{N_0 \ cm}$
g_a	$1.81 \cdot 10^{-2} \frac{1}{cm}$	$1.81 \cdot 10^{-2} \frac{1}{cm}$
g_Y	$5.16 \cdot 10^{-2} \frac{1}{cm}$	$5.16 \cdot 10^{-2} \frac{1}{cm}$

Table 7.1: List of strip specific Hamburg model parameters derived from [Dierla].

latter modules the average pitch has been taken for the correction. The pitch values of the CMS tracker sensors are listed in table 7.2.

For the luminosity the Fluka simulations (introduced in section 4.1) are used. The fluence values are computed for a grid of points covering the whole tracker region with 2.5 cm distance in r 2.5 cm in z direction. In addition, the simulations assume perfect ϕ symmetry. In order to obtain a fluence value for a given position of a module, a linear interpolation between the next grid points is performed.

The choice of the input data of the luminosity depends on the given type of calculation. For past periods the measured data (see section 4.2) is used, whereas for future periods the luminosity profiles are based on the expectations from LHC experts (e.g. [Zimmer]). The standard modus operandi of the tool uses one computational unit per day. However, this can easily be adjusted to a higher granularity if needed for the future. Thus, the luminosity and temperature values used so far are averaged per day.

Partition	Layer	Ring	Pitch
TIB	1,2	-	80 μm
TIB	3,4	-	120 μm
TOB	1,2,3,4	-	183 μm
TOB	5,6	-	122 μm
TID	-	1,2,3	97 - 143 μm
TEC	-	1,2,3	96 - 143 μm
TEC	-	4,5,6,7	143 - 183 μm

Table 7.2: List of the pitch values of the silicon strip sensors within the CMS tracker.

7.2 The Temperature Data

The assessment of the appropriate temperature data is a little bit more effort than the assessment of the luminosity. For scenarios in the past, the measured temperature data can be used. For projections into the future, a handle on the temperature evolution with increasing leakage currents is needed. To this effect, we determined the thermal contact between the modules and the cooling system. Details about the temperature data used is presented in the following sections.

7.2.1 The Measured Temperature Data

There are two independent temperature measurements within the CMS strip tracker:

Hardwired sensors read out via a *Programmable Logic Controller* (PLC) system, providing continuous measurements. There are three different general locations where the temperature probes are situated: on the like cooling pipes, in the air and on the silicon sensors. The different tracker partitions use different approaches for the thermal monitoring as it is shown in table 7.3.

DCU temperature measurements (compare section 5.1.2) are only read out during data taking, but provide several measurements per module.

Partition	T probes at the silicon	T probes at the cooling pipe	T probes in the air
TIB	no	yes	no
TID	no	yes	no
TOB	no	yes	yes
TEC	yes	no	yes

Table 7.3: List of the PLC temperature probe position types in the tracker.

Two different approaches are used to create reasonable temperature datasets for past periods:

In case all modules are part of the calculation the average temperatures for the different operational states (ON,OFF,STANDBY) are computed. The temperatures used for the simulation are then defined by the dominant state of each respective day.

If a detailed investigation of only few modules is performed, the complete temperature history is taken into account on a day by day basis. In case of enabled data acquisition, the average temperature values measured from the DCUs are taken. When the tracker is off, the temperature is assumed to be equalized. Thus, the average temperature values provided by the PLCs are used. If the tracker is ON or in STANDBY and no DCU data is recorded, the PLC data is used together with a specific offset. The offset is determined by the average temperature difference between the DCU measurements and the PLC measurements for the respective states.

The implementation of this logic has been performed with the supervised CERN summer student Philipp Löschl.

7.2.2 The Thermal Contacts

For long term projections it is important to estimate the impact of an increase in leakage current on the temperature of the sensor. This is essential since an increase in leakage current will raise the temperature of the sensor through additional power load and a finite thermal contact to the cooling system. In addition, an increase in temperature leads to higher leakage current values (compare equation 2.39). Due to this self enforcing effect, it is possible that the thermal contact as well as the cooling itself wonÂ´t be able to keep the temperature at a constant level at high leakage currents. In this case, the temperature increases further and further until the limitations of the power supply system are reached. This phenomenon is called *thermal runaway*. A schematic draft of the power-temperature dependency is depicted in figure 7.2.

A dedicated measurement has been performed in 2011 to estimate the thermal contacts of the tracker modules. In the scope of the measurement, the VPSP setting ([BaBaHa]) of the APV has been modified, leading to an altered baseline voltage and thus to a change in the power load of the readout electronic. During the variation of the power the temperature change of the hybrid has been measured resulting in a $\frac{dT}{dP}$ dependency, which is assumed to be constant. The results determine the thermal contact between each modules readout electronic and the cooling system. As a first step we used these values as an approximation of the modules thermal contact between the sensor and the cooling system.

In the VPSP scan temperature differences of up to 6 K have been achieved. The distribution of the thermal contacts obtained via the measurement is shown in figure 7.3.

The question whether a module is near to a thermal runaway, can be calculated. At

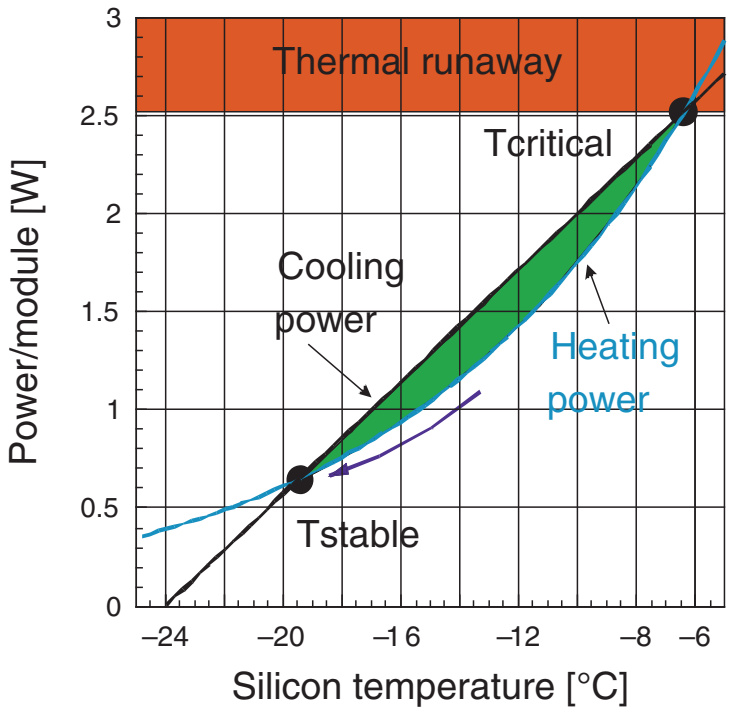

Figure 7.2: Example of the power-temperature dependency of a module. The straight black line indicates the cooling power given by the cooling plant and the thermal contact between the module and the cooling system. This linear curve corresponds to a constant thermal contact. The bended blue curve shows how the power load depends on the module temperature. At the critical temperature the power increase per temperature surpasses the capabilities of the cooling system, resulting in a thermal runaway. The figure is taken from [Hartma].

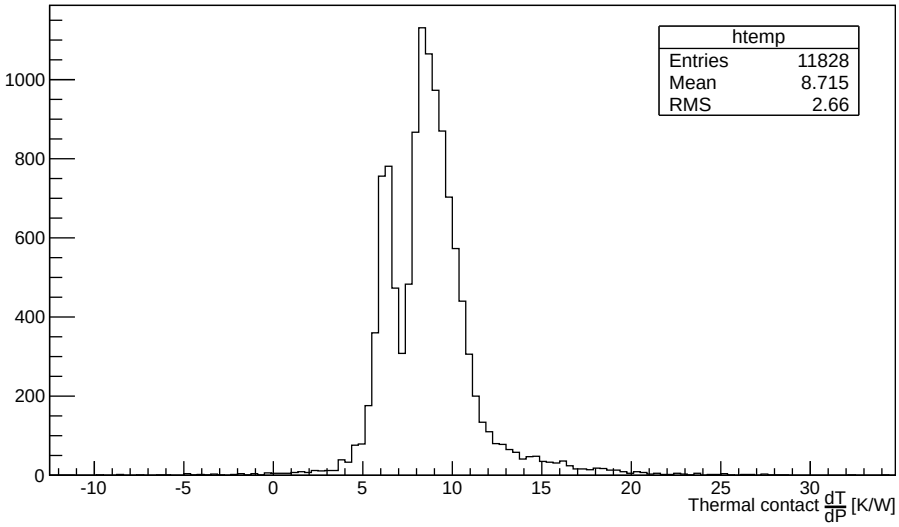

Figure 7.3: Distribution of the thermal contacts between the hybrid and the cooling system of the tracker modules. The results have been obtained by modifying the power applied to the hybrids (by VPSP settings) and measureing simultaneously the temperature change.

a given operational point in the power-temperature plane ($(V_{bias} \cdot I_0, T_0)$) the heating power increases in the following way with the temperature T (see equation 2.39):

$$P = V_{bias} \cdot I_{leak} = V_{bias} \cdot I_0 \frac{T^2}{T_0^2} \exp\left(\frac{-1.21eV}{2k_B}(\frac{1}{T} - \frac{1}{T_0})\right), \tag{7.1}$$

for k_B being the Boltzmann constant. The thermal contact defines the differential dependency $\frac{dP}{dT}$ that leads to:

$$P(T) = \frac{dP}{dT}(T - T_0) + I_0 V_{bias}, \tag{7.2}$$

for an operational temperature T, initial temperature T_0 and leakage current I_0. If we search for the zero values of the following function

$$\left[\frac{dP}{dT}(T - T_0) + I_0 V_{bias}\right] - \left[V_{bias} \cdot I_0 \frac{T^2}{T_0^2} \exp\left(-\frac{1.21}{2k_B}(1/T - 1/T_0)\right)\right], \tag{7.3}$$

we obtain per definition the zero value $T = T_0$. However, the function may have another zero value, which defines T_{crit}. The thermal distance $T_{crit} - T_0$ gives an estimate on how close a module is to the critical point of a thermal runaway. It depends on the operational temperature T_0 and on the collected radiation damage via I_0.

7.3 Comparison Between Simulated and Measured Data

One of the most important aspects of the radiation damage study is the validation of the used radiation damage models with the measured data. In section 5.2.5 it has been shown that the predictions of the particle flux, based on the CMS luminosity measurements and the Fluka simulations, deliver reasonable estimates of the 1 MeV neq fluence for the tracker. The next step in the validation process is to include the full simulation of simultaneous irradiation and annealing and compare it to the respective measurements. A discussion of the validation processes and the measured radiation damage in CMS will be published in [Barth2].

7.3.1 Comparison Between Simulated and Measured Leakage Current

For the leakage current there are primarily two types of plots assessing the quality of the simulation:

A scatter plot of the simulated versus the measured leakage current for a high statistic sample at certain points in time.

An overlay of the simulated and measured leakage current values in time for selected modules.

For the first part, the simulation was launched on all modules with reliable DCU readout of the temperature and the leakage current and with the thermal contact being in a reasonable range ($0 < \frac{dT}{dP} < 30\frac{K}{W}$ see figure 7.3).

In figure 7.4, 7.5 and 7.6 the simulated leakage current versus the measured DCU leakage current for several integrated luminosity values are shown. For each scatter plot a histogram of the relative deviation between simulation and measurement is depicted.

There are several reasons for uncertainties and fluctuations in these plots. At first, the granularity of the computation does not allow for multiple tracker states and temperatures on a single day. In addition, the temperature is only derived from an average value with the given dominant tracker state of the respective day and does not describe potential long term movements. All these uncertainties are valid for all integrated luminosity values, thus if we neglect the impact of the initial leak-

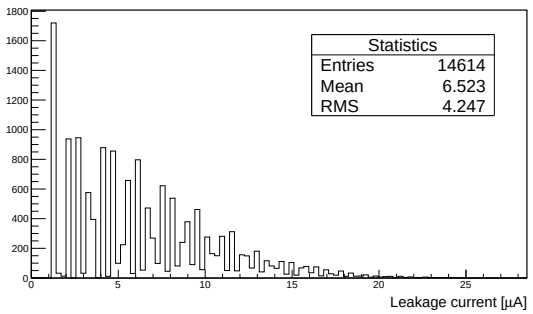

Figure 7.7: Early 2011 leakage currents, used for initial simulation values.

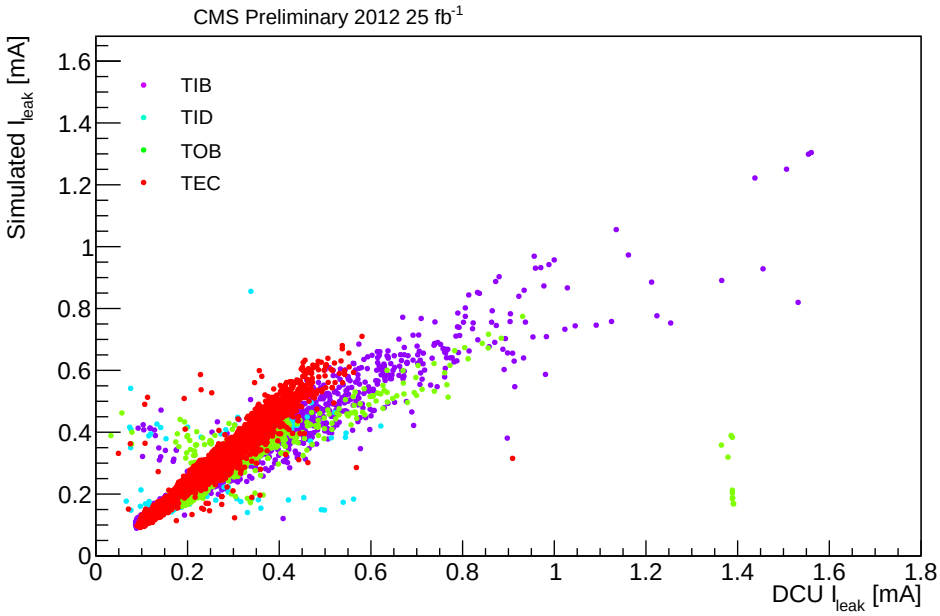

Figure 7.4: Simulated leakage current versus DCU measurements for a high statistic sample for 25 fb^{-1} of integrated luminosity. Each point in the scatter plots corresponds to one module in the tracker, while the different colors indicate the corresponding partition.

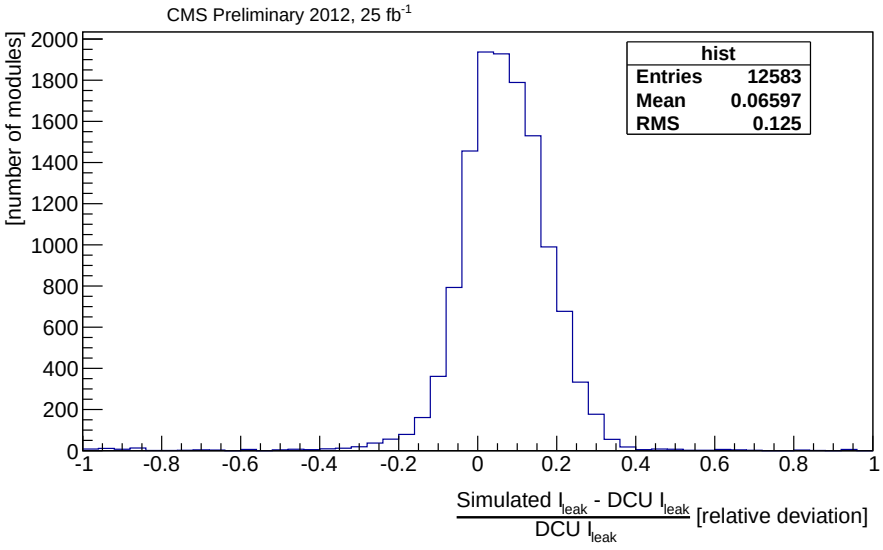

Figure 7.5: Relative deviation between simulated and measured $I_{leakage}$ after an integrated luminosity of 25 fb^{-1}.

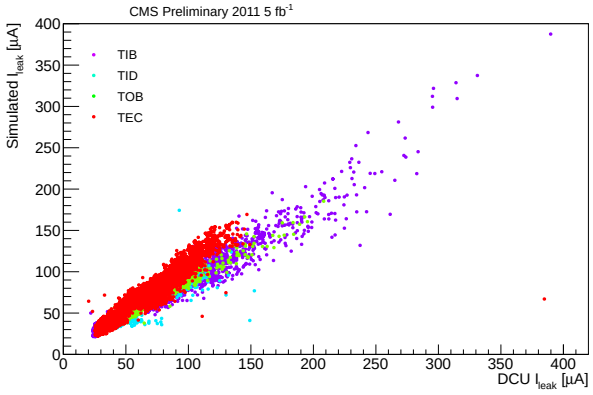

(a) Simulated vs. measured $I_{leakage}$ after 5 fb^{-1}

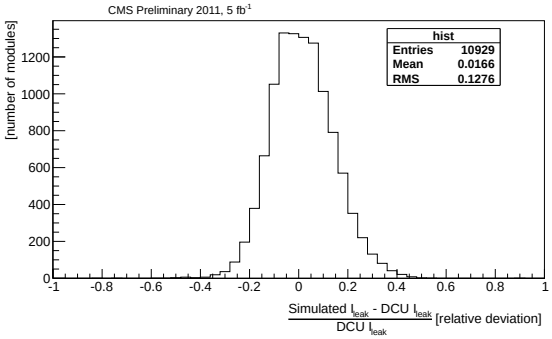

(b) Relative deviation between simulated and measured $I_{leakage}$ after 5 fb^{-1}

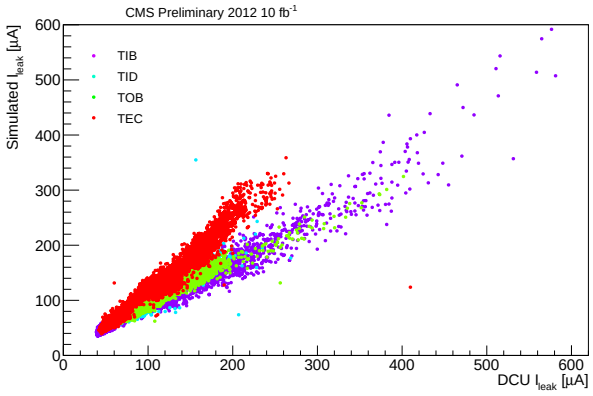

(c) Simulated vs. measured $I_{leakage}$ after 10 fb^{-1}

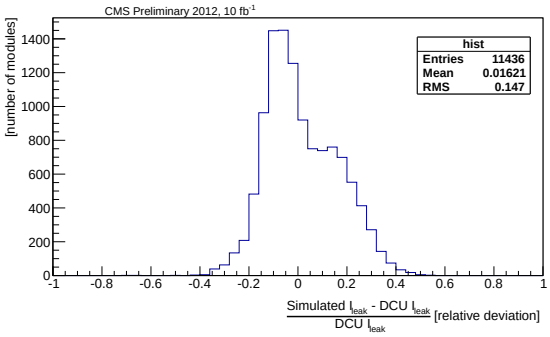

(d) Relative deviation between simulated and measured $I_{leakage}$ after 10 fb^{-1}

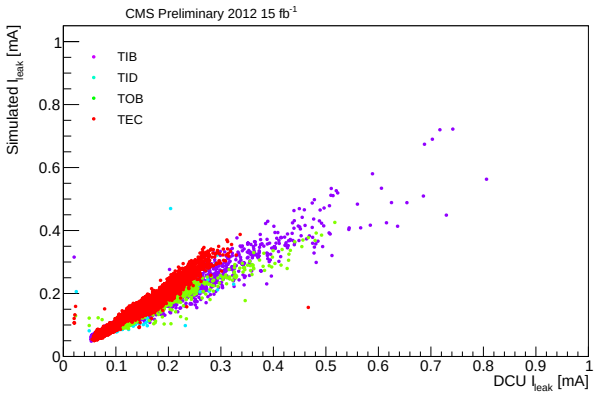

(e) Simulated vs. measured $I_{leakage}$ after 15 fb^{-1}

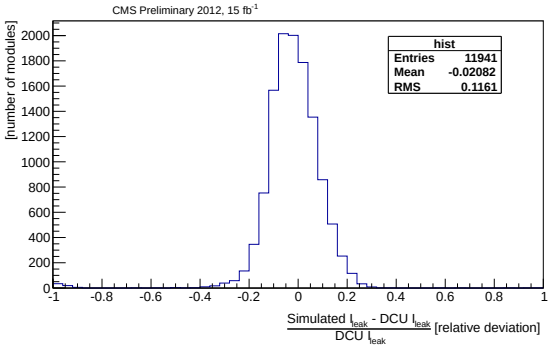

(f) Relative deviation between simulated and measured $I_{leakage}$ after 15 fb^{-1}

Figure 7.6: Simulated leakage current versus DCU measurements for a high statistic sample for different integrated luminosity values (5 fb^{-1}, 10 fb^{-1} and 15 fb^{-1}). Each point in the scatter plots corresponds to one module in the tracker, while the different colors indicate the corresponding partition. For each luminosity the right hand side plot shows a histogram of the relative deviation between the simulation and the DCU values of the leakage current.

age current (its relative significance drops with higher currents), we expect the relative deviation to be more or less constant. The leakage current at the beginning of 2011 operations is used as initial value for the simulation. The magnitude of the values is in the order of μA, the distribution is shown in figure 7.7.

The relative deviations for the four above mentioned snapshots are all well below 10%. A clear trend is not visible, thus it is compatible with random fluctuations. However, especially for 10 fb^{-1} we have a high discrepancy in the distribution with respect to the expected Gaussian. While for 5, 15 and 25 fb^{-1} the measurement is taken in the mid or even late running of the respective year, the 10 fb^{-1} plot corresponds to early 2012 operations, two month after the winter shutdown. This circumstance is making the relative share of pure annealing periods way more pronounced than in the three remaining cases.

In figure 7.8 the evolution of simulated and measured leakage current values over time is depicted, starting from 2011 operations until mid 2012. Even though both the leakage current and the temperature data (and thus the simulated leakage current) is distorted with high fluctuations, it is visible that the overall trend of the current measurement is described by the simulation.

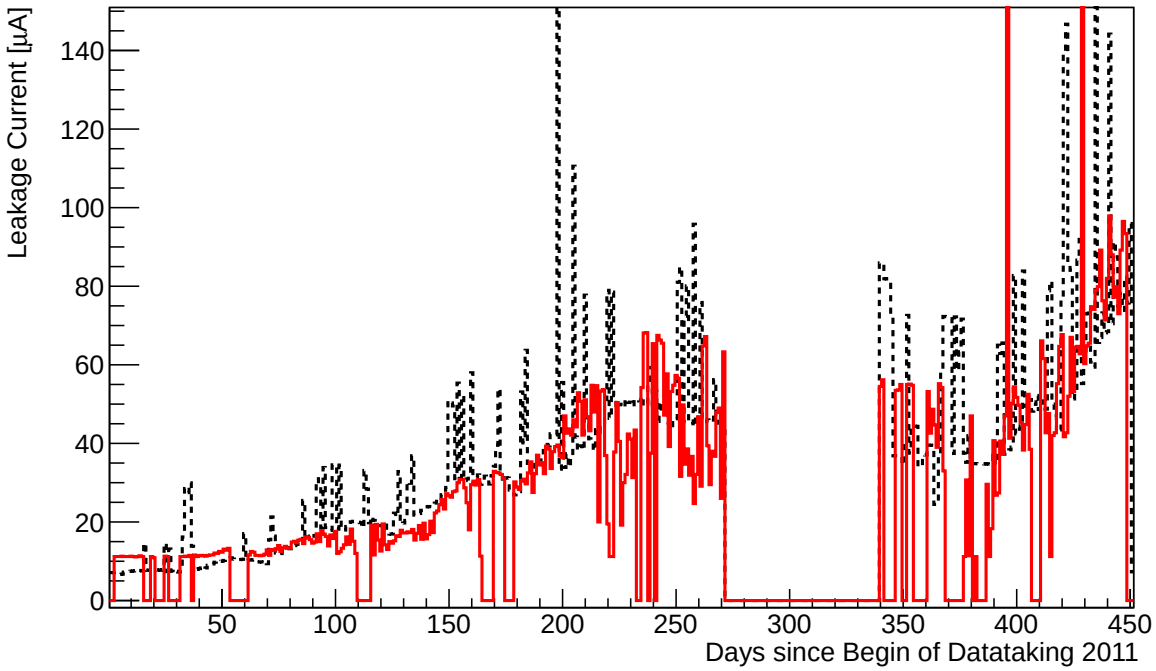

Figure 7.8: Simulated and measured leakage current evolution over time. The red line represents the DCU leakage current measurements, while the black dashed line represents the simulation.

The temperature and fluence profiles used for the simulation shown in figure 7.8 is drawn in figure 7.1.

7.3.2 Comparison Between Simulated and Measured Full Depletion Voltage

With the given accuracy of the full depletion measurement techniques used at the CMS tracker, no comparison between the simulation and measurement is possible. However, we shared our code with the CMS pixel community in order to validate the tool. In the pixel sub detector significant changes in the full depletion voltage are visible due to the more intense fluence exposure (about one order of magnitude higher).

Some modifications to the underlying model have been implemented by Seth Zenz. Firstly, the pitch correction was omitted so that the model describes a plain p-n junction. In order to account for the oxygenated silicon bulk used for the pixel sensors, a different set of parameters was used. The parameters have been derived from [LiWaLe]. The main difference is an unequal impact of charged and neutral radiation.

For determining the full depletion voltage the pixel community uses a slightly different approach: they compute the hit efficiency while scanning through the bias voltage regime of interest. Instead of searching for the exact full depletion voltage, a more pragmatic approach is chosen. At the point where the hit efficiency reaches 99%, the sensor is considered to be be fully depleted; this point is called effective full depletion voltage. Though this is an approximation, the strong dependency of the hit efficiency on the depletion of the sensor (as it will be shown in section 9.2) justifies this approach.

In figure 7.9 a comparison plot is shown between the model predictions of the full depletion voltage evolution (based on the measured luminosity and temperatures using the Fluka simulations to translate the luminosity into the 1 MeV neq particle fluence) and the measured effective full depletion voltage during 2011 and 2012.

It is visible that the actual change in full depletion voltage drags behind the model prediction. Nevertheless, the overall shape is similar. The measurements indicate that the type-inversion for the pixel layer 1 happened between the end of 2011 and early 2012. For real sensors it is not expected that the full depletion voltage becomes zero. Investigations of the LHCb collaboration show, for example, that the finite value at type inversion is around 20 V [Moran].

Based on this comparison, it is difficult to give a conclusive statement concerning the credibility of the model for the full depletion voltage evolution in CMS. Mainly because the effective full depletion voltage is not necessarily the same as the full depletion voltage. In addition, comparisons of the leakage current show that the Fluka simulation in the region of the pixel is less reliable than for the microstrip region [BarZen].

For the radiation levels after the long shutdown of 2013 and 2014 it will be an interesting task to elaborate on the comparison between the model predictions and the measured full depletion voltage changes of the silicon strip tracker.

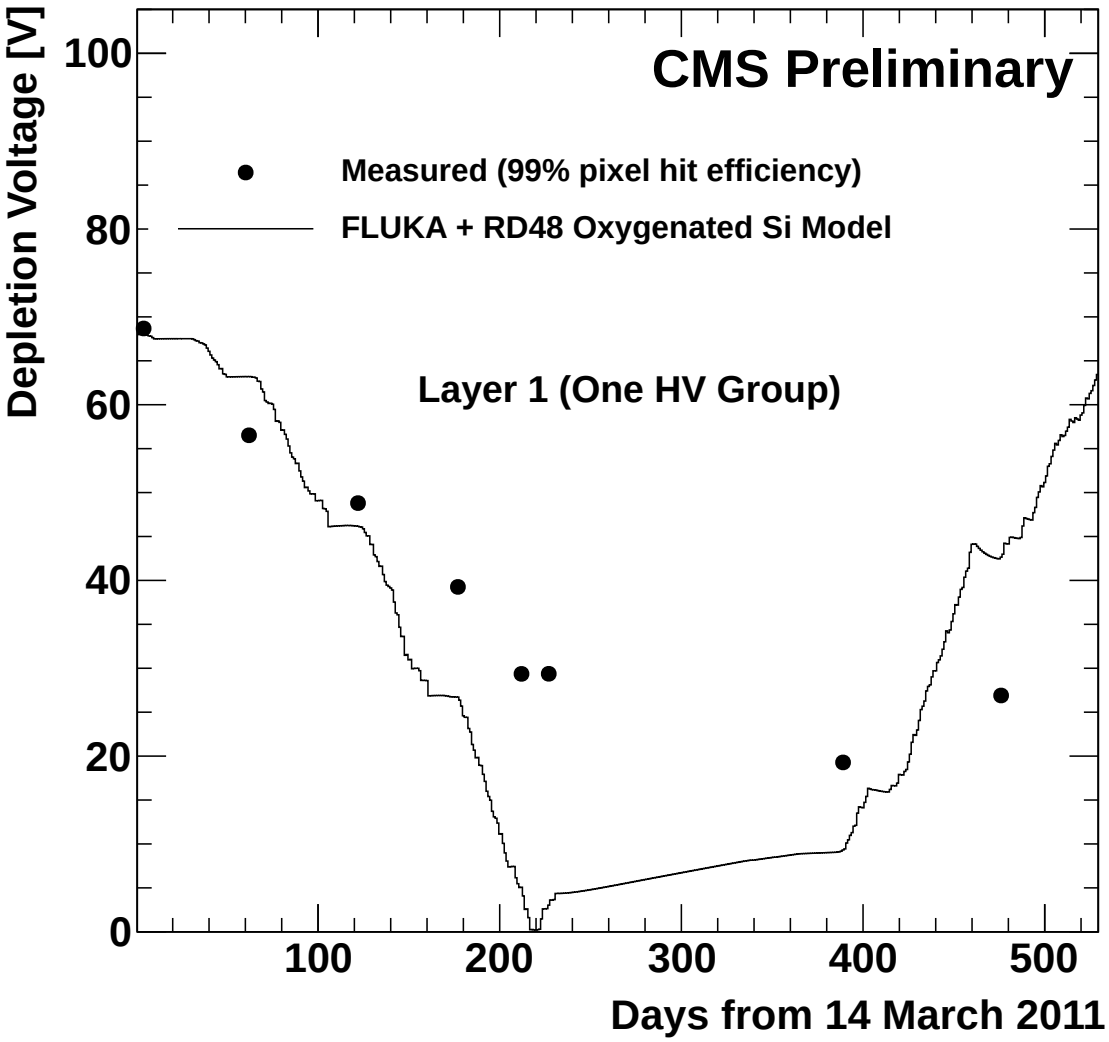

Figure 7.9: Comparison between the measured evolution of the full depletion voltage of the first pixel layer and the model predictions. The measured effective full depletion voltage points are derived from hit efficiency scans at 99% efficiency. The simulation is based on a model for oxygenated silicon described in [LiWaLe].

Chapter 8

Predictions for Detector Properties

To predict the evolution of a property is always a delicate matter. Nevertheless, it is vital for the tracker community to estimate the future developments of the relevant quantities and to assess the impact of modifications of the temperature scenario. The simulations do not leave any doubt that the cooling of the CMS tracker needs to be improved in order to be operational at the expected luminosity after the long shutdown in 2013 and 2014.

In figure 8.1 a map of the tracker modules is shown for an integrated luminosity of 200 fb^{-1} under the assumption that the cooling plant continues to run with the same settings as in 2012. Even though the tracker was built to endure at least 500 fb^{-1} of integrated luminosity, a huge part of the modules would exceed the critical 4 mA of leakage current already at 200 fb^{-1}.

It was mentioned before that the shielding of some support lines of the tracker from humid air is a crucial task for LS1 (see section 5.2.2). Thus, a lot of effort is put into an adequate sealing. Nevertheless, there is a small number of modules which have either lost their cooling contacts or are cooled by cooling lines that have been closed due to increased leak rates of the cooling liquid. For any of these, it is not clear whether it will be possible to keep them at reasonable low temperatures during the LHC operations of the next years. The modules at risk are collected in a dedicated list. It has 674 entries which is less than 5% of the tracker modules. The potential impact on the tracking efficiency due to a loss of these modules is investigated in section 9.3.

In the following sections predictions for the future evolution of the leakage current and the full depletion voltage are presented for different cooling scenarios. In all cases, it is assumed that a change of the cooling set point translates one-to-one into a change of the individual sensor temperatures. A list of the considered scenarios is presented in table 8.1.

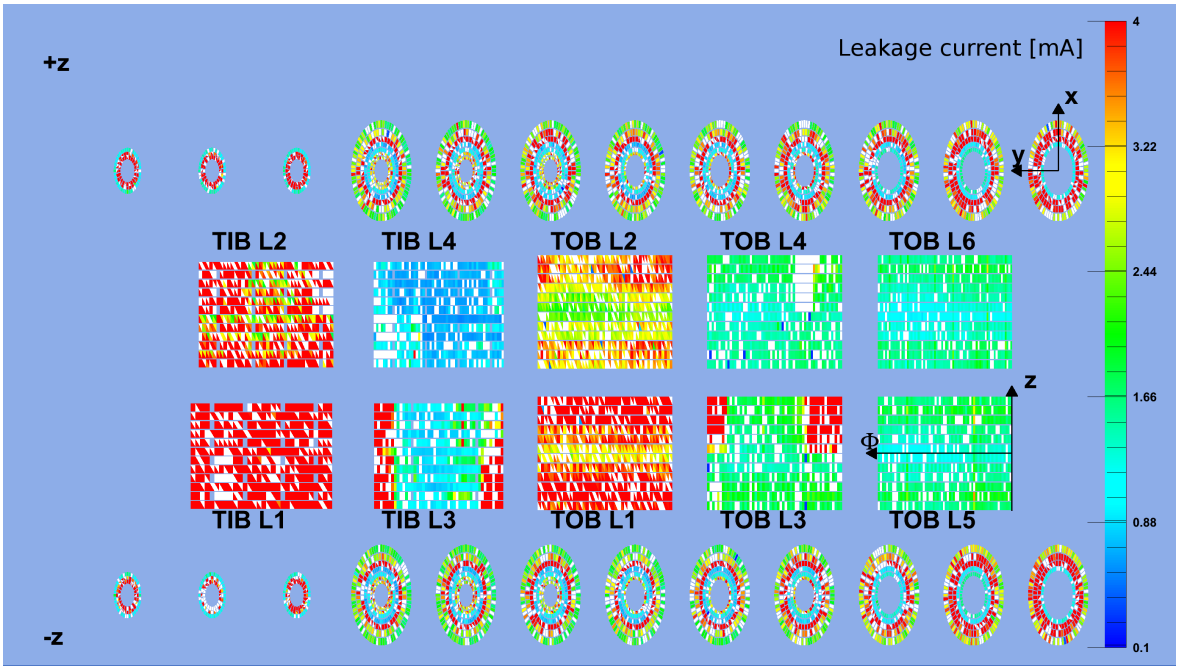

Figure 8.1: Map of the tracker modules with their expected leakage current at 200 fb^{-1} integrated luminosity with the same cooling plant settings as during 2012.

Label	Cooling plant set point during 2011 & 2012	Cooling plant set point between LS1 and LS2	Cooling Plant set point for the first two years after LS2	Cooling plant set point during 2021
A	+4 °C	-5 °C	-10 °C	-20 °C
B	+4 °C	-5 °C	-15 °C	-20 °C
C	+4 °C	-5 °C	-15 °C	-25 °C
D	+4 °C	-10 °C	-15 °C	-15 °C
E	+4 °C	-10 °C	-15 °C	-20 °C
F	+4 °C	-10 °C	-15 °C	-25 °C
G	+4 °C	-10 °C	-20 °C	-20 °C
G	+4 °C	-10 °C	-20 °C	-20 °C

Table 8.1: List of the cooling scenarios used to simulate the evolution of detector properties.

8.1 Prediction of the Leakage Current

In the long run, the high operational temperatures, which are responsible for the present high leakage currents, are having a beneficial effect on the future leakage current. The characteristics of the annealing behavior of leakage current (compare subsection 2.2.3) makes higher temperatures preferable, but only as long as the magnitude of leakage current is acceptable for operational purposes.

Based on this basic insight, a reasonable way to keep the leakage current low in the long term is to reduce the set point of the cooling plant gradually with increasing amounts of radiation damage.

The following scenarios are simulated for a total integrated luminosity of 500 fb^{-1} aligned to the expectations presented in [Zimmer], demonstrated in figure 8.2. The simulation takes the increase of the sensor temperatures into account, caused by increasing leakage currents with finite thermal contacts (see section 7.2.2).

Due to the delicate combination of high operational temperatures and high fluence exposures, the most critical region with respect to the leakage current is situated in the first layer of TIB. In figure 8.3 a simulated evolution of the leakage current and the temperature for an example module in TIB layer 1 is depicted.

It is not clear whether this hot module can be operated with leakage current values above 2 mA. However, another conclusion can be drawn: if instead of cooling scenario 'C' (see table 8.1) cooling scenario 'B' is used, the leakage current would exceed 4 mA already. This is a critical value in a sense that the CAEN A4601 power supplies are only able to provide up to 12 mA ([CAEN]) per channel with a minimum number of three modules connected. The simulated leakage current evolution of the latter scenario is shown in figure 8.4.

The abovementioned calculations have been performed for all modules with a trusted DCU readout for different cooling scenarios. In this way, it is possible to estimate the fraction of modules exceeding certain thresholds of leakage current in dependence of the integrated luminosity. In figure 8.5 the fraction of modules exceeding 1, 2, 3 or 4 mA is shown, assuming cooling scenario 'B' (see table 8.1).

It was mentioned before that not only the maximal leakage current of a module is a concern, the limits of the power supply system also need to be kept in mind. The number of modules connected to one HV line varies from 3-12 modules with a limit of 12 mA. In figure 11.18 the simulated fraction of modules connected to a HV line exceeding 12 mA is plotted in dependency of the integrated luminosity. The cooling assumptions are the same as in the previous example.

The conclusion which can be drawn on figure 11.18 are: The considered cooling scenario will result in a significant loss of tracker modules, with our current power supply system. Still, there are ways to reduce the impact. It is possible to cut the power supply for modules that draw high currents. This can help to keep the remaining modules of the given line operable. Also, an upgrade of the power supply system for a selection of

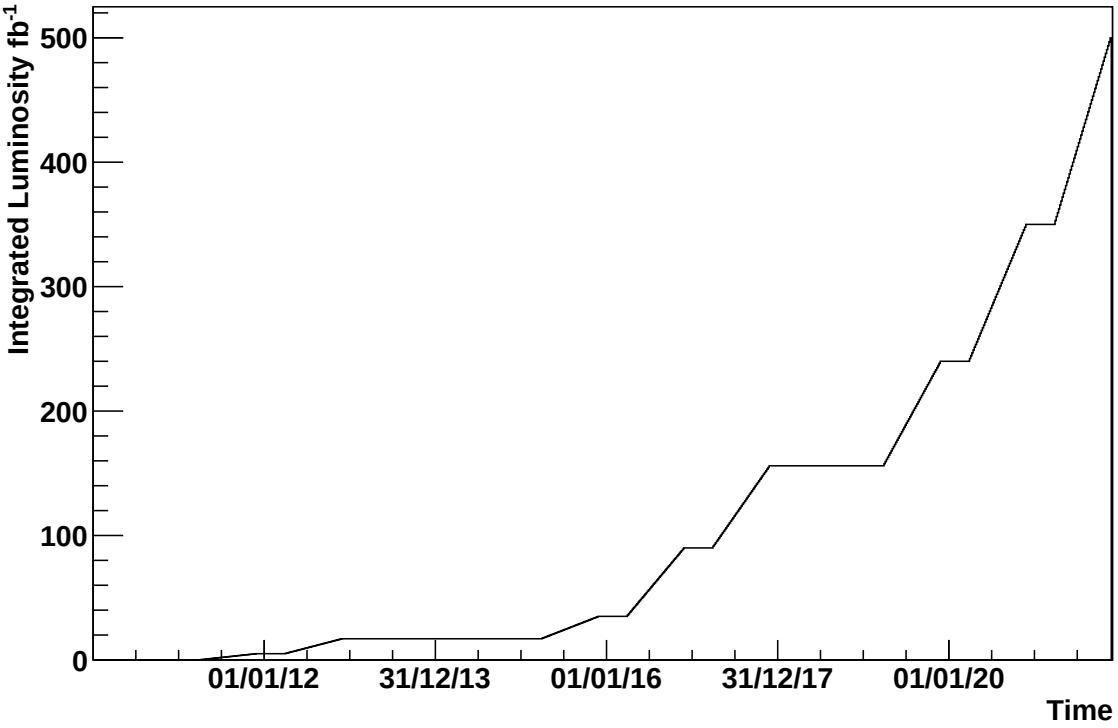

Figure 8.2: Integrated luminosity scenario used for simulations. Included are the long shutdown in 2013 and 2014 (LS1) and the long shutdown in 2018 (LS2).

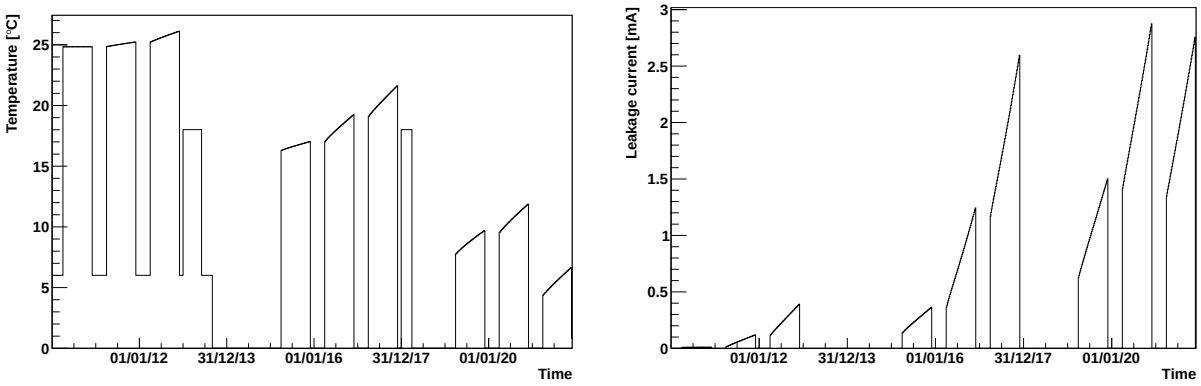

(a) Temperature profile used for simulation

(b) Simulated leakage current

Figure 8.3: Simulated evolution of the temperature and the leakage current for an example module in TIB layer 1. The assumed cooling scenario is 'C' according to table 8.1. Noticeable are the long shutdowns during 2013-2014 and during 2018. For each cooling plant set point the temperature is still increasing with increasing leakage currents due to finite thermal contacts.

channels can be considered after LS2.

In any case, the abovementioned cooling scenario is disadvantageous due to too high temperatures at integrated luminosities around 350 fb^{-1}.

The scenarios presented in this section are only of exemplary nature. For a more extensive set of scenarios the reader is referred to the appendix chapter of this thesis in section 11.1.

In order to keep the number of lost modules in the percentage level, the simulations suggest that the cooling plant set point needs to be at least -5 °C after LS1, -15 °C after LS2 and -20 °C for the last year of operations (scenario 'C'). The optimal set points

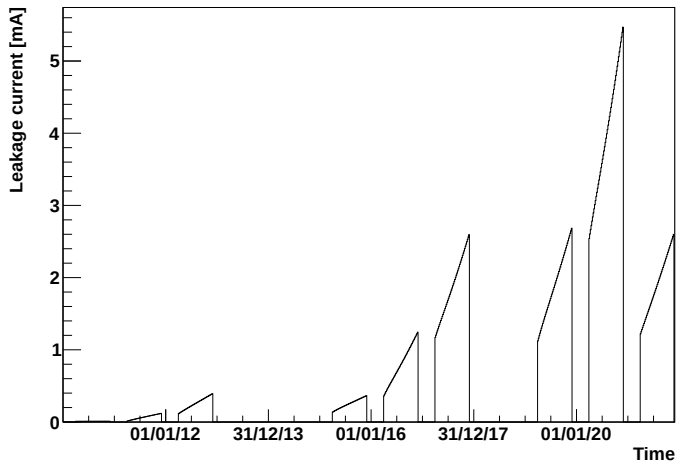

Figure 8.4: Simulated evolution of the leakage current for an example module in TIB L1 based on modified cooling scenario. For this simulation the cooling scenario 'B' is used according to table 8.1. It is noticable that the leakage current would exceed the critical 4 mA for this module towards the end of the -10 °C period in 2020.

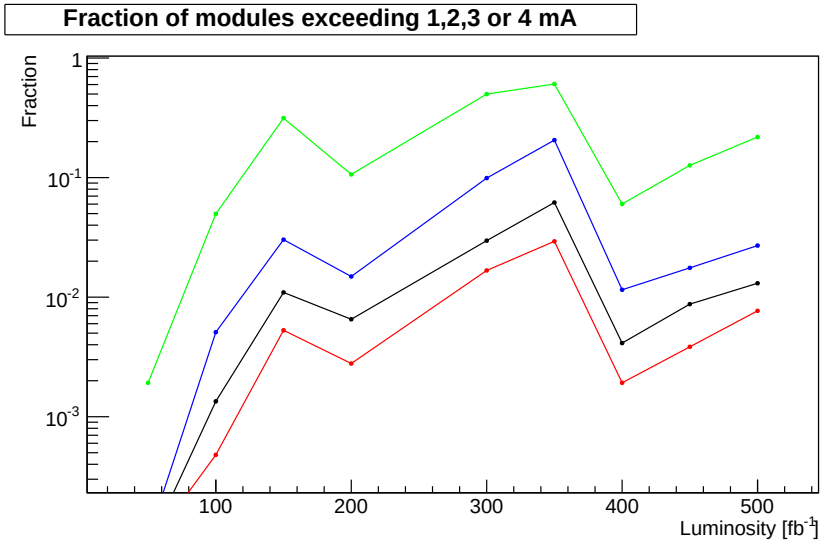

Figure 8.5: Fraction of modules exceeding 1, 2, 3 or 4 mA on a logarithmic scale. For this plot the cooling scenario 'B' (see table 8.1) translates into -5 °C for the first points up to LS2 at 150 fb^{-1}, then -10 °C up to an integrated luminosity of 350 fb^{-1} and -20 °C thereafter.

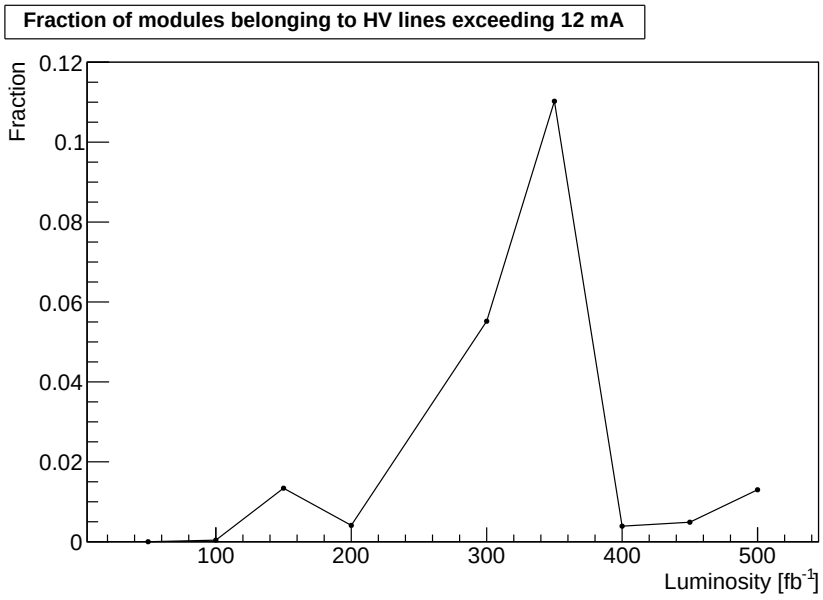

Figure 8.6: Fractions of modules connected to HV lines exceeding 12 mA. For this plot the cooling scenario 'B' (see table 8.1) translates into -5 °C for the first points up to LS2 at 150 fb^{-1}, then -10 °C up to an integrated luminosity of 350 fb^{-1} and -20 °C thereafter.

of the reviewed simulations is provided with scenario 'I', assuming a temperature of -10 °C after LS1, -20 °C after LS2 and -25 °C for the last year of operations.

8.2 Prediction of the Full Depletion Voltage

While for the reduction of the leakage current high operational temperatures are tend to be beneficial in the long run, the situation for the full depletion voltage is more complex. The silicon needs to be kept at sufficiently low temperatures to minimize the impact of reverse annealing (see subsection 2.2.3), while simultaneously warmer periods need to be present in order to use the beneficial effect of the short term annealing (see subsection 2.2.3). Furthermore, it needs to be assessed whether the potential harm to long term operations arises mainly from the leakage current or the full depletion voltage increase. A trade off for the optimal cooling scenario needs to be found since both radiation damage effects cannot be minimized simultaneously.

In figure 8.7 the simulated evolution of the full depletion voltage is shown for the same module that was presented in 8.4, based on the luminosity profile used for the previous examples with a total integrated luminosity of 500 fb^{-1}. For the temperature cooling scenario 'B' has been chosen (see table 8.1).

A disentanglement of the different Hamburg model terms contributing to the effective space charge change in figure 8.7 is depicted in figure 8.8.

For this example, the final full depletion voltage is still below the present operational bias voltage of 300 V. In contrast to the leakage current, which has a strong temperature dependency, the full depletion voltage increases steadily after type inversion. Thus, a good way to assess a temperature scenario is to look at the final full depletion voltage. In figure 8.9 a tracker map of the final depletion voltage values for cooling scenario 'B' (see table 8.1) and 500 fb^{-1} integrated luminosity is shown.

During the quality control phase of the tracker production, bias voltages between 500 V and 800 V have been tested on the modules [Dierla]. During a bias voltage scan in 2011, bias voltage settings of 450 V have been tested on the detector without problems. The power supply limit is 600 V [CAEN]. Consensus within the tracker community is that it is possible to apply a bias voltage of 600 V for the vast majority of modules, even though it has not yet been tested on the detector itself (compare section 5.2.1).

Based on this study, it can be stated that the increase of the full depletion voltage is way less of a concern compared to the increase of the leakage current. Since the operational temperatures need to be reduced due to the leakage current increase, the sensors are not in a temperature regime where reverse annealing could put the operations of the modules at risk.

Even at integrated luminosity values of 700 fb^{-1}, all sensors can be fully depleted according to the simulation, as shown in figure 8.10.

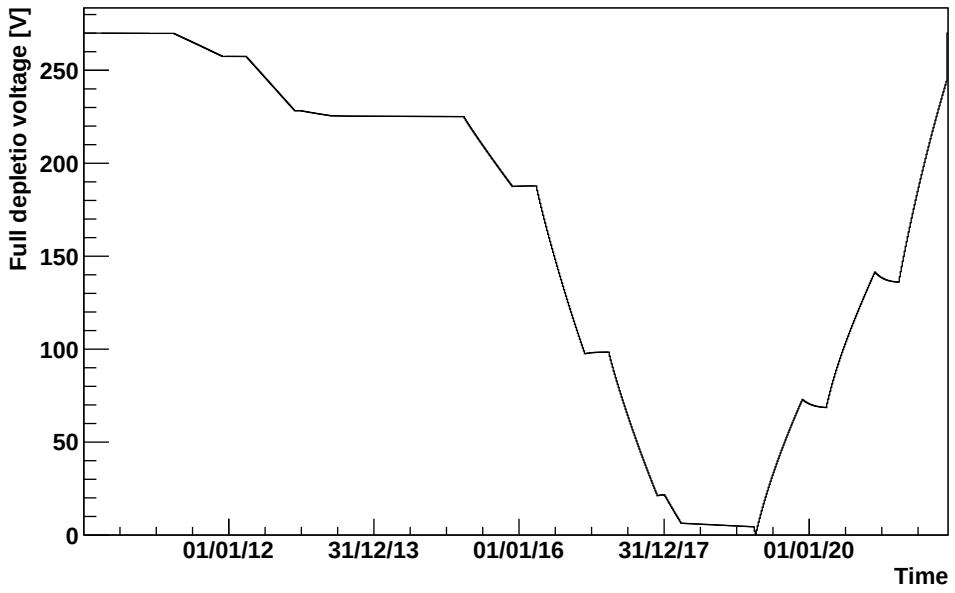

Figure 8.7: Simulated full depletion voltage evolution for an example module in the first layer of the TIB partition.

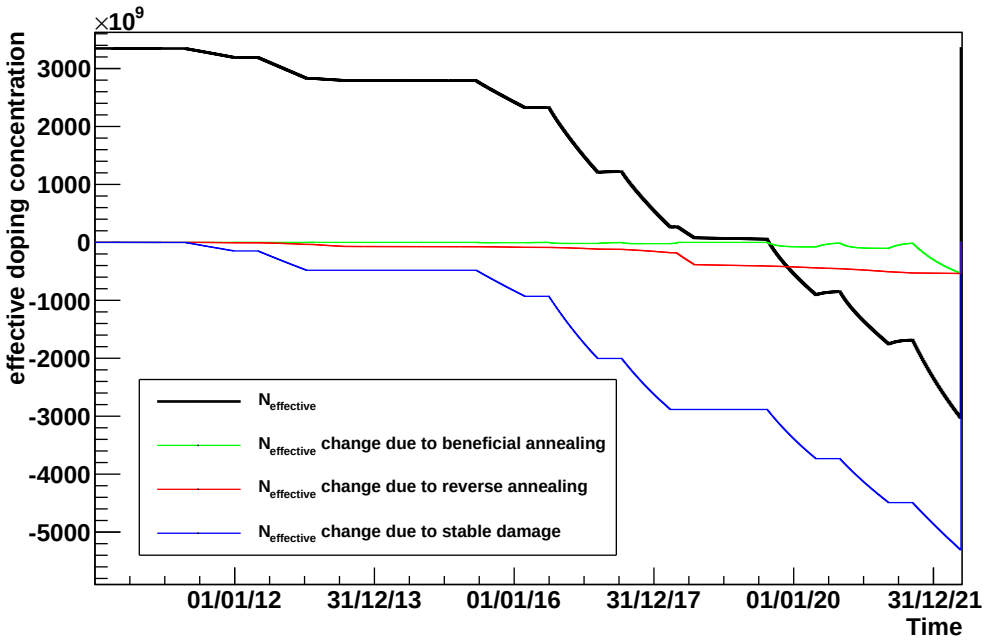

Figure 8.8: Simulated evolution of the effective doping concentration and the contributions of the various Hamburg model terms influencing it.

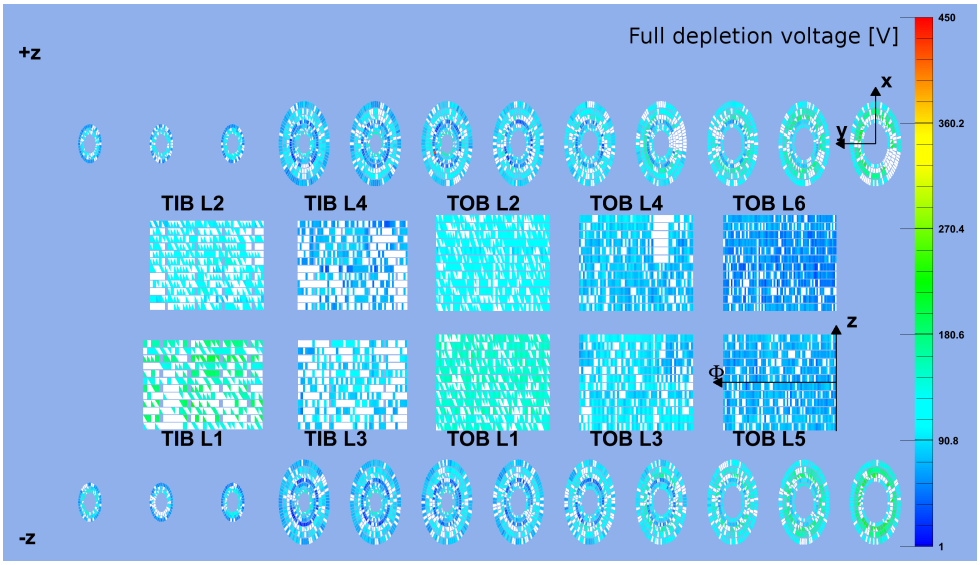

Figure 8.9: Simulated full depletion voltage after an integrated luminosity of 500 fb^{-1}. For this simulation, cooling scenario 'B' has been used (see table 8.1). The white spots correspond to missing thermal contacts or missing initial full depletion voltage values.

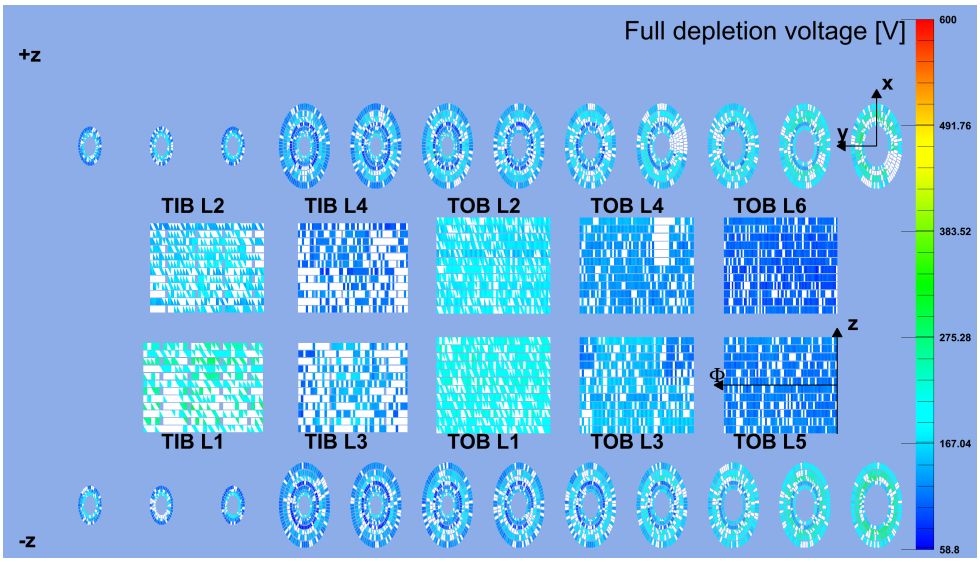

Figure 8.10: Simulated full depletion voltage after an integrated luminosity of 700 fb^{-1}. For this simulation, cooling scenario 'C' has been used (see table 8.1).The white spots correspond to missing thermal contacts or missing initial full depletion voltage values.

Chapter 9

Estimating the Impact on Physics Performance

There is a number of studies investigating the impact of radiation damage on the physics performance of sensor devices, for example [CDF]. The amount of radiation damage the strip sensor suffered so far is not yet causing any significant impact on the physics performance. The crucial quantity affected by radiation damage, with respect to physics performance, is the signal over noise ratio.

9.1 The Signal over Noise Ratio

The signal over noise ratio (S/N) is defined as the ratio between the ADC counts created by an charged traversing particle and the noise ADC count. The signal strength is following a Landau distribution (see section 2.1.5). In case a distinct number for the S/N is quoted one is usually referring to the *most probable value* (MPV) of the distribution. The ratio is affected by radiation damage in multiple ways. The increase in leakage current increases the shot noise (see 2.49). Another noise source is the so-called *single event upset* (SEU). Its effect is that in sensitive areas enough charge is deposited so that the state of a flip-flop is inverted, which leads to an increase in noise. According to [FrBaPe], however, this effect is negligible. At high fluence the trapping (see subsection 2.2.1) reduces the signal strength. A significant drop in the signal occurs when the sensor is not fully depleted anymore.

In figure 9.1 the average year 2011 and 2012 S/N ratios for clusters that have been identified to belong to particle tracks are shown. The data has been collected by [DQM].

It is clearly visible that, during 2012 operations, the S/N decreased already for the inner barrel region with high radiation exposure. In order to investigate whether the reduction of the S/N ratio arises from an increase of the noise or a decrease of the

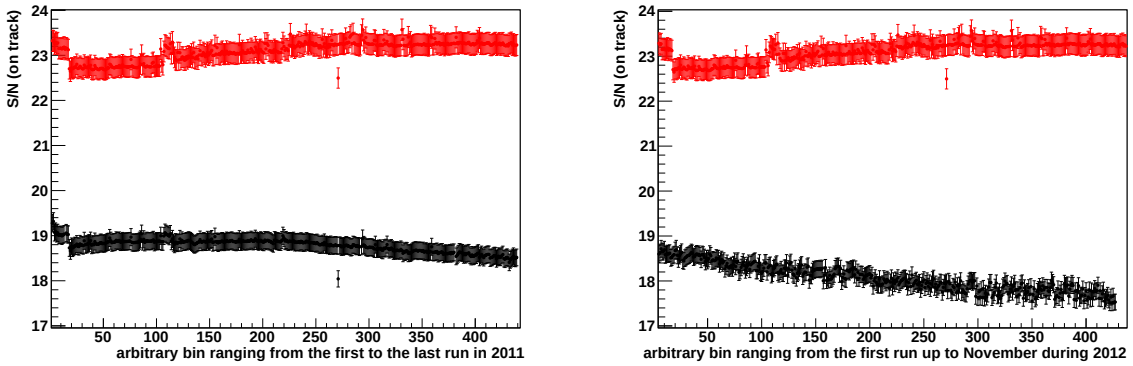

(a) 2011 S/N (b) 2012 S/N

Figure 9.1: S/N evolution during (a) the runs of 2011 and (b) the runs of 2012 in the TIB (lower black curve) and TOB (upper red curve) partition of the CMS microstrip tracker [DQM].

signal, charge and noise are plotted separately for the innermost TIB layer in figure 9.2.

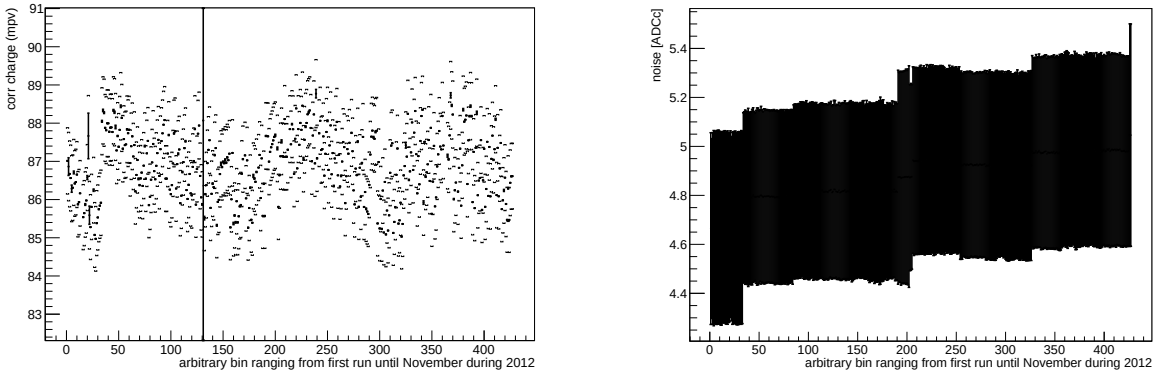

(a) 2012 corrected cluster charge evolution (b) 2012 noise evolution

Figure 9.2: Evolution of (a) the cluster charge and (b) the noise in TIB layer 1 during 2012. The distribution of the signal shows that there is a slight trend towards lower signals which is counteracted several time by a shift up. These steps correspond to new gain settings also visible in the gain corrected noise in plot (b) [DQM].

While there is a slight indication for a degrade in signal in figure 9.2a which is counteracted by repeated adjustments of the gain setting. This affects also the corrected noise shown in figure 9.2b.

In order to asses whether the noise itself also increased we need to investigate the raw noise. The evolution of raw noise for two example modules is shown in figure 9.3.

While for module 369173784 in TIB layer 4 now increase in the noise can be observed for

all APVs, the hotter module 369124646 with is situated in the highly radiation exposed TIB layer 1, is already showing a slight increase in noise in the order of 0.3 ADC counts.

Even though the S/N is a crucial quantity for the physics performance of the tracker, small changes do not necessarily translate into a decreased efficiency or data quality. One can roughly estimate the impact of the shot noise increase on the S/N ratio in the following way: Given that the shot noise increases proportional to the square-root of the leakage current (compare equation 2.49), an increase of the leakage current by a factor of 9 would lead to a three times bigger noise increase. A factor of 9 is already a conservative assumption in the sense that the real increase in leakage current needs to be kept at a way smaller level. One reason is the limit of the power supply of 12 mA per channel ([CAEN]), this limit would be exceeded for the high voltage lines in TIB layer 1 supporting three modules. The noise increase in figure 9.3 is in the order of 5%, with a factor of 3 this would translate into a S/N reduction factor of about 1.15. With the given S/N values of approximately 18, the remaining S/N would still be above 15.6.

The S/N number, at which the physics performance of the tracker is suffering, is usually quoted to be 10. This means that the leakage current induced shot noise alone is not able to compromise the physics performance. However, it will contribute to the degradation of the signal over noise ratio, and need to be kept under control to avoid a hazardous interplay with other signal decreasing effects. In the following section an estimation of the impact of a lowered S/N ratio on the hit efficiency is presented.

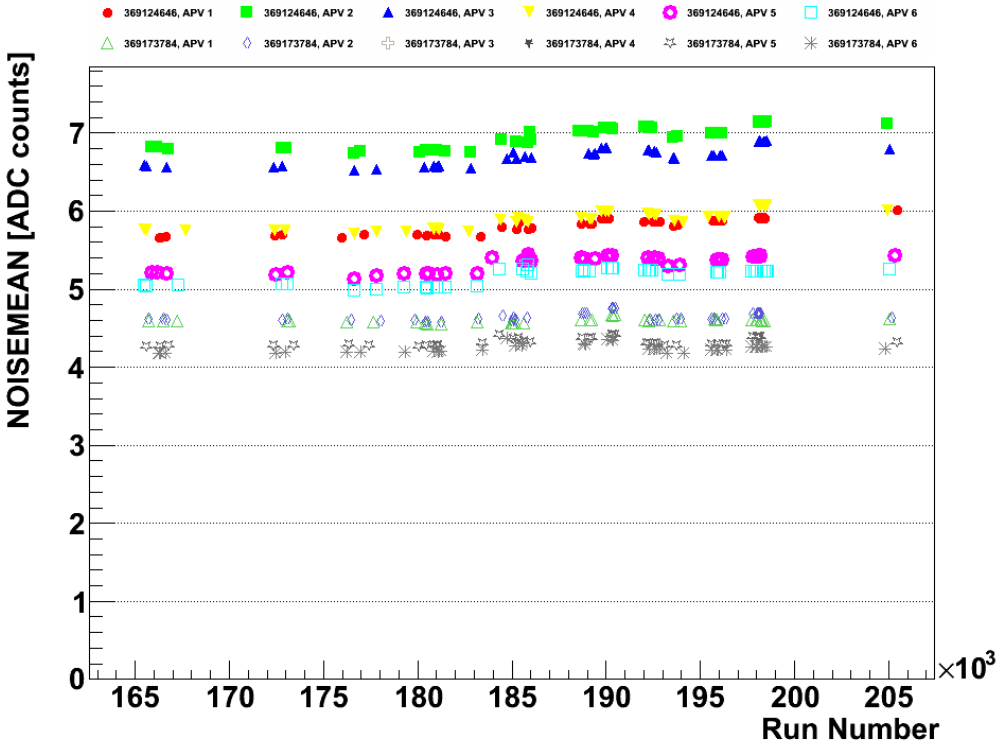

Figure 9.3: Evolution of raw noise for two example modules in the TIB partition [Butz].

9.2 Hit Efficiency of Under-depleted Sensors

The hit efficiency of a silicon microstrip layer is one of the fundamental factors for a good tracking performance. It is defined as the ratio with which a signal hit is found at the position where the traversing particleÂ´s trajectory, calculated by the remaining layers, crosses the layer of investigation. In order to assess the impact of a lowered S/N ratio on the hit efficiency, we reduced the bias voltage in the first layer of TIB and the first layer of TOB to 120 V and to 60 V respectively, while keeping the remaining layers at the operational 300 V. By under-depleting the sensor bulk, the S/N ratio values are lowered significantly as shown in figure 9.4.

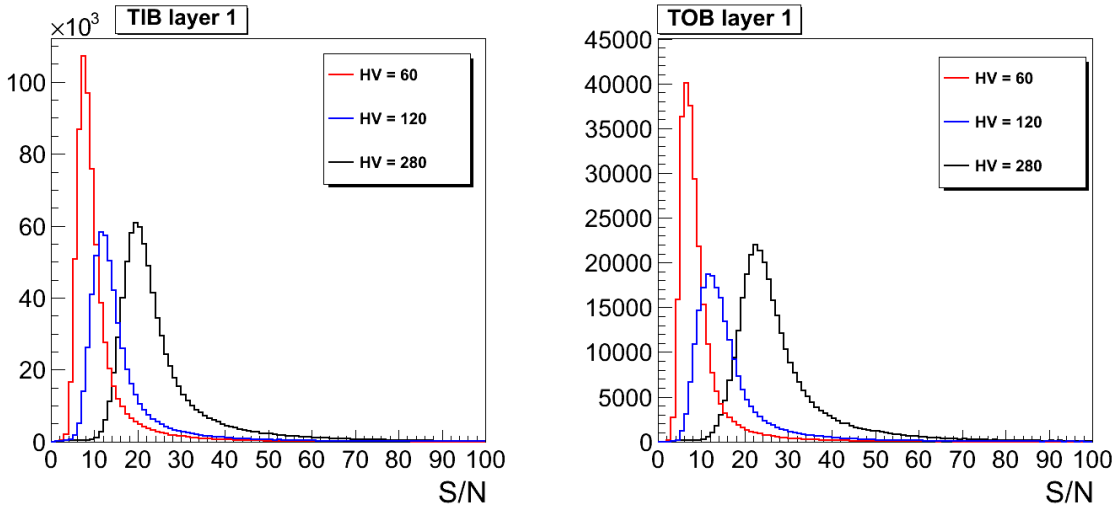

(a) S/N for TIB layer 1 at reduced bias voltage (b) S/N for TIB layer 1 at reduced bias voltage

Figure 9.4: Signal to noise ratio for TIB and TOB layer 1 at reduced bias voltage.

The impact of the hit efficiency is shown in figure 9.5. The plot was created in 2010 for all modules. The official numbers for the hit efficiency, computed for the 2011 data by the detector performance group, is well above 99% for the majority of modules that are qualified as good (see figure 3.7).

While comparing the drop in the hit efficiency, shown in figure 9.5 with the corresponding S/N values depicted in figure 9.4, it is striking that the decrease in the S/N from more than 20 to approximately 12 (for 280 V and 120 V respectively) has only a minimal effect on the hit efficiency. For the lowest S/N values below 10 (at 60 V) the impact on the hit efficiency is significant.

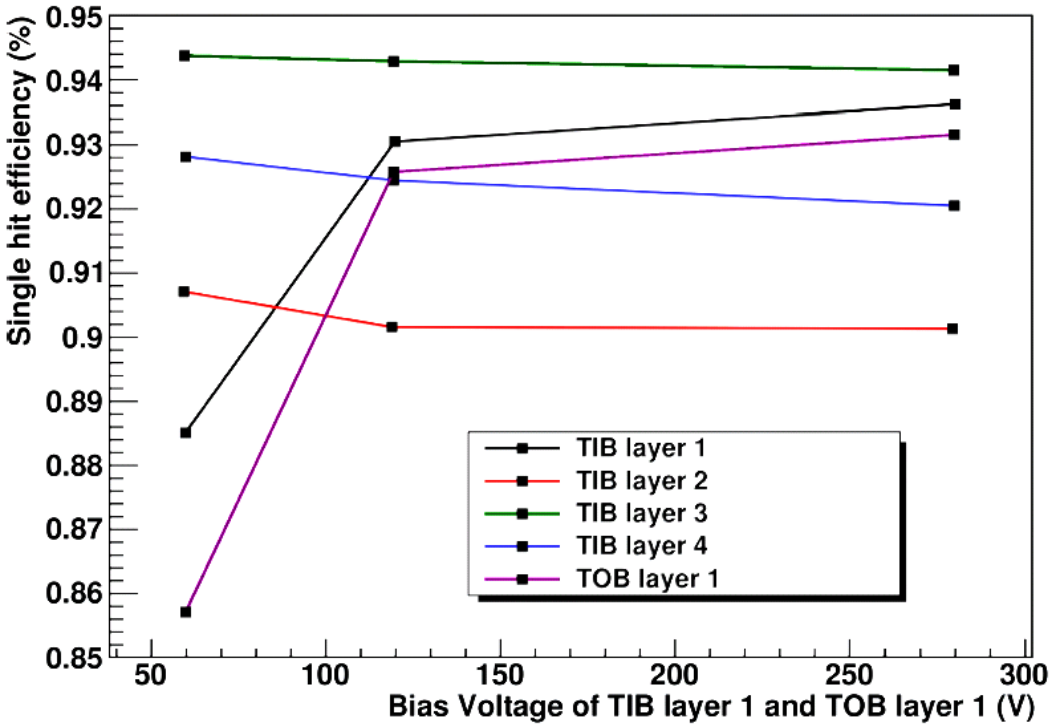

Figure 9.5: The hit efficiency versus the applied bias voltage of the tracker layers TIB L1 and TOB L1.

9.3 Tracking Efficiency and the new Pixel Layer

As a consequence of the lost cooling contacts of 674 modules in the strip tracker, a study was performed to estimate the potential impact on tracking efficiency, assuming that these modules would be lost for further data acquisition [PIXTDR]. Since the majority of uncooled modules are in the first two layers of the TIB partition, a conservative simulation of a loss of 20% efficiency in the first two TIB layers has been used as baseline. The impact on the total tracking efficiency has been simulated, with and without the planned fourth pixel layer. The results of the simulation are summarized in figure 9.6.

It is clearly visible that the tracking efficiency for the upgraded detector with the fourth pixel layer is, in all scenarios, higher than the tracking efficiency of the current detector. This is valid even with the conservative assumption of a 20% loss of efficiency in the first two layers of TIB. Also, the relative impact of an efficiency decrease of the tracker layers is reduced by a fourth pixel layer.

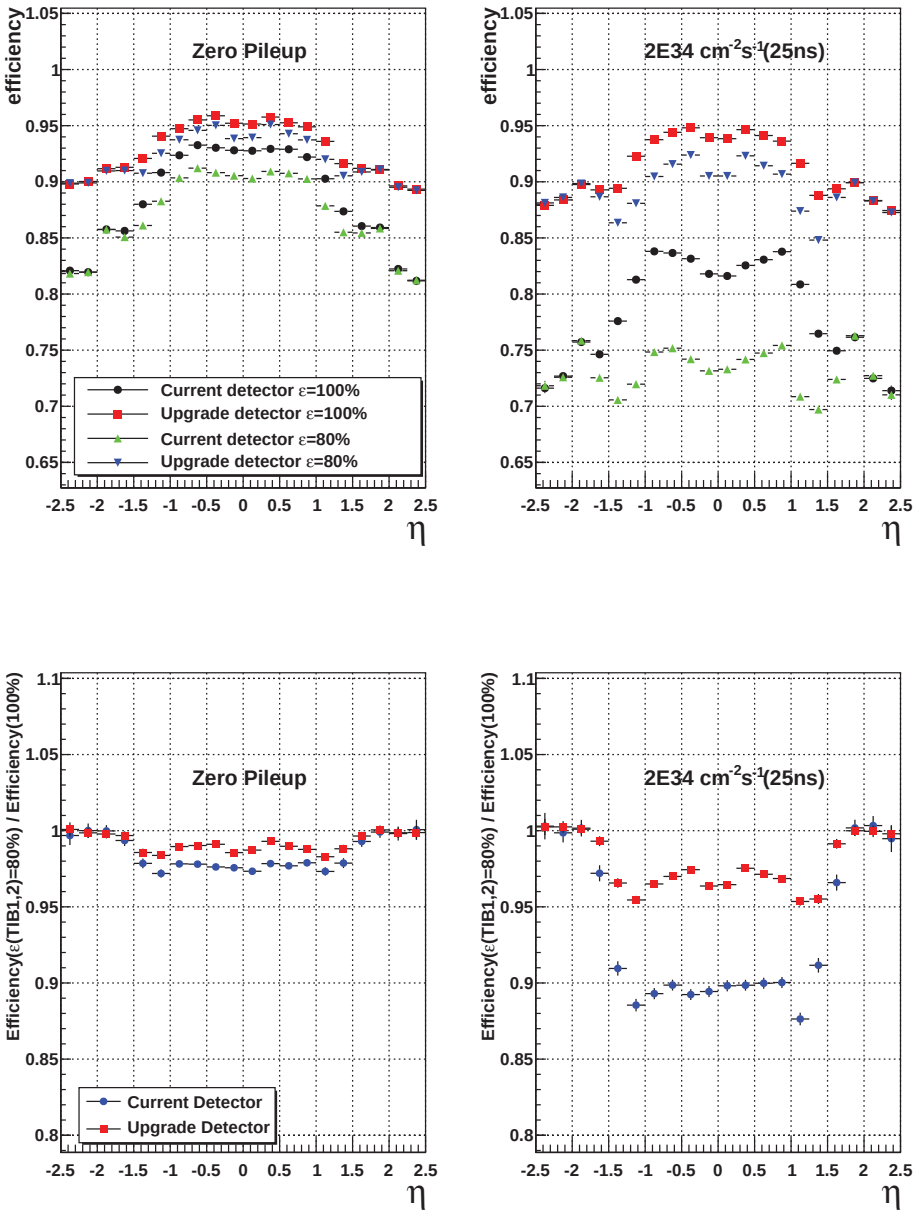

Figure 9.6: Estimated impact of a 20% efficiency loss in TIB layer 1 and 2. The upper left plot shows, in the case of zero pileup, the efficiency for the current detector at 100 % efficiency (black dots) and with a reduced efficiency of 80% in TIB layer 1 and 2 (green triangles). In addition, the same efficiencies are shown including a new fourth layer of the pixel detector (red squares, blue inverted triangles). The upper right plot shows the same efficiencies for an average pileup of 50. The lower left plot shows the relative impact of a 20% efficiency drop in TIB layer 1 and 2 for the current detector (blue dots) and for the upgraded detector with a fourth pixel layer (red squares) at zero pileup. The plot on the bottom left shows the same relative impact at an average pileup of 50. All efficiencies are simulated for default tracks in a $t\bar{t}$ sample as a function of the pseudorapidity η. The figure is taken from [PIXTDR].

Chapter 10

Conclusion

A practical tool has been developed to estimate the evolution of the leakage current and the full depletion voltage. The tool computes the radiation damage of each days' irradiation, taking annealing into account based on the respective temperature of all following days. The final impact on the sensor properties is given by the integral of each day's radiation damage. With the available measurements until fall 2012, the simulations have been validated. The relative deviations between the modeled data and the measurements are below 7% and no indication of a disagreement with the established radiation damage model has been observed (subsection 7.3.1). In addition to this simulation software, two in-situ measurement techniques and analysis approaches have been proposed to determine the full depletion voltage in this thesis.

- The signal approach yields accurate results but has a negative impact on the data quality during the scan. A part of the signal method is to create template curves for the change of the particle tracks' signal strength with changing bias voltage settings; based on basic considerations of physical processes within the silicon bulk and the module geometry. These curves are fitted to the measured dependency of the on-track cluster charge on the bias voltage. The full depletion voltage values obtained this way have been compared to the C-V measurements performed during the production phase. The absolute deviations between the two measurements show a systematic offset in the order of 5 V and a spread in the order of 15 V (see section 6.3).

- The noise approach can be performed during maintenance periods but is less precise. The in-situ method utilizes the dependency of the sensor's noise on the applied bias voltage. A comparison between the C-V measurements, the signal measurements and the noise measurements indicates that the noise method has the highest spread. Nevertheless, the noise approach provides a valuable supplement to the determination of the full depletion voltage.

Both approaches have been thoroughly tested and thus qualified as suitable run modes of the strip tracker. Consequently, they became part of the standard CMS operations and are performed on a regular basis. Up to mid 2012 there is no sign of a change

of the full depletion voltage within the CMS strip tracker. However, the combination of the simulation software tool and the measurement techniques laid the foundation for future comparisons between the established radiation damage model and physical reality on a high statistics and high diversity data sample.

Another important part of this thesis are predictions for the evolution of sensor properties for different cooling scenarios. Based on these computations, it is expected that the tracker will be able to endure more than the estimated 500 fb^{-1} of integrated luminosity, provided that the thermal conditions can be lowered significantly after the long shutdown of 2013 and 2014 (compare chapter 8). A significant contribution to the minimization of radiation damage effects is the thermal screen. It continuously provides a cooling of the tracker volume, especially during maintenance periods when the main cooling plant is not operational. This implies that the undesirable reverse annealing which adversely affects the full depletion voltage of the sensors can be kept low. Under these circumstances, estimates are that the power supply system will be able to provide the needed bias voltage to fully deplete all sensors until the end of phase 1 operations in 2021 and beyond.

Even though the increase in leakage current is more concerning, it is fairly certain that the vast majority of modules with proper cooling contact will withstand the expected radiation damage of the LHC. The annealing processes of the leakage current are beneficial. The higher the temperatures are the more defects recombine. This results in a reduction of the underlying cause of leakage current. On the other hand, the leakage current itself has a strong thermal dependency and high operational temperatures increase the current significantly. This behavior directly demonstrates the existence of optimal cooling conditions that providing a maximum amount of annealing while still keeping the leakage current at an acceptable level. Since the fluence exposure is steadily increasing during LHC running a gradual decrease in temperature is preferable. A suboptimal sealing of support structures is forcing the tracker community to operate at temperatures above the design values. Against the background of the radiation damage model of leakage current, this is in fact a beneficial thermal setting. That being said, even if efforts to perfectly seal the tracker during its long shutdown in 2013 and 2014 would partly fail, a progressive reduction of the cooling set points would still allow for the opportunity to eventually reach the final temperatures after the second long shutdown planned for 2018. At the end of phase 1 in 2021, the operational temperatures need to reach -20 °C as has been shown in chapter 8.

The impact of radiation damage effects on the hit efficiency and signal over noise ratio has been estimated. An extrapolation of the observed effects into the future suggests that the data quality will not be significantly affected until the end of phase 1. Concerning the lost cooling contact of a number of modules, a variety of interventions are feasible to avoid unnecessary heating and potential thermal runaways. One possible option is to remove the power for extraordinary hot modules by switching to appropriate jumper settings. In this way, only the offending modules would be lost for data-taking purposes, but the remaining modules of the power supply channel would potentially still be operable. A conservative list of modules which might be lost eventually consists

of 674 entries, representing well below 5% of the tracker's total number of modules. In addition, when taking into account a planned fourth pixel layer, investigations concerning the loss of uncooled modules demonstrate that the tracking performance is going to stay at excellent levels over the whole period of data taking.

The expected integrated luminosity of the coming years in combination with lower temperatures allow for further radiation damage studies. Firstly, for the full depletion voltage change, which will be accessible by the presented methods. Secondly, the decreasing temperatures are going to bring the leakage current into a regime that is less prone to temperature uncertainties, since the relative impact of temperature modifications decreases at lower temperatures. Additionally, the resolution of the DCUs will improve while moving towards the design temperatures of -10 °C due to a better dynamic range of the electronics.

In summary, this paper showed that the CMS microstrip tracker is in a good shape and more than adequate to efficiently record and process future collision data. In its development, a rich set of tools to investigate radiation damage effects has been introduced, which allows for an extensive assessment of radiation damage models.

Chapter 11

Appendix

11.1 The Different Cooling Scenarios

In chapter 8 a table with the simulated cooling scenarios have been presented (8.1).

Label	Cooling plant set point during 2011 & 2012	Cooling plant set point between LS1 and LS2	Cooling Plant set point for the first two years after LS2	Cooling plant set point during 2021
A	+4 °C	-5 °C	-10 °C	-15 °C
B	+4 °C	-5 °C	-10 °C	-20 °C
C	+4 °C	-5 °C	-15 °C	-20 °C
D	+4 °C	-5 °C	-15 °C	-25 °C
E	+4 °C	-10 °C	-15 °C	-15 °C
F	+4 °C	-10 °C	-15 °C	-20 °C
G	+4 °C	-10 °C	-15 °C	-25 °C
H	+4 °C	-10 °C	-20 °C	-20 °C
I	+4 °C	-10 °C	-20 °C	-20 °C

Table 11.1: List of the cooling scenarios used to simulate the evolution of detector properties.

In the following sections, the impact of the thermal conditions on the leakage current and full depletion voltage is assessed.

11.1.1 Cooling Scenario A

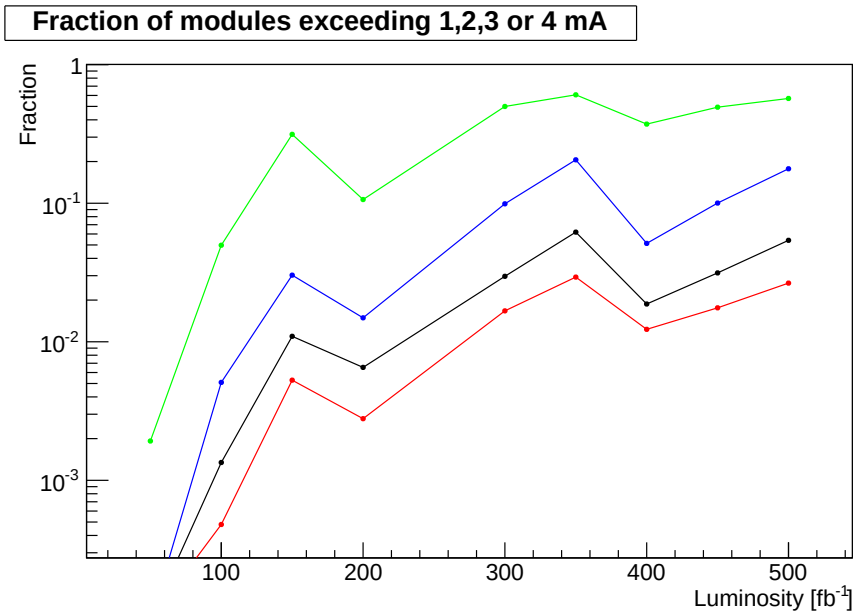

Figure 11.1: Fraction of modules exceeding 1,2,3 or 4 mA on a logarithmic scale. The cooling scenario 'A' translates for this plot into -5 °C for the first points up to LS2 at 150 fb^{-1}, -10 °C up to an integrated luminosity of 350 fb^{-1} and -15 °C after.

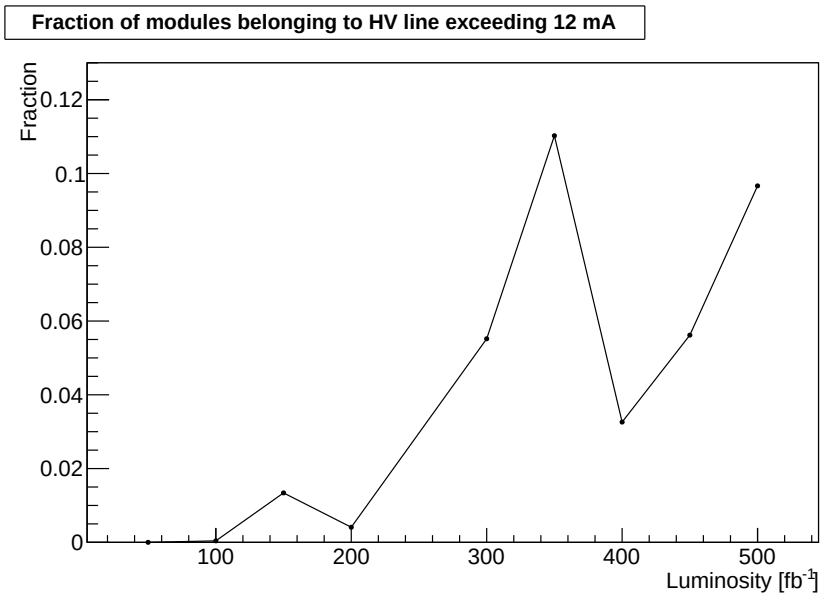

Figure 11.2: Fractions of modules connected to HV lines exceeding 12 mA. The cooling scenario 'A' translates for this plot into -5 °C for the first points up to LS2 at 150 fb^{-1}, -10 °C up to an integrated luminosity of 350 fb^{-1} and -15 °C after.

11.1.2 Cooling Scenario B

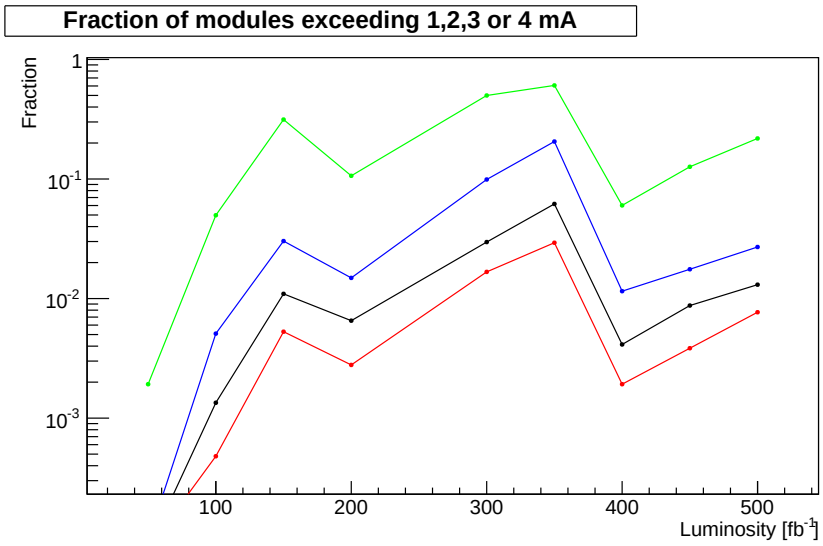

Figure 11.3: Fraction of modules exceeding 1,2,3 or 4 mA on a logarithmic scale. The cooling scenario 'B' translates for this plot into -5 °C for the first points up to LS2 at 150 fb^{-1}, -10 °C up to an integrated luminosity of 350 fb^{-1} and -20 °C after.

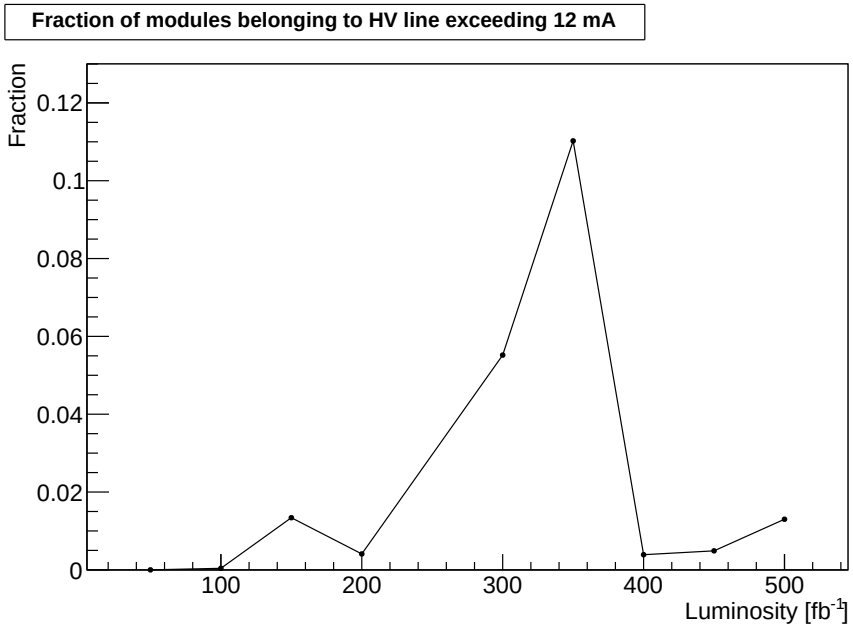

Figure 11.4: Fractions of modules connected to HV lines exceeding 12 mA. The cooling scenario 'B' translates for this plot into -5 °C for the first points up to LS2 at 150 fb^{-1}, -10 °C up to an integrated luminosity of 350 fb^{-1} and -20 °C after.

11.1.3 Cooling Scenario C

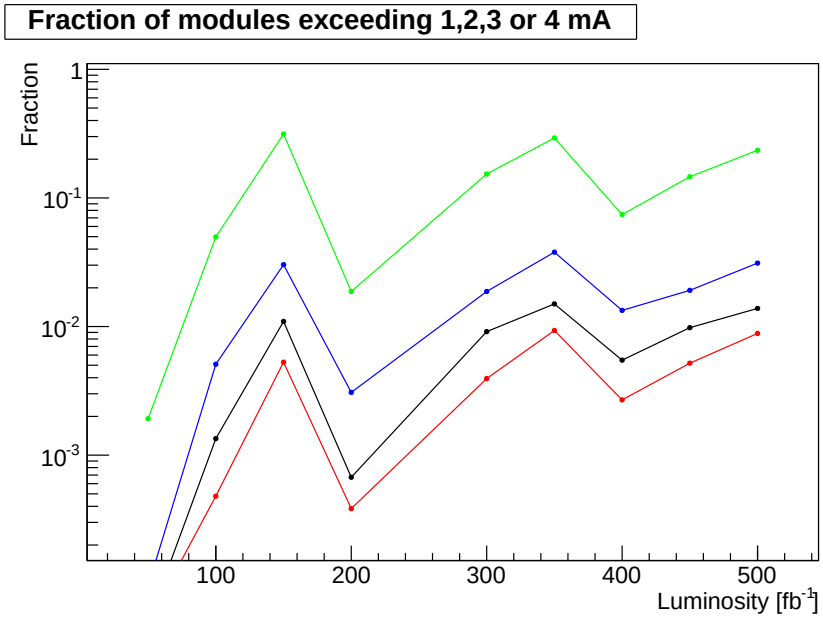

Figure 11.5: Fraction of modules exceeding 1,2,3 or 4 mA on a logarithmic scale. The cooling scenario 'C' translates for this plot into -5 °C for the first points up to LS2 at 150 fb^{-1}, -15 °C up to an integrated luminosity of 350 fb^{-1} and -20 °C after.

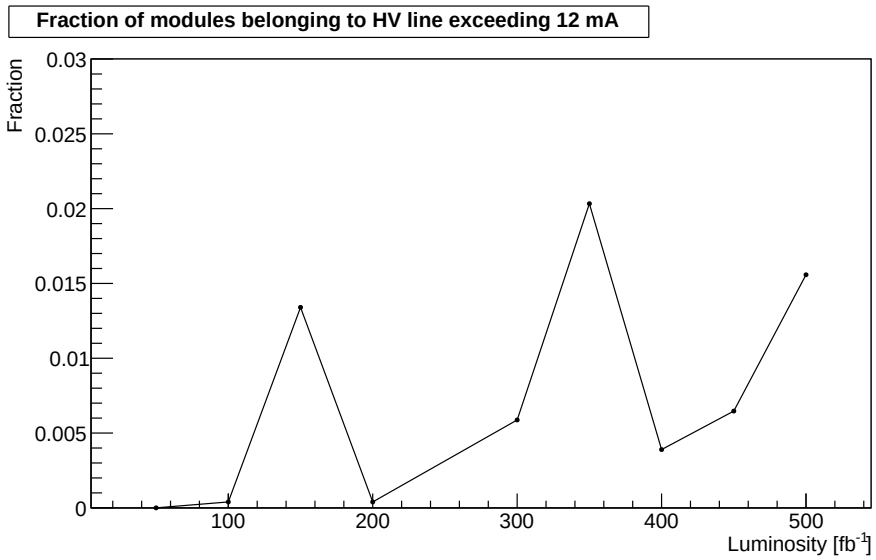

Figure 11.6: Fractions of modules connected to HV lines exceeding 12 mA. The cooling scenario 'C' translates for this plot into -5 °C for the first points up to LS2 at 150 fb^{-1}, -15 °C up to an integrated luminosity of 350 fb^{-1} and -20 °C after.

11.1.4 Cooling Scenario D

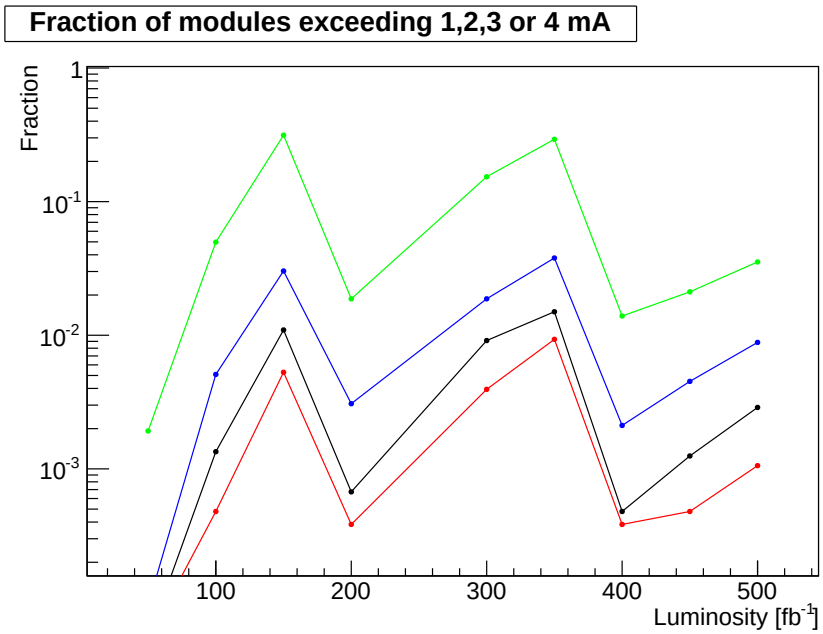

Figure 11.7: Fraction of modules exceeding 1,2,3 or 4 mA on a logarithmic scale. The cooling scenario 'D' translates for this plot into -5 °C for the first points up to LS2 at 150 fb^{-1}, -15 °C up to an integrated luminosity of 350 fb^{-1} and -25 °C after.

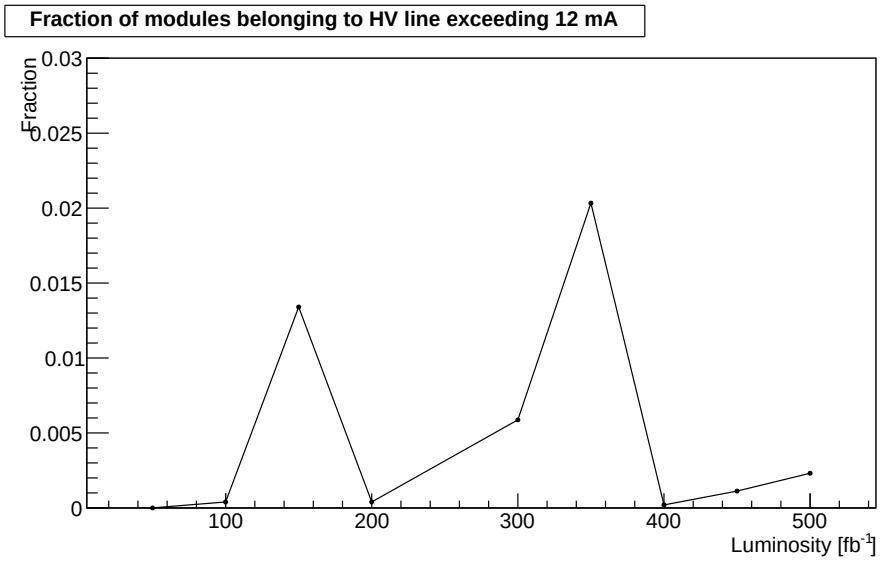

Figure 11.8: Fractions of modules connected to HV lines exceeding 12 mA. The cooling scenario 'D' translates for this plot into -5 °C for the first points up to LS2 at 150 fb^{-1}, -15 °C up to an integrated luminosity of 350 fb^{-1} and -25 °C after.

11.1.5 Cooling Scenario E

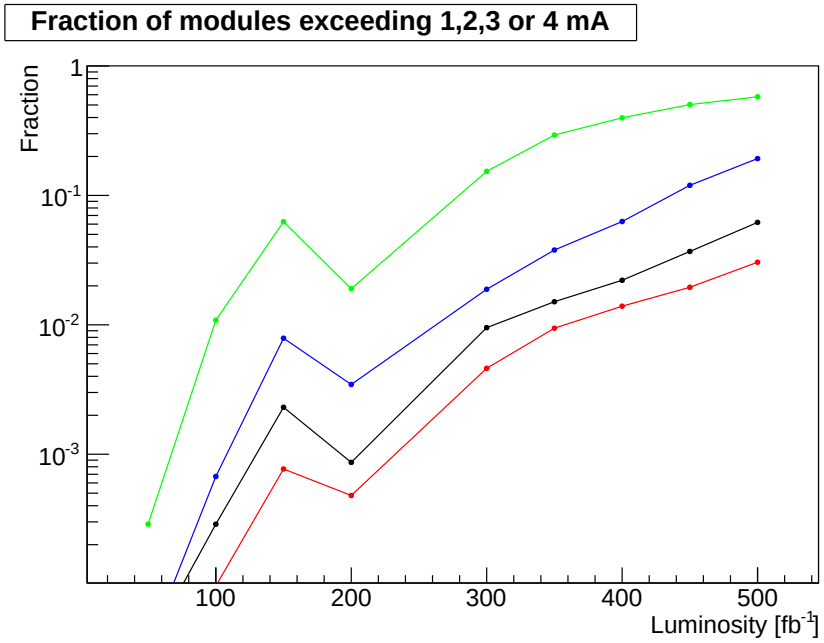

Figure 11.9: Fraction of modules exceeding 1,2,3 or 4 mA on a logarithmic scale. The cooling scenario 'E' translates for this plot into -10 °C for the first points up to LS2 at 150 fb^{-1} and -15 °C afterwards

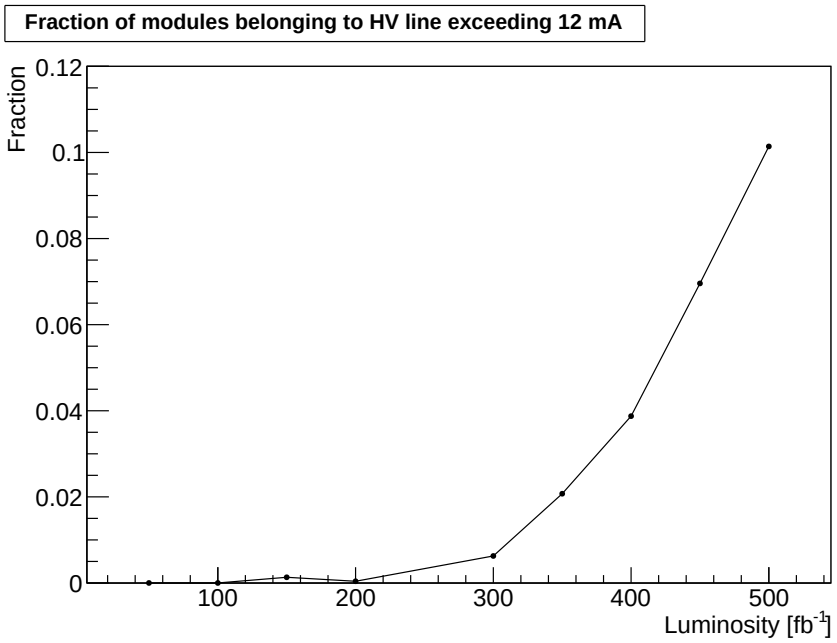

Figure 11.10: Fractions of modules connected to HV lines exceeding 12 mA. The cooling scenario 'E' translates for this plot into -10 °C for the first points up to LS2 at 150 fb^{-1} and -15 °C afterwards.

11.1.6 Cooling Scenario F

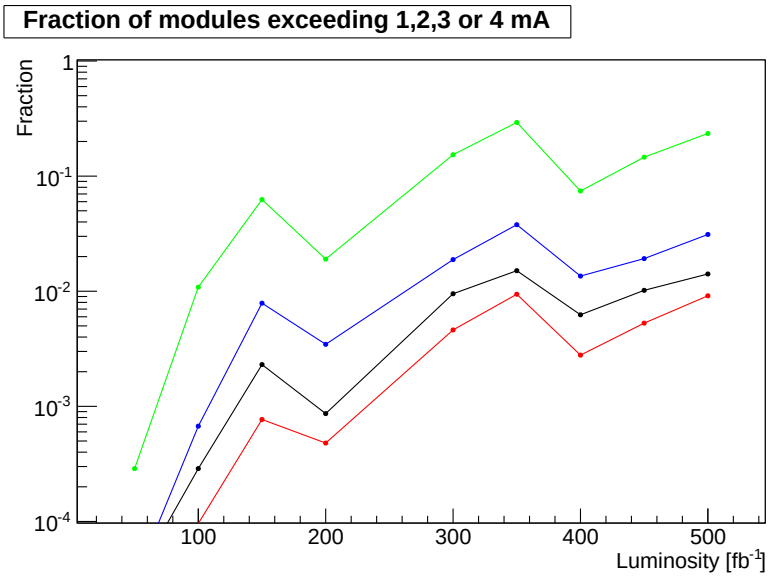

Figure 11.11: Fraction of modules exceeding 1,2,3 or 4 mA on a logarithmic scale. The cooling scenario 'F' translates for this plot into -10 °C for the first points up to LS2 at 150 fb^{-1}, -15 °C up to an integrated luminosity of 350 fb^{-1} and -20 °C after.

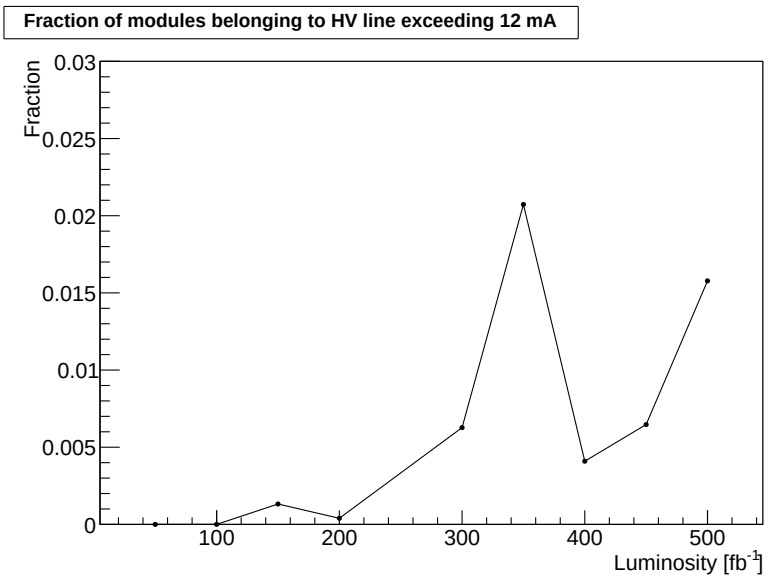

Figure 11.12: Fractions of modules connected to HV lines exceeding 12 mA. The cooling scenario 'F' translates for this plot into -10 °C for the first points up to LS2 at 150 fb^{-1}, -15 °C up to an integrated luminosity of 350 fb^{-1} and -20 °C after.

11.1.7 Cooling Scenario G

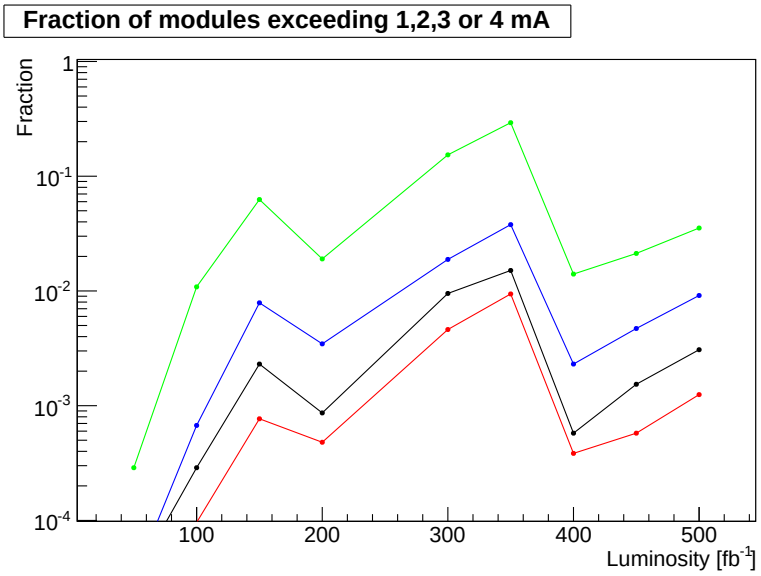

Figure 11.13: Fraction of modules exceeding 1,2,3 or 4 mA on a logarithmic scale. The cooling scenario 'G' translates for this plot into -10 °C for the first points up to LS2 at 150 fb^{-1}, -15 °C up to an integrated luminosity of 350 fb^{-1} and -25 °C after.

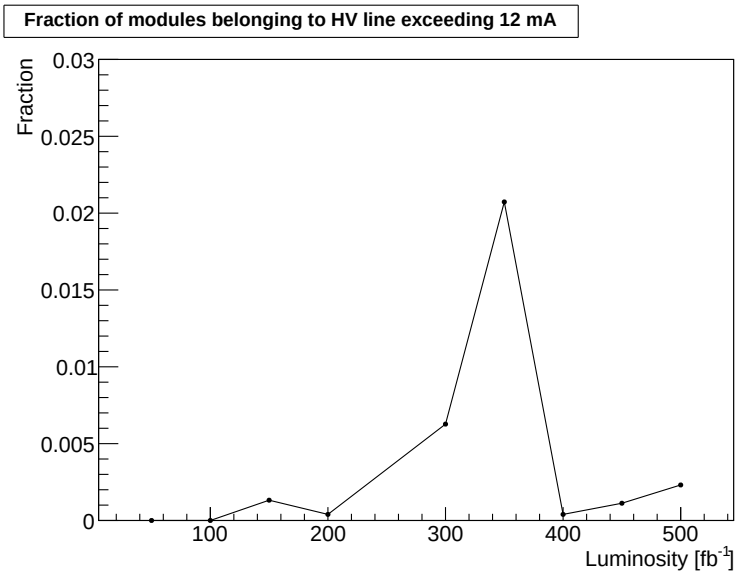

Figure 11.14: Fractions of modules connected to HV lines exceeding 12 mA. The cooling scenario 'G' translates for this plot into -10 °C for the first points up to LS2 at 150 fb^{-1}, -15 °C up to an integrated luminosity of 350 fb^{-1} and -25 °C after.

11.1.8 Cooling Scenario H

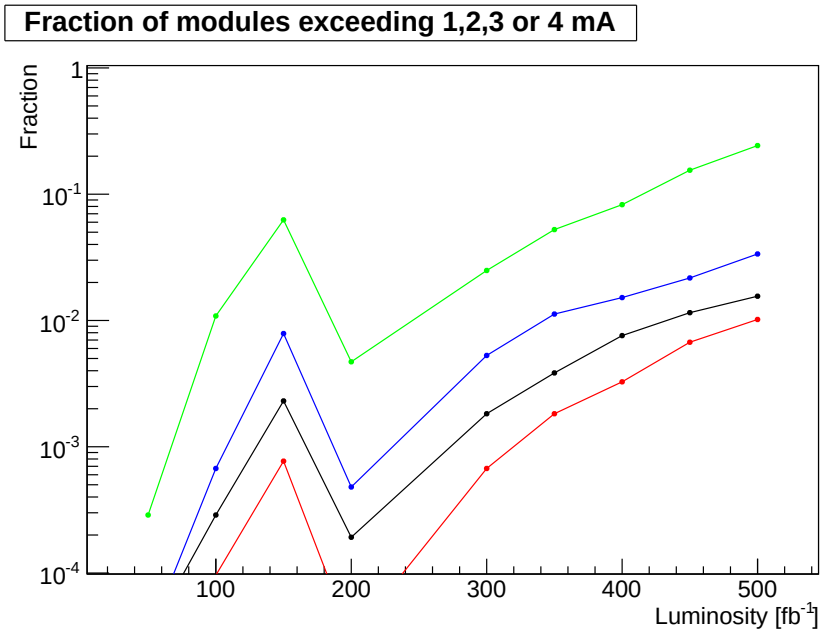

Figure 11.15: Fraction of modules exceeding 1,2,3 or 4 mA on a logarithmic scale. The cooling scenario 'H' translates for this plot into -10 °C for the first points up to LS2 at 150 fb^{-1} and -20 °C afterwards.

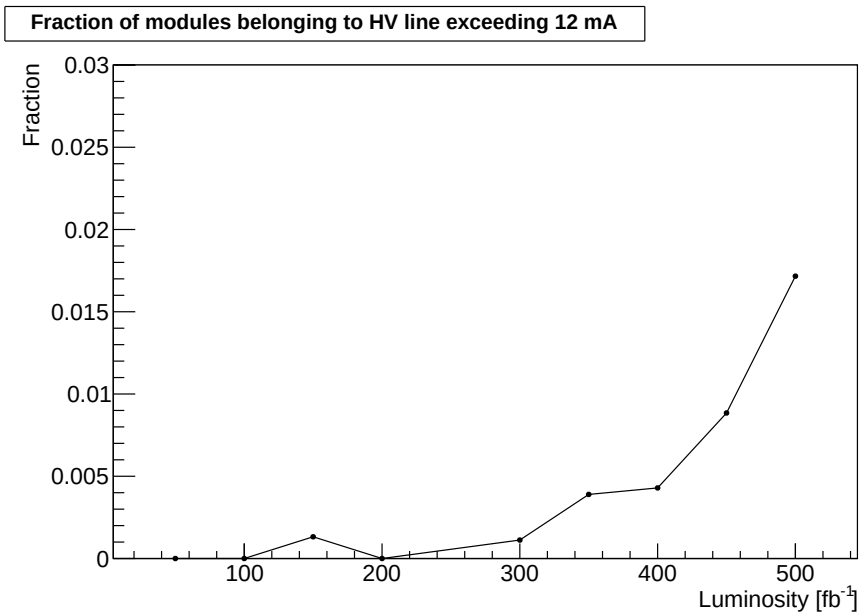

Figure 11.16: Fractions of modules connected to HV lines exceeding 12 mA. The cooling scenario 'H' translates for this plot into -10 °C for the first points up to LS2 at 150 fb^{-1} and -20 °C afterwards.

11.1.9 Cooling Scenario I

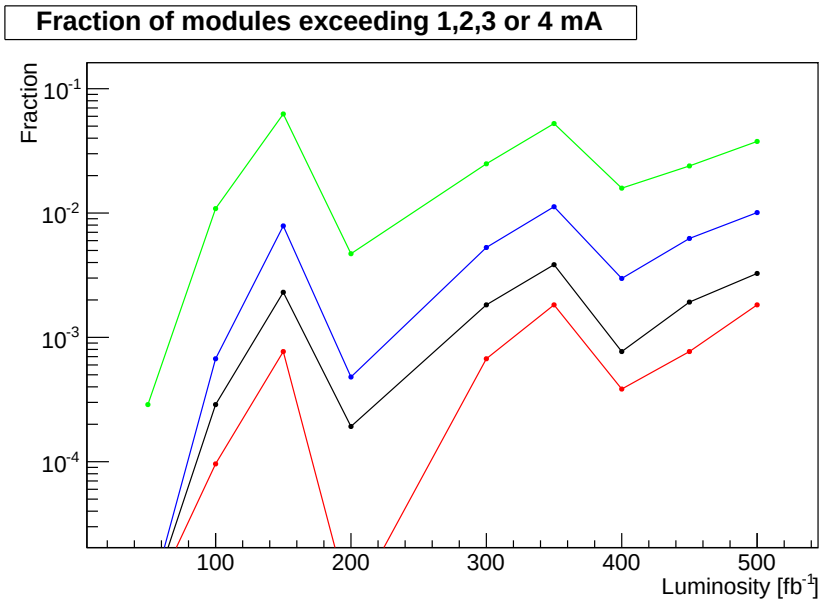

Figure 11.17: Fraction of modules exceeding 1,2,3 or 4 mA on a logarithmic scale. The cooling scenario 'I' translates for this plot into -10 °C for the first points up to LS2 at 150 fb^{-1}, -20 °C up to an integrated luminosity of 350 fb^{-1} and -25 °C after.

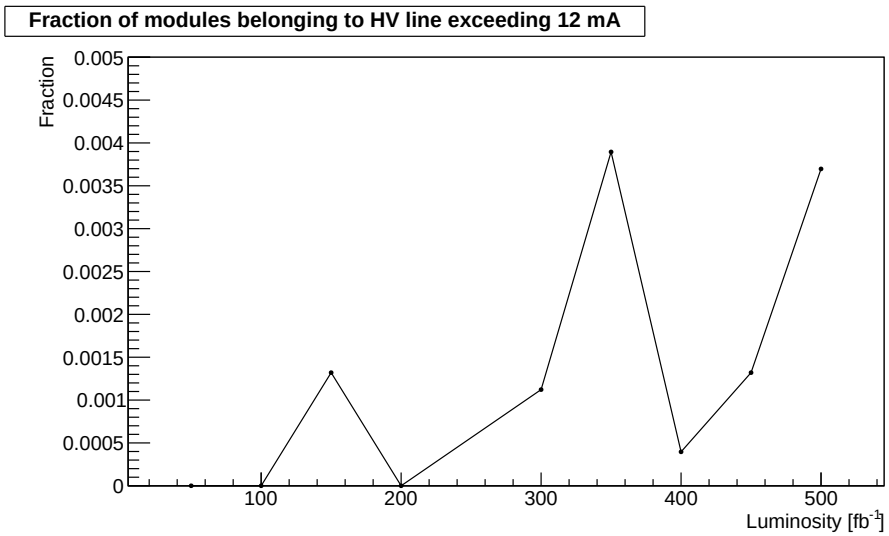

Figure 11.18: Fractions of modules connected to HV lines exceeding 12 mA. The cooling scenario 'I' translates for this plot into -10 °C for the first points up to LS2 at 150 fb^{-1}, -20 °C up to an integrated luminosity of 350 fb^{-1} and -25 °C after.

Chapter 12

Acknowledgement

Firstly, I want to deeply thank Prof. Thomas Müller for giving me the opportunity to work on this exciting topic and for supporting and advising me during the years of this study. A special thank is due to Prof. de Boer for being the second reviewer and for fruitful suggestions during the monthly meetings in Karlsruhe.

For my supervision at CERN, for great support, for sedulous help and friendship beyond the scope of work I want to express my gratitude to Frank Hartmann.

During my time at CMS I worked with numerous people contributing to a delightful working atmosphere. The first I want to thank is Stefano Mersi for supervising the full depletion voltage group, for never getting tired of giving me private lectures and for friendship and support. In addition, I want to thank all people that contributed to this project namely: Jeremy Andrea, Jean-Laurent Agram, Jean-Charles Fontaine, Gabriele Benelli, Michael Segala and for many sophisticated comments Andrea Venturi. A special thank is dedicated to the tracker management team around Karl Gill for the aid and confidence shown to me. For a private root session and many advises I warmly thank Erik Butz. I enjoyed a lot the work with the whole operations team and I want to highlight Lino Demaria, Alexander Kaminsky, Francesco Palmonari, Derek Strom, Guido Dirkes and Michael Hoch. For great collaboration I want to thank my DCS colleagues: Lorenzo Masetti, Robert Stringer, Alessandro Gaz and William Gabella. For appreciation and good collaboration I also want to thank Andromachi Tsirou and Piero Giorgio Verdini.

For the Fluka simulations I want to thank Moritz Guthoff. For the simulations of the APV response a special thanks is due to Mark Raymond.

I thank all members of my home institute at the northern campus of the KIT especially Alexander Dierlamm for proof reading parts of my thesis, but also to Prof. Husemann, Hans-Juergen Simonis, Thomas Weiler, Robert Eber, Karl-Heinz Hoffmann, Alexis Descroix, Andreas Nürnberg, Stefan Heindl and all remaining members of the coffee group.

For great hospitality at the southern campus of the KIT, I want to thank Jeannine

Wagner-Kuhr, Hauke Held, Thorsten Chwalek, Jochen Ott, Christian Böser and all members of the lunch crew.

For steady and uncomplicated help in bureaucratic aspects I want to thank Bärbel Bräunling, Diana Fellner and Brigitte Gering.

I wish to thank all my friends that accompanied me during my life, especially Mirko Deforth, Sarah Jochum and Boris Deforth for patient proof reading of my thesis but also Peter Eberle, Philip Busch, Eva Steiner and Maria Braunschmidt.

My warmest gratitude appertains to my family who enabled me to study and who supported me during my whole life; thank you so much!

Last but not least I want to thank my longtime girlfriend Susanna for loving me through hell and high water.

List of Figures

List of Tables

Bibliography

[AgrFon] J.-L. Agram, J.-C. Fontaine, *private communication* 2011/2012

[ALICE] *A Large Ion Collider Experiment*, `http://aliweb.cern.ch/`, 2012

[AmBoFü] U. Amaldi, W. de Boer, H. Fürstenau, *Comparison of grand unified theories with electroweak and strong coupling constants measured at LEP*, Physics Letters B, Volume 260, Issues 3-4, p. 447-455, 16 May 1991

[ATLAS] *Atlas Experiment*, `http://atlas.web.cern.ch/Atlas/Collaboration/`, 2012

[BaBaHa] R. Bainbridge, P. Barillon, G. Hall, *Production testing and quality assurance of CMS silicon microstrip tracker readout chips*, Nuclear Instruments and Methods in Physics Research Section A: Accelerators, Spectrometers, Detectors and Associated Equipment, Volume 543, Issues 2-3, 11 May 2005

[BaCaVi] E. Barberis, N. Cartiglia, C. LeVier, *Capacitances in silicon microstrip detectors*, Nuclear Instruments and Methods in Physics Research Section A, Volume 342, p. 90-95, 1994

[BaMuSa] G. Battistoni, S. Muraro, P.R. Sala, et. al., *The FLUKA code: Description and benchmarking*, Proceedings of the Hadronic Shower Simulation Workshop 2006, Fermilad 6-8, 2007

[Barth1] C. Barth on behalf of the CMS Collaboration, *Evolution of silicon sensors characteristics of the current CMS tracker*, Nucl. Instrum. Meth., Volume A658, p. 6-10, 2011

[Barth2] C. Barth on behalf of the CMS Collaboration, *Evolution of silicon sensor characteristics of the CMS silicon strip tracker*, Nucl. Instrum. and Meth., Volume A699, p. 178-183, 2013

[BarZen] C. Barth, S. Zenz, *CMS tracker bulk radiation effects update*, Second Inter-Experiment Workshop on Radiation Damage in Silicon Detectors, March 2012

[BeaBen] F. Beaudette, D. Benedetti, et. al., *Electron Reconstruction within the Particle Flow Algorithm*, CMS-AN-2009-034, 2009

[Bergau] T. Bergauer, *Process Quality Control of Silicon Strip Detectors for the CMS Tracker*, Dipl. TU Wien, 2004

[Berga2] T. Bergauer, *Quality Assurance of Silicon Strip Detectors and Monitoring of Manufacturing Process*, SiLC meeting, ILC workshop, 2005

[Braiba] S. Braibant, et. al., *Investigation of design parameters and choice of substrate resistivity and crystal orientation for the CMS Silicon Strip Tracker*, CMS Note 2003/020, CERN, CH-1211 Geneva 23, Switzerland, 2003

[Butz] E. Butz, *private communication*, 2012

[CAEN] CAEN *Technical Information Manual, Mod. A4601H/F*, NPO: 00105/03:A4601.MUTx/05, Revision n. 5, 30. March 2006

[CarHab] M. Carena, H.E. Haber, *Higgs Boson theory and phenomenology* Progress in Particle and Nuclear Physics, Volume 50, Issue 1, p. 63-152, 2003

[Cassa] G. Cassa, *Charge multiplication in highly irradiated planar silicon sensors* Proccedings of Sience, Vertex conference 2010

[CDF] S. Behari on behalf of CDF Collaboration, *Longevity Studies in the CDF II Silicon Detector*, IEEE Nuclear Sience Symposium Conference Record, 2009

[Chilin] A. Chilingarov, *Generation Current Temperature Scaling*, RD50 Technical Note RD50-2011-01, 2011

[CMS] *Compact Muon Solenoid experiment at CERN's LHC*, `http://cms.web.cern.ch/`, 2012

[CMSCOL] CMS Collaboration, *The CMS experiment at the CERN LHC*, JINST, Volume 3, 2008

[CMSHIG] CMS Collaboration, *Observation of a new boson at a mass of 125 GeV with the CMS experiment at the LHC*, Phys.Lett. B716 (2012) 30-61, 2012

[CMSLAY] CMS Collaboration, *Detector Drawings*, CMS-PHO-GEN-2012-002, 2012

[CMSPho] CMS Photos, *A TEC petal of the CMS tracker in a cold container*, CMS-PHO-OREACH-2006-014, 2006

[CNGS] *CERN Neutrinos to Gran Sasso*, `http://proj-cngs.web.cern.ch/proj-cngs/`, 2012

[COMPAS] COMPASS *COmmon Muon Proton Apparatus for Structure and Spectroscopy*, `http://wwwcompass.cern.ch/`, 2012

[Czochr] J. Czochralski, *Metalle*, Z. Phys. Chem., 92:219, 1918

[Demari] L. Demaria, *private communication*, 2012

[Dezill] B. Dezillie, *Radiation hardness studies of epitaxial silicon particle detectors for applications at the CERN Large Hadron Collider*, PhD. thesis, Univeristy Joseph Fourier - Grenoble 1, 1997

[Dierla] A. Dierlamm, *Untersuchung zur Strahlenhärte von Silizium-Sensoren*, Ph.D. thesis Universität Karlsruhe, IEKP-KA/03-23, 2003

[DijetA] ATLAS Collaboration *Observation of a Centrality-Dependent Dijet Asymmetry in Lead-Lead Collisions at* $\sqrt{s_{NN}} = 2.76\ TeV$ *with the ATLAS Detector at the LHC*, Phys. Rev. Lett., Volume 105, Nov. 2010

[DPG] The Detector Performance Group, *CMS Tracker Detector Performance Results, Approved results for ICHEP12*, `https://twiki.cern.ch/twiki/bin/view/CMSPublic/DPGResultsTRK#2010`, 2012

[DQM] CMS Tracker DQM, *Monitoring tools*, `http://vocms01.cern.ch/event_display/HDQM/Current/index.htm`, 2012

[EngBro] F. Englert, R. Brout, *Broken Symmetry and the Mass of Gauge Vector Mesons*, Phys. Rev. Lett., Volume 13, Issue 9, p. 321-323, 1964

[ETM] ETM *Professional Control*, http://www.pvss.com/, 2012

[EvaBry] L. Evans, P. Bryant, *LHC Machine*, Journal of Instrumentation, Volume 3, no 08, 2008

[Fermil] Fermilab, `http://www.fnal.gov/pub/today/archive/archive_2006/today06-08-10.html`, 2012

[Ferrar] A. Ferrari, et. al., *FLUKA: a multi-particle transport code*, CERN-2005-10, INFN/TC_05/11, SLAC-R-773, 2005

[FrBaPe] M. Friedl, T. Bauer, M. Pernicka, *Pion irradiation of the APV25 front-end chip*, CMS Conference Report, CMS CR 2001/015, November 2001

[FrJoMo] M.J. French, L.L. Jones, Q. Morrissey, et. al., *Design and results from the APV25, a deep sub-micron CMOS front-end chip for the CMS tracker*, Nuclear Instruments and Methods in Physics Research Section A: Accelerators, Spectrometers, Detectors and Associated Equipment, Volume 466, Issue 2, 1 July 2001

[GaGrSc] M. K. Gaillard, P. D. Grannis, F. J. Sciulli, *The Standard model of particle physics*, Rev.Mod.Phys., Volume 71, p. 96-111, 1999

[GoSaWe] J. Goldstone, A. Salam, S. Weinberg, *Broken Symmetries*, Phys. Rev. 127 p. 965-970, 1962

[GruShw] C. Grupen, B. Shwartz, *Particle Detectors* Cambridge University Press, The Edinburgh Building, Cambridge CB2 8RU, UK, 2008

[GuHaKi] G. S. Guralnik, C. R. Hagen, T. W. B. Kibble, *Global Conservation Laws and Massless Particles*, Phys. Rev. Lett., Volume 13, Issue 20, p. 585-587, 1964

[Guthof] M. Guthoff, *private communication*, 2011/2012

[Hall] R.N. Hall, *Electron-hole recombination in germanium*, Phys. Rev. **87**, 1952

[Hartma] F. Hartmann, *Evolution of Silicon Sensor Technology in Particle Physics*, STMP 231 Springer, Berlin Heidelberg 2009, DOI 10.1007/978-3-540-44774-0, 2009

[Hiscoc] P. Hiscocks, *A laplace transform cookbook*, Syscomp Electronic Design Limited, www.syscompdesign.com, March 2008

[Huhtin] M. Huhtinen, *Simulation of Non-Ionising Energy Loss and Defect Formation in Silicon*, ROSE/TN/2001-02, CERN, CH-1211 Geneva 23, Switzerland, 2001

[JaCaOt] C. Jacoboni, C. Canali, G. Ottaviani, et. al., *A review of some charge transport properties of silicon*, Solid-State Electronics, Volume 20, Issue 2, February 1977

[Junkes] A. Junkes, *Influence of radiation induced defect clusters on silicon particle detectors*, Ph.D. thesis, Universität Hamburg, DESY-THESIS-2011-031, July 2011

[KotSta] D. Kotlinski, A. Starodumov, *High level tracker triggers for CMS*, Nucl. Instrum. Meth., A501, 2001

[LaKaSa] T. Lampén, V. Karimäki, S. Saarinen, et. al., *Alignment of the Cosmic Rack with the Hits and Impact Points Algorithm*, CMS Note 2006/006, CERN, CH-1211 Geneva 23, Switzerland, 2006

[LeCaCi] M. Lenzi, E. Catacchini, C. Civinini, et. al., *Characterization of neutron irradiated Silicon Microstrip Detectors*, Nucl. Phys. B (Proc. Suppl.) 78, 1999

[Lee] S. Y. Lee, *Accelerator Physics*, World Scientific Publishing Co. Pte. Ltd., 2004

[Lefevr] C. Lefevre, *LHC: the guide (English version)*, CERN-Brochure-2009-003-Eng, 2009

[LHCb] *The LHCb collaboration*, http://lhcb.web.cern.ch/lhcb/, 2012

[LHCEXP] *Joint LHC Machine - Experiments Workshops*, http://ts-dep.web.cern.ch/ts-dep/groups/lea/int/workshops/, 2012

[LHCf] *The LHC forward experiment*, http://www.stelab.nagoya-u.ac.jp/LHCf/LHCf/index.html, 2012

[LHCSCH] LHC, *2012 LHC Schedule*, https://espace.cern.ch/be-dep/BEDepartmentalDocuments/BE/LHC_Schedule_2012.pdf, 2012

[LHCSWG] (LHC Higgs Cross Section Working Group *Handbook of LHC Higgs Cross Sections: 1. Inclusive Observables* arXiv:1101.0593v3, 2011

[Lindha] J. Lindhard, V. Nielson, *Nuclear collisions and ionisation fluctuations in charged particle detectors*, Phys. Lett. 2(5), p. 209-211, 1962

[LiWaLe] G. Lindström, S. Watts, F. Lemeilleur, *3rd RD48 status report: the ROSE collaboration (R & D on silicon for future experiments)*, CERN, Geneva, CERN-LHCC-2000-009, 1999

[Lumino] CMS Collaboration, *CMS Luminosity - Public Results*, https://twiki.cern.ch/twiki/bin/view/CMSPublic/LumiPublicResults, 2012

[Lutz] G. Lutz, *Semiconductor Radiation Detectors* Springer, Berlin, Heidelberg, New York, London, Paris, Tokyo, 1999

[MaLiFi] L. Masetti, V. Lindenstruth, P. Fischer, *Implementation of a Large Scale Control System for a High-Energy Physics Detector: The CMS Silicon Strip Tracker*, Inst. Appl. Math., Heidelberg, 2011

[MaMaMo] G. Magazzú, A. Marchioro, P. Moreira, *The Dector Control Unit: An ASIC for the Monitoring of the CMS Silicon Tracker*, IEEE Trans. on Nucl. Science, Volume 51, no 4, August 2004

[MeaLum] CMS Collaboration, *Measurement of CMS Luminosity*, CMS Physics Analysis Summary, CMS PAS EWK-10-004, 2010

[MoEDAL] *The Monopole & Exotics Detector at the LHC*, `http://moedal.web.cern.ch/`, 2012

[MoFeFr] M. Moll, H. Feick, E. Fretwurst, et. al., *Comparison of defects produced by fast neutrons and ^{60}Co-gammas in high resistivity silicon detectors using Deep Level Transient Spectroscopy*, International Conference on Radiation Effects on Semiconductor Materials, Detectors and Devices, Firenze, Italy , 6.- 8. March 1996

[Moll] M. Moll, *Radiation Damage in Silicon Particle Detectors*, Universität Hamburg, DESY-THESIS-1999-040, 1999

[MollRS] M. Moll, *Summary of the 3rd ROSE STATUS REPORT*, ROSE Meeting on Radiation Hardening of Silicon Detectors, CERN, 16-17 March 2000, 5th ROSE Workshop, RD48, 2000

[Moran] D. Moran on behalf of LHCb VELO *Effective depletion voltage & 2nd metal layer effects in the LHCb VELO*, 20th RD50 Workshop on Radiation hard semiconductor devices for very high luminosity colliders, Bari 2012

[Müller] S. Müller, *The Beam Condition Monitor 2 and the Radiation Environment of the CMS Detector at the LHC*, CERN-THESIS-2011-085

[Murray] W. J. Murray, *LHC potential: Energy and Luminosity*, Proccedings of Chamonix 2011 workshop on LHC performance, 2011

[NA61] *NA61/SHINE*, `https://na61.web.cern.ch/na61/xc/index.html`, 2012

[Obs125] CMS Collaboration *Observation of a new boson at a mass of 125 GeV with the CMS experiment at the LHC*, CMS-HIG-12-028; CERN-PH-EP-2012-220, arXiv:1207.7235v1, 2012

[PDG] The Particle Data Group, `http://pdg.lbl.gov`, 2012

[PerMuo] CMS Collaboration, *Performance of CMS muon reconstruction in pp collision events at $\sqrt{s}$ = 7 TeV*, CMS-MUO-10-004; CERN-PH-EP-2012-173, arXiv:1206.4071v1, 2012

[PesSch] M. E. Peskin, D. V. Schroeder, *Introduction to quantum field theory* Westview Press, 1995

[PFlow] CMS Particle Flow Physics Object Group, *Particle Flow Reconstruction of Jets, Taus, and MET*, CMS-AN-2009-039, 2009

[PHiggs] P. W. Higgs, *Broken Symmetries and the Masses of Gauge Bosons*, Phys. Rev. Lett., Volume 13, Issue 16, p. 508-509, 1964

[PIXTDR] Pixel collaboration, *CMS technical design report for the pixel detector upgrade*, CMS UG-TDR-1, 26. September 2012

[Pointo] A. J. Pointon, *Piezoelectric Devices* IEE Proc., 129, Pt. A, 285, 1982

[Potenz] A. Potenza, *private communication*, 2012

[PPCros] TOTEM Collaboration, *First measurement of the total proton-proton cross section at the LHC energy of* $\sqrt{s} = 7$ *TeV*, EPL 96 21002, 2011

[Quench] CMS Collaboration *Observation and studies of jet quenching in PbPb collisions at* $\sqrt{s_{NN}} = 2.76TeV$, CMS-PAS-HIN-10-004, Feb. 2011

[Quert] L. Quertenmont, *Particle Identification with Ionization energy loss in the CMS Silicon Strip Tracker*, CMS Conference Report (IPRD10), CMS CR 2010/120, 2010

[RaCeFr] M. Raymond, G. Cervelli, M. French, et. al., *The CMS Tracker APV 25 0.25* μm *CMOS Readout Chip*, Proc. of the 6$^{\text{th}}$ Workshop on Electronics for LHC and Future Experiments, Cracow, Poland, 11-15 Sep. 2000

[Raymon] M. Raymond, *Private communication*, 2011/2012

[RD50] G. Casse, *Overview of the recent activities of the RD50 collaboration on radiation hardening of semiconductor detectors for the sLHC*, Nuclear Instruments and Methods in Physics Research Section A: Accelerators, Spectrometers, Detectors and Associated Equipment, Volume 598, Issue 1, January 2009

[RoEnRa] S. Roesler, R. Engel, J. Ranft, *The Monte Carlo Event Generator*, DPMJET-III SLAC-PUB-9740, 2000

[ROOT] F. Rademakers, P. Canal, et. al., *ROOT Development Team*, `http://root.cern.ch/drupal/content/root-development-team`, 2012

[Rossi] L. Rossi, *Superconductivity: its role, its success and its setbacks in the Large Hadron Collider of CERN*, Superconductor Science and Technology, Volume 23, no 3, 2010

[Rubbia] C. Rubbia, *Experimental observation of the intermediate vector bosons W+, W- and Z0*, Rev. Mod. Phys., Volume 57, no CERN-OPEN-94-004, p. 699-722, 1994

[ShoRea] W. Shockley, W.T.J. Read, *Statistics of the recombinations of holes and electrons*, Phys. Rev. **87** (5), 1952

[Sze] S. Sze, *Physics of semiconductor devices*, Wiley, 2 edition, November 1981

[TDR] V. Karimäki, et. al., *The CMS tracker system project: Technical Design Report*, CERN, Geneva, 1997

[TOTEM] *Total Cross Section, Elastic Scattering and Diffraction Dissociation at the LHC*, `http://totem.web.cern.ch/Totem/`, 2012

[TraPer] CMS Collaboration, *CMS Tracking Performance Results from Early LHC Operation*, arXiv:1007.1988; CERN-PH-EP-2010-019; CMS-TRK-10-001., Geneva, CERN, 2010

[UpdLum] CMS Collaboration, *Absolute Calibration of the Luminosity Measurement at CMS: Winter 2012 Update*, CMS PAS SMP-12-008, 2012

[WIKI] Wikipedia *The free encyclopedia*, `http://www.wikipedia.org/`, 2012

[WWW] *WorldWideWeb: Proposal for a HyperText Project*, `http://www.w3.org/Proposal.html`, 2012

[Zichin] A. Zichini, *Innovative Detectors for Supercolliders*, Proceedings of the 42nd Workshop of the INFN ELOISATRON Project, World Scientific Publishing Co. Pte. Ltd., 2004

[Zimmer] F. Zimmermann, *Machine Progress Towards Higher Luminosity*, CMS Upgrade Meeting, FNAL, Chicago, 7 November 2011